

The Formation of Iron Ore at the Keystone Skarn, Puerto Rico

by

Jessica N. Patrick

A thesis submitted to the Graduate Faculty of
Auburn University
in partial fulfillment of the
requirements for the Degree of Master of Science

Auburn, Alabama
August 5th, 2023

Approved by

Laura Bilenker, Chair, Assistant Professor of Geosciences, Auburn University
Thomas Hudgins, Associate Professor of Geology, University of Puerto Rico, Mayagüez
Willis Hames, Professor of Geosciences, Auburn University

Abstract

Iron (Fe) is essential to modern life, primarily for its use in steel. Understanding the processes that transport and deposit Fe within the crust is crucial to finding and evaluating Fe deposits for economic potential. The complex tectonic and magmatic history of Puerto Rico as an extinct and unaccreted island arc was conducive to the formation of many ore deposits, but they are understudied. In this investigation, field observations, petrography, and geochemical analysis of Fe ore from the Keystone skarn provide records of fluid movement and metal transport in an unaccreted Fe skarn. Keystone is hosted in volcanoclastic rocks and dominantly made up of magnetite in the form of two subparallel ridges. The ore bodies potentially extend to another hilltop ~0.52km away. A zone of alteration runs perpendicular to the ridges. The trace element (Ti, Al, V, Ca, Mn) concentrations in the magnetite are consistent with global skarns and indicate a hydrothermal origin rather than crystallization from magma. The $\delta^{56}\text{Fe}$ (-0.12‰ to 0.21‰) and $\delta^{18}\text{O}$ (0.10‰ to 2.00‰) values of Keystone magnetite are consistent with global accreted and unaccreted Fe skarns. The Fe and O isotopic signatures indicate multiple fluid sources but point to initial magmatic-hydrothermal fluids and small proportions of meteoric influx in later stages. Oscillatory zonation within the magnetite indicates changing formation conditions related to additional fluid input, evolving source pluton, or reactions between the fluid and host rock. Truncations of the oscillatory zoning indicate episodic dissolution and reprecipitation processes. Mineralogical and textural evidence imply that both redox dependent and independent reactions altered the magnetite to martite. Overall, a genetic model of the Keystone skarn is proposed as three main stages: 1) intrusion of an Fe-rich pluton, 2) magmatic-hydrothermal fluid release and metal deposition, 3) introduction of late Si-Al-Ca-rich fluids and meteoric water. This new characterization of Keystone and detailed analysis of its ore will

inform the people of Puerto Rico in mineral resource assessment and exploration. This contribution is also applicable to global exploration for Fe skarns during a key time for securing Fe as a commodity.

Acknowledgments

First, I cannot begin to express my thanks to Dr. Laura Bilenker, my advisor, who academically challenged me and supported my endeavors throughout the last two years. I am extremely grateful to Dr. Thomas Hudgins for his help with fieldwork and mentorship. I would also like to extend my sincere thanks to Dr. Dominique Weis for granting us access to the PCIGR facilities and Kathy Gordon and Dave Daquioag for support with sample preparation and Fe isotope analysis at the University of British Columbia. As well as Dr. Zeki Billor for assistance with LA-ICP-MS and XRD and Dr. Willis Hames for assistance with EMPA at Auburn University. Many thanks to Dr. Ilya Bindeman at the University of Oregon for collecting oxygen isotope data for me. A special thank you to C. Lauren Talkington, and all my friends at Side Track Coffee for encouragement and support. I would like to acknowledge the National Science Foundation, grant EAR-2217927, the GAB research and travel grant, the Fousek research grants, and GSA travel grant for helping make this research possible.

Table of Contents

Abstract	ii
Acknowledgments	iv
Table of Contents	v
List of Tables	vii
List of Figures	viii
1. Introduction	1
2. Objectives	2
3. Background	2
3.1 The Geologic Setting of Puerto Rico	2
3.2 Skarn Deposits	4
3.3 The Keystone Fe Skarn Deposit	7
4. New Field Observations of the Keystone Skarn	8
5. Methods	12
5.1 Sample Collection	12
5.3 Major and Trace Element Geochemistry	15
5.3.1 Laser Ablation-Inductively Coupled Plasma-Mass Spectrometry.....	15
5.3.2 Electron Microprobe Analysis	17
5.4 Isotope Geochemistry	19
5.4.1 Stable Fe Isotope Analysis.....	19
5.4.2 Stable O Isotope Analysis	21
6. Results	21
6.1 Petrography of the Keystone Fe Ore	21
6.2 Geochemical Zonation of the Keystone Magnetite	24
6.3 Observations of Non-Ore Minerals	29
6.4 Iron Content and Trace Element Composition of Keystone Magnetite Ore	31
6.5 Stable Fe and O Isotope Composition of Magnetite ore from the Keystone Skarn	32
7. Discussion	34
7.1 Updated Observations of the Keystone Fe Skarn Deposit and Characterization of the Magnetite Ore	34
7.2 Modification and Replacement of Keystone Magnetite	35
7.2.1 Trace Element and Textural Evidence for Modification of the Keystone Magnetite ...	35

7.2.2 Oxidation and Redox-Independent Replacement of Keystone Magnetite	36
7.3 The Source of Keystone Magnetite	37
7.3.1 Trace Element Evidence for the Source of Keystone Magnetite	37
7.3.2 Stable Fe and O Evidence for the Source of Keystone Magnetite	40
7.4 Keystone Stable Isotope Geochemistry Compared to Global Fe Skarn Data	44
7.5 Keystone Skarn Geology and Geochemistry Compared to Puerto Rican Fe Skarns: Tibes and Island Queen	46
7.6 The Formation Model of the Keystone Fe Skarn	48
7.6.1 Stage 1: Intrusion of Fe-rich Pluton.....	48
7.6.2 Stage 2: Magmatic-Hydrothermal Fluid Release and Metal Deposition.....	48
7.6.3 Stage 3: Late Si-Al-Ca-Rich Fluids and Meteoric Water Input	50
8. Future Work.....	53
9. Conclusions.....	55
References.....	57
Appendix A: Supplemental Figures	62
Appendix B: Full Fe and Trace Element Dataset by Electron Microprobe Analysis	64
Appendix C: Full Trace Element Dataset by Laser Ablation-Inductively Coupled Plasma-Mass Spectrometry	71

List of Tables

Table 1: Characteristics and locations of all samples collected or analyzed in this study.....	13
Table 2: LA-ICP-MS conditions used for analysis	17
Table 3: EMPA setup.....	18
Table 4: Estimated extent of oxidation of each magnetite powder sample	19
Table 5: Summary of petrographic observations	22
Table 6: Iron, Si, and Al concentrations in Keystone magnetite measured by EMPA	29
Table 7: Iron concentrations (wt%) for Keystone magnetite determined by EMPA.....	31
Table 8: Trace element concentrations (wt%) determined by LA-ICP-MS	32
Table 9: The Fe isotope composition of Keystone magnetite samples	33
Table 10: The O isotope composition of Keystone magnetite samples	33

List of Figures

Figure 1: Map of the tectonic region surrounding Puerto Rico	3
Figure 2: Generalized geologic map of Puerto Rico illustrating the location of three Fe skarn deposits	4
Figure 3: Simplified genetic model of skarn deposits during three stages of formation	5
Figure 4: Sketch of the sequence of reaction fronts expected to form during stages 1 and 2 of skarn formation	6
Figure 5: The mineralogy and primary commodity of a skarn deposit	7
Figure 6: Locations and spatial distribution of all 25 collected samples and their associated mineralogy	10
Figure 7: Field photos of the ore ridges on Cell Tower Hill.....	10
Figure 8: Field photo of a quartz pocket in sample KS-17	11
Figure 9: Field photos of variable clay mineralogy between north and south ridge	11
Figure 10: Field photo of previously unmapped local igneous intrusion	12
Figure 11: Photos of the portable core drill in use and core product.....	14
Figure 12: Reflected light observations of magnetite and Fe oxides.....	23
Figure 13: Additional reflected light observations of magnetite and Fe oxides	24
Figure 14: BSE images and WDS maps of Fe and Si.....	25
Figure 15: RL, BSE images and WDS maps of oscillatory zoning along the edge of a euhedral magnetite grain from KS-19	26
Figure 16: Reflected light and false color images of ore magnetite from KS-26.....	27
Figure 17: BSE images and WDS maps of Fe, Si, and Al in zoned massive magnetite	28
Figure 18: Transmitted light observations of non-ore minerals	30
Figure 19: Plot of Ti+V (wt%) vs. Ca+Al+Mn (wt%) measured in Keystone magnetite	38
Figure 20: Plot of V (ppm) vs. Ti (ppm) in the Keystone magnetite.....	40
Figure 21: Plot of Fe/(Mg+Al+Mn) (ppm) vs. Ti (ppm) in the Keystone magnetite	40
Figure 22: Discrimination diagram of $\delta^{56}\text{Fe}$ vs. $\delta^{18}\text{O}$ to determine the fluid source(s) of Keystone magnetite.....	41
Figure 23: Spatial relationships of samples and Fe and O isotope results.....	43
Figure 24: $\delta^{56}\text{Fe}$ values of Keystone magnetite compared to global Fe-associated skarns	45

Figure 25: $\delta^{18}\text{O}$ values of Keystone magnetite compared to six global Fe-associated skarns... 45

Figure 26: Schematic illustration of magmatic-hydrothermal fluid flow from the Fe-rich pluton interacting with the volcanoclastic host rocks to form the magnetite ore bodies within the Keystone skarn..... 49

Figure 27: Sketch illustrating the textures that result from modification of Keystone magnetite due to redox-dependent and redox-independent (DRP) processes 50

Figure 28: Spatial relationships of samples and trace element results..... 52

1. Introduction

The volcanic island arc terrane of Puerto Rico, located at the easternmost end of the Greater Antilles, hosts a variety of ore deposits as a result of its geologic history. Fortuitously, during the Late Cretaceous and Early Paleogene, Puerto Rico was intruded by numerous plutons, which facilitated the concentration of many metals including iron (Fe) (Bawiec, 1998). Iron ore deposits have been reported in Puerto Rico since at least the early 1900s (e.g., Berkey, 1915; Fettke, 1924) and at least three Fe deposits have been identified: Keystone, Island Queen, and Tibes, with Keystone being the largest one known on the island (Bawiec, 1998 and references therein).

Iron ore is predominantly used in steel and is a resource heavily utilized in modern life. On average, an American who was born in 2022 will require 18,317 pounds of Fe ore during their lifetime (Minerals Education Coalition, 2022). Iron ore is mined in about 50 countries and its worldwide consumption rate is expected to increase, due in part to the anticipated shift toward renewable energy resources (U.S. Geological Survey, 2022a; Wang et al., 2023). Therefore, mapping and characterizing Fe deposits are critical to securing ample Fe ore to sustain societal growth and development.

Despite being rich in mineral deposits and accessible historical documentation of them, Puerto Rico's resources are vastly understudied due to a series of laws that permits only minimal mining to occur (Gelabert, 2011). Before the current mining ban, Keystone and Island Queen were mined briefly from 1951-1953 by the West Indies Mining Company, producing 220,475 tons of ore with a monetary value of \$1,270,000 (Vázquez, 1960). Tibes, located in southcentral Puerto Rico, was never mined substantially due to its small size. The classification of Fe deposit assigned to these sites, Fe skarn, is generally formed in island arcs and most of the examples

studied to date have undergone some metamorphism or alteration associated with continental accretion. Since Puerto Rico is an unaccreted island arc, its Fe deposits present a rare opportunity to apply geochemical methods to minimally altered Fe skarns to understand their formation, the transport of Fe in the crust, and to help secure Fe ore needed in everyday life.

2. Objectives

The focus of this study was to produce a detailed characterization of the Keystone Fe ore and determine the genesis of the deposit by establishing relationships between magmatic activity, fluid flow events, and metal transport. This project continued recent investigations into the Fe ore deposits of Puerto Rico, and comparisons of the three Fe skarns can help determine the role of island-scale features and processes in the formation of the deposits. Overall, this research addresses two main scientific questions: (1) What is the composition and source of the Fe ore at Keystone? (2) How did the Keystone deposit form?

3. Background

3.1 The Geologic Setting of Puerto Rico

Located along the easternmost side of the Greater Antilles, Puerto Rico is part of the Puerto Rico-Virgin Islands microplate within the Caribbean plate (Figure 1) (Jolly et al., 1998; Schellekens, 1998). The Caribbean plate has a complex tectonic history that is yet to be fully understood and is readily debated (e.g., Lidiak and Larue, 1998; Schellekens, 1998). Simply, the Farallon plate (proto-Caribbean) started to subduct under the North and South American plates during the breakup of Pangea. By about 80 Ma, an abnormally thick oceanic plateau formed on the Farallon plate due to subduction volcanism (Schellekens, 1998; Boschman et al., 2014). The oceanic plateau was too buoyant to subduct under the North and South American plates, and this

caused a subduction reversal. The renewed subduction to the east formed the island arc chain known today as the Antilles. Over time, left lateral transcurrent faulting moved the island arc away from the subduction zone, so that the once westward-facing arc now faced eastward (Lidiak and Larue, 1998; Schellekens, 1998). The exact timing of the subduction reversal, initiation of renewed subduction, and the amount of lateral movement and rotation have been topics of hot debate (Schellekens, 1998 and references therein).

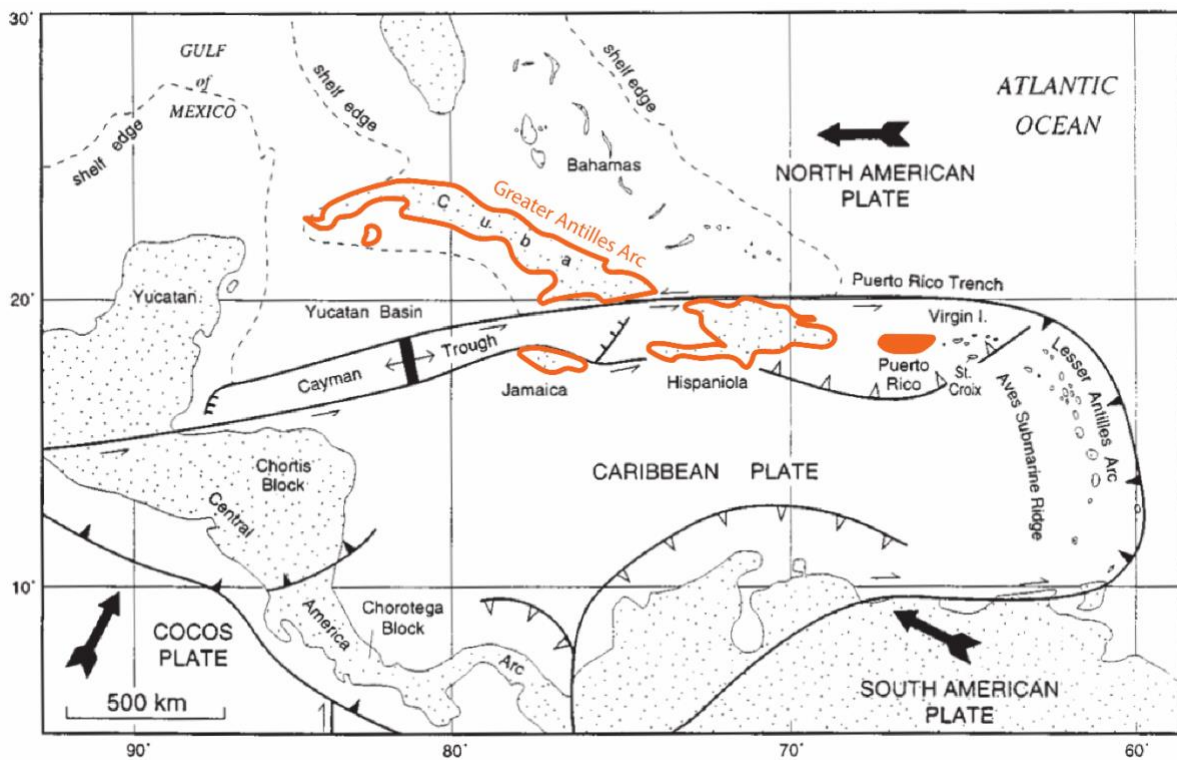


Figure 1: Map of the tectonic region surrounding Puerto Rico, which is filled in with orange and is located at the eastern most part of the Greater Antilles, which is outlined in orange (modified from Lidiak and Larue, 1998). The Greater Antilles includes Cuba, Jamaica, Hispaniola, Puerto Rico, and the Cayman Islands.

The island of Puerto Rico is an extinct island arc divided into three sections or provinces based on fault zones and basement lithology (Figure 2; Bawiec, 1998; Jolly et al., 1998; Schellekens, 1998 and references therein). The provinces are named the Southwestern Igneous Province (SIP), Central Igneous Province (CIP), and Northeastern Igneous Province (NIP). The SIP and CIP are divided by the Southern Puerto Rico Fault Zone (SPRFZ) and the CIP and NIP

are divided by left-lateral faulting along the San Francisco-Cerro Mula Fault Zone, which is part of the Northern Puerto Rico Fault Zone (NPRFZ; Figure 2; Jolly et al., 1998; Schellekens, 1998). By about 85 Ma, the CIP and NIP collided, creating the NPRFZ. Next, starting around 69 Ma, felsic magmatic bodies such as the San Lorenzo Batholith intruded into basement sedimentary and volcanic rocks within the CIP (Figure 2; Jolly et al., 1998; Schellekens, 1998). The intrusions are concurrent with the renewed subduction from the east (Schellekens, 1998).

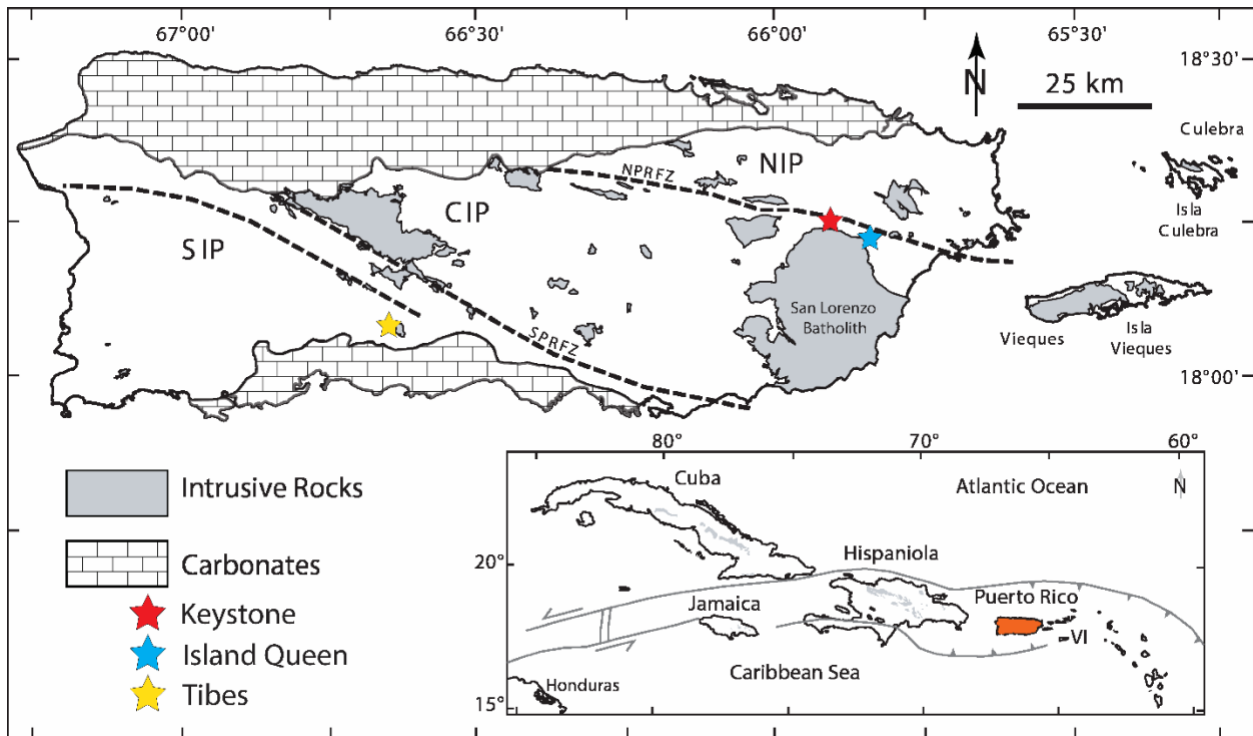


Figure 2: Generalized geologic map of Puerto Rico illustrating the location of three known Fe skarn deposits: Keystone, Island Queen, and Tibes (modified from map provided by Dr. Thomas Hudgins). SIP = Southwestern Igneous Province, SPRFZ = Southern Puerto Rico Fault Zone, CIP = Central Igneous Province, NPRFZ = Northern Puerto Rico Fault Zone and NIP = Northeastern Igneous Province. Inset highlights the generalized modern tectonic setting of Puerto Rico, highlighted in orange within the Greater Antilles. VI = Virgin Islands.

3.2 Skarn Deposits

The numerous faults and magmatic intrusions associated with the formation of Puerto Rico are why it is home to numerous ore deposits, such as the Keystone, Island Queen, and Tibes Fe skarns. Skarn deposits are mined worldwide for metals such as Fe, Mo, W, Au, Cu, Pb, Zn,

and Sn (e.g., Einaudi et al., 1981; Meinert et al., 1992; Meinert et al., 2005; Robb, 2005).

Typically, skarns form near a magmatic intrusion in surrounding carbonates or calcareous volcanic rocks as a product of metamorphism and metasomatism (Figure 3; Einaudi et al., 1981; Meinert et al., 2005; Robb, 2005). A skarn is defined by its mineralogy; therefore, it can form in numerous tectonic settings and host rocks but predictably has calc-silicate minerals including garnet, pyroxene, epidote, and wollastonite (Meinert et al., 2005 and references therein).

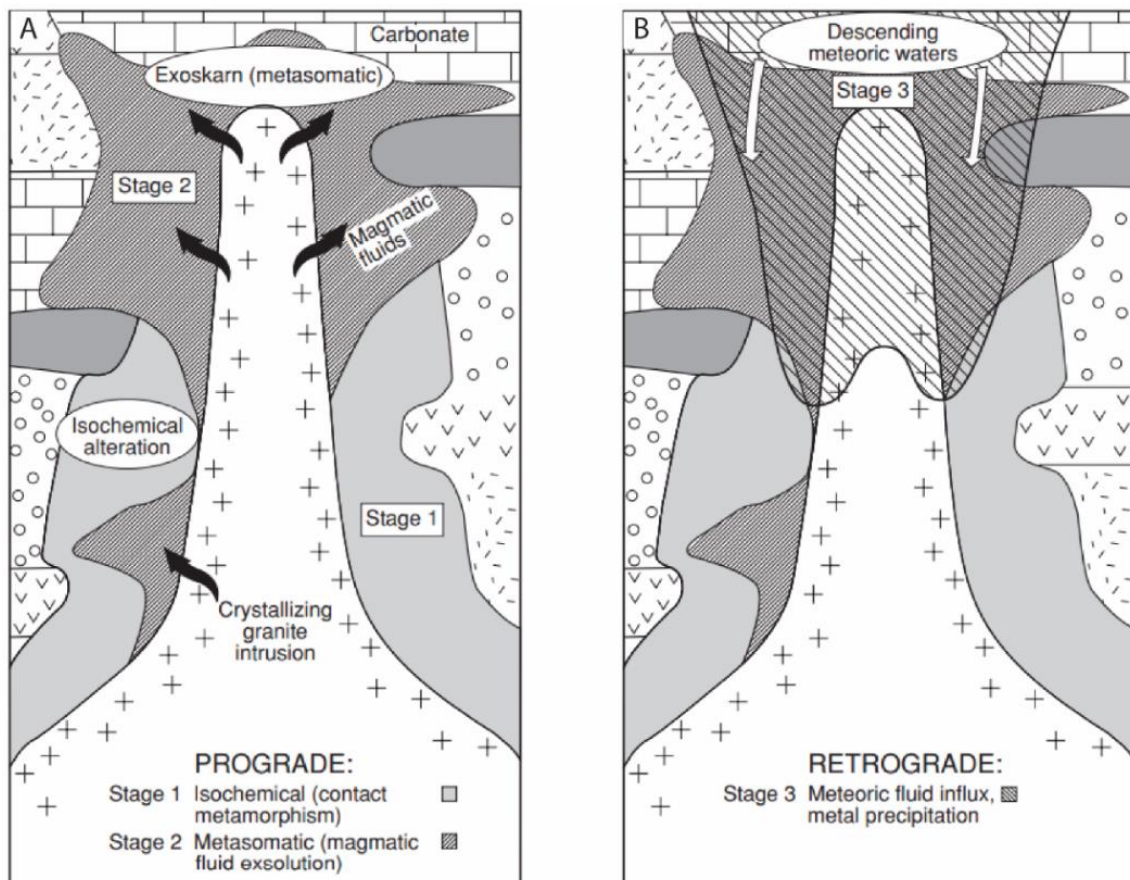


Figure 3: Simplified genetic model of skarn deposits during three stages of formation. (A) prograde stages 1 and 2, (B) retrograde stage 3 (Robb, 2005).

There are three main stages of skarn formation (Figure 3). First, a magmatic intrusion introduces heat, producing increasingly hot (prograde) conditions and causing isochemical contact metamorphism of the wall rock (Figure 3A). Then, metasomatism of the host rock occurs by the episodic introduction of fluids from the pluton, creating a sequence of reaction fronts and

forming new anhydrous minerals (Figure 4). Initial metal deposition can occur during stage 2 (Figure 3A). Finally, in stage 3, the cooling of the intrusion allows for the introduction of meteoric water (Figure 3B). The retrograde reactions between these fluids and the already metasomatized host rocks cause the formation of hydrous minerals and precipitation of metals (Einaudi et al., 1981; Meinert et al., 2005; Robb, 2005). The oxidation state of the pluton and host rock are important controls on the resulting mineralogy and primary commodity of the skarn deposit (Figure 5; Einaudi et al. 1981; Meinert et al. 2005).

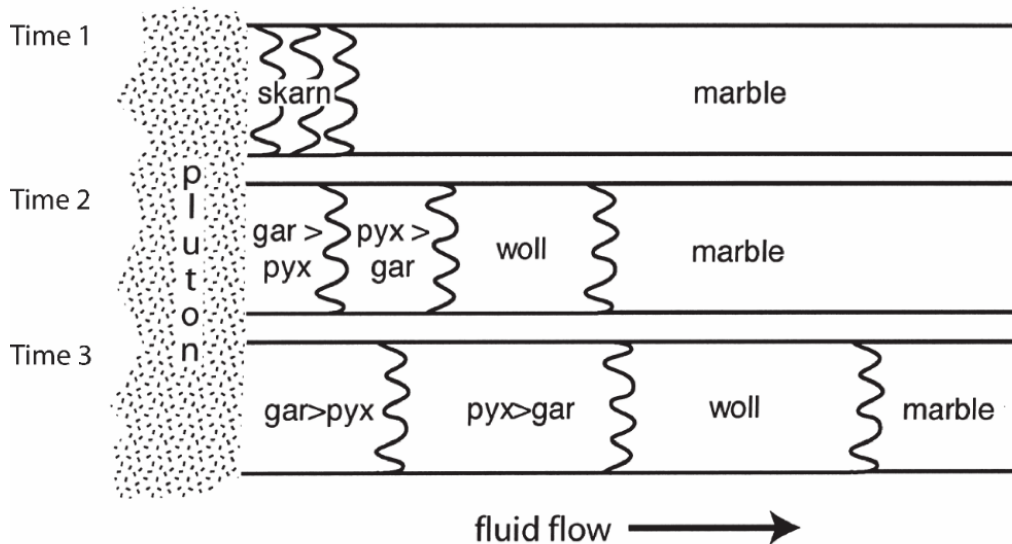


Figure 4: Sketch of the sequence of reaction fronts expected to form during stages 1 and 2 of skarn formation. The time series represents three independent slices of time (Time 1, Time 2, Time 3). The different reaction fronts (squiggled vertical lines) progress away from the pluton with multiple episodes of magmatic fluid released into the metamorphosed host rock (marble formed during stage 1) (Meinert et al., 2005).

Mined for their Fe oxide content as magnetite or hematite, Fe skarns are subdivided into two categories, calcic Fe and magnesian Fe skarns. Calcic Fe skarns are associated with intrusions of Fe-rich plutons into volcanic or limestone host rock in oceanic island arcs. Mineralogically, they are rich in garnet and pyroxene and have minor ilvaite, actinolite, and epidote (Meinert et al., 2005). On the other hand, magnesian Fe skarns are hosted in Mg-rich wall rock and form in a variety of tectonic settings. Mineralogically, they are rich in forsterite,

diopside, talc, periclase, and serpentine (Meinert et al., 2005). The Fe skarns of Puerto Rico are expected to be the calcic type.

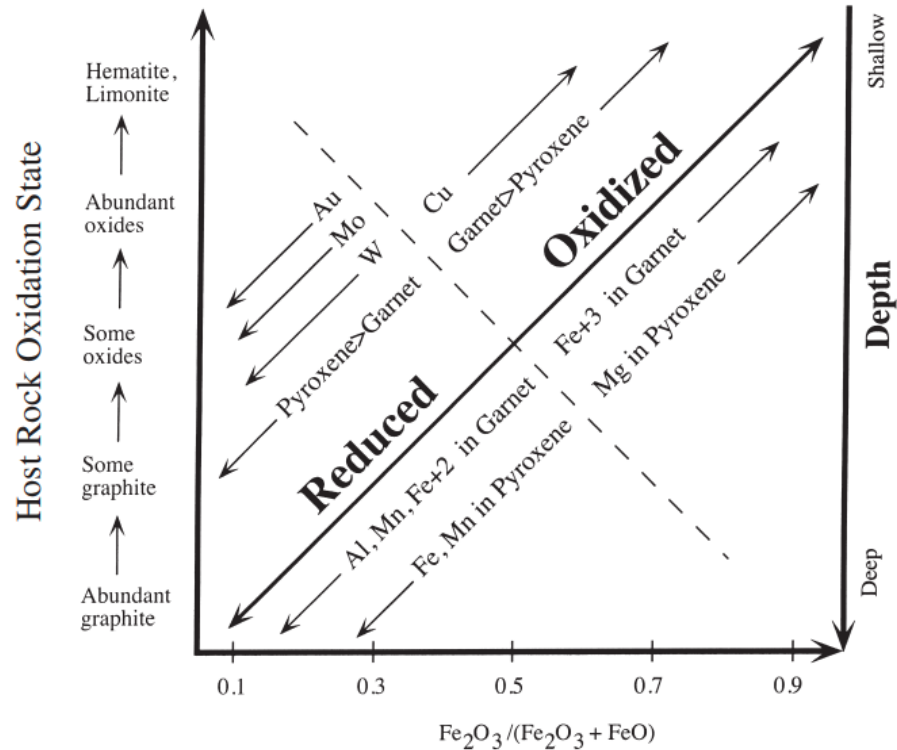


Figure 5: The mineralogy and primary commodity of a skarn deposit are related to the depth of formation and how reducing or oxidizing the host rocks and source pluton were (Meinert et al., 2005).

3.3 The Keystone Fe Skarn Deposit

Located along the southeastern side of the CIP near the NPRFZ, the Keystone Fe skarn was reported as early as 1915 (Berkey, 1915; Fettke, 1924) to contain high-grade magnetite ore (Figure 2; Vázquez, 1960 and references therein). The Fe deposits on the eastern side of Puerto Rico near Humacao (Keystone, Island Queen) were described historically as predominantly composed of magnetite and hematite (Colony and Meyerhoff, 1935 and references therein). Fettke (1924) even described a cluster of five magnetite deposits with four of them grouped into a “Main Belt” about 2.4km from Juncos and a fifth deposit located about 1.6km northeast of the Main Belt. This fifth deposit (and possibly the fourth) is likely Island Queen, and the largest

deposit (“No. 1”) was dubbed the Juncos Deposit, which is likely Keystone. The Juncos Deposit was estimated to be ~0.6km long, with outcrops of ore magnetite, martite, and hematite that vary in width (Fettke, 1924). Throughout the historic literature, Keystone was mentioned under several additional names including La Mina, La Esperanza, and Juncos Mine (Bawiec, 1998; Vázquez, 1960 and references therein).

Keystone outcrops near the northern edge of the San Lorenzo Batholith, which intruded into a thin tuffaceous limestone (Figure 2). The documented ore bodies form two main lenses around 6-15m wide (Vázquez, 1960; Bawiec, 1998). The lower lens is garnetiferous, therefore the upper lens was most likely the main source of ore mined by the West Indies Mining Company (Vázquez, 1960). Mineralogically, the ore has been reported to consist primarily of magnetite intergrown with martite, specular hematite, andradite garnet, and epidote with lesser amounts of quartz, malachite, azurite, calcite chrysocolla, chalcopyrite, and other minerals (Vázquez, 1960; Bawiec, 1998). The garnet at Keystone was described to be birefringent as early as Fettke (1924). The exact age of the deposit is unknown but is believed to be a part of the “older complex”, which formed during the Cretaceous and early Tertiary (Vázquez, 1960 and references therein).

4. New Field Observations of the Keystone Skarn

Researchers from Auburn University (AU) and the University of Puerto Rico, Mayagüez (UPRM) visited the Keystone skarn in July 2022. Keystone is located about 2.6km east of the town of Juncos in eastern Puerto Rico and is reachable near a hilltop cell tower (“Cell Tower Hill”, Figure 6) and nearby public land (“East Hill”, Figure 6). The magnetite ore bodies form two subparallel ridges atop a broader topographical ridge with a strike of S57°E. This measurement is consistent with the previously published estimate of S53°E (Fettke, 1924). The

northern ridge is ~4.6m wide (Figure 7A) and the southern ridge ranges from 7.6-15m wide (Figure 7B). Due to past mining activity and modern vegetation in the area, it is difficult to discern which ridge was considered by Vázquez (1960) to be the upper lens or the lower lens. However, based on field observations, the southern ridge appears to have been mined more extensively or instead of the northern ridge. The ore on both ridges is highly weathered and the grade of the northern ridge varies across the lateral extent. The eastern side of the northern ridge is laminated with pockets of quartz (Figure 8), hematite, and copper oxides. The western extent of the northern ridge is dominated by thin veins of hematite and garnet cross-cutting weathered iron oxide at about 40° and 140°. The southern ridge has a higher grade and is dominated by massive magnetite. Due to heavy vegetation in the area, only ~0.11km in length of the north and south ridges were exposed enough to be mapped and examined (Figure 6).

Ore was also discovered ~0.52km following strike from the eastern extent of the northern ridge; thus, it is possible that the ore bodies extend to around ~0.63km in length (Figure 6). In between the two ridges are zones of alteration differentiated by their variable clay mineralogy (Figure 9). Pink alteration is ~7.6m wide, yellow/green alteration is ~3m wide and red oxidation/volcaniclastics are ~3m wide. The host rock is a mafic, volcaniclastic that is weakly magnetitic. Unmapped igneous intrusions were discovered within the host rock on the East Hill (Figures 6, 10).

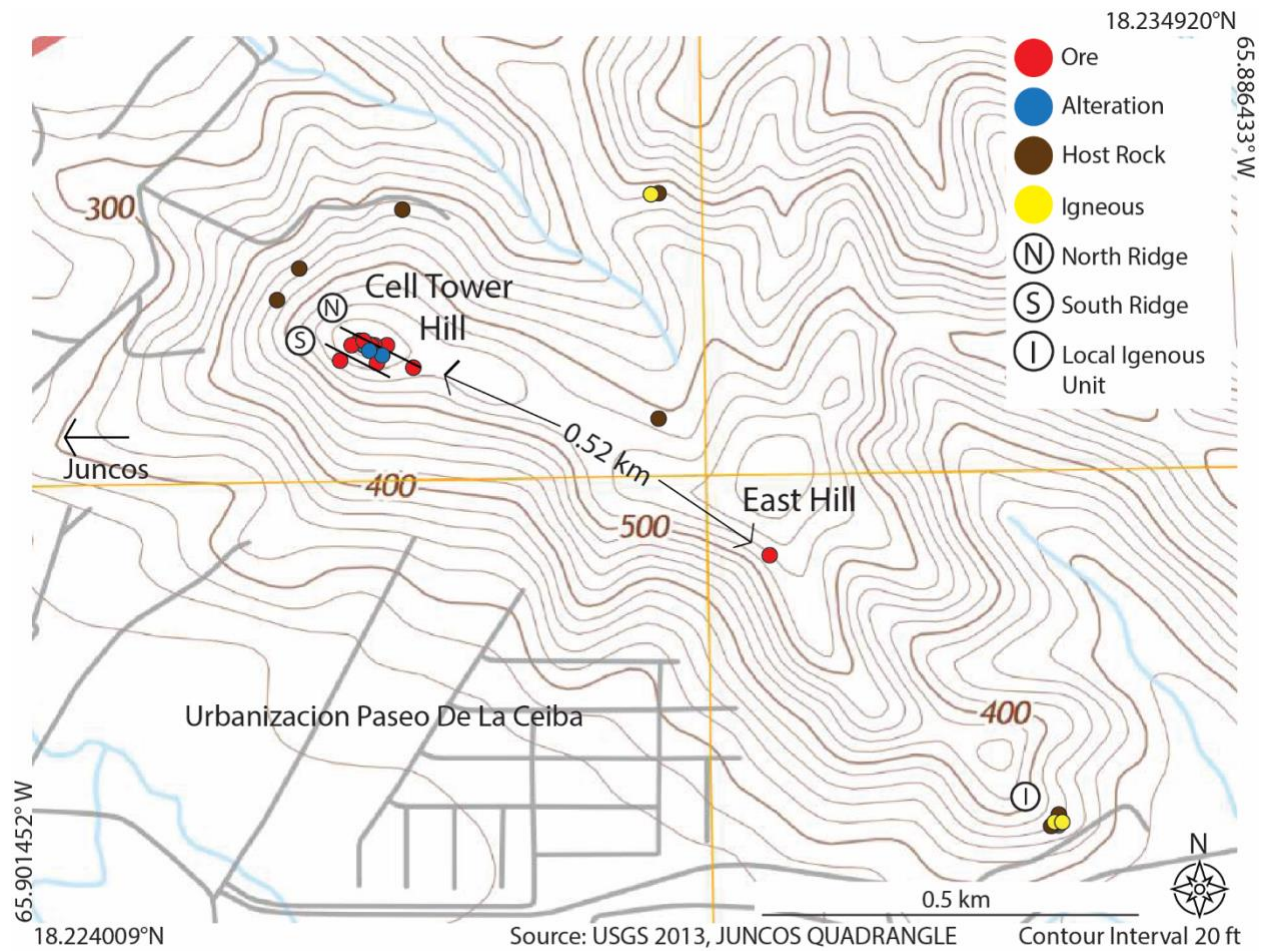


Figure 6: Locations and spatial distribution of all 25 collected samples and their associated mineralogy (ore, alteration, host rock, and igneous) (U.S. Geological Survey 2013, Juncos Quadrangle).

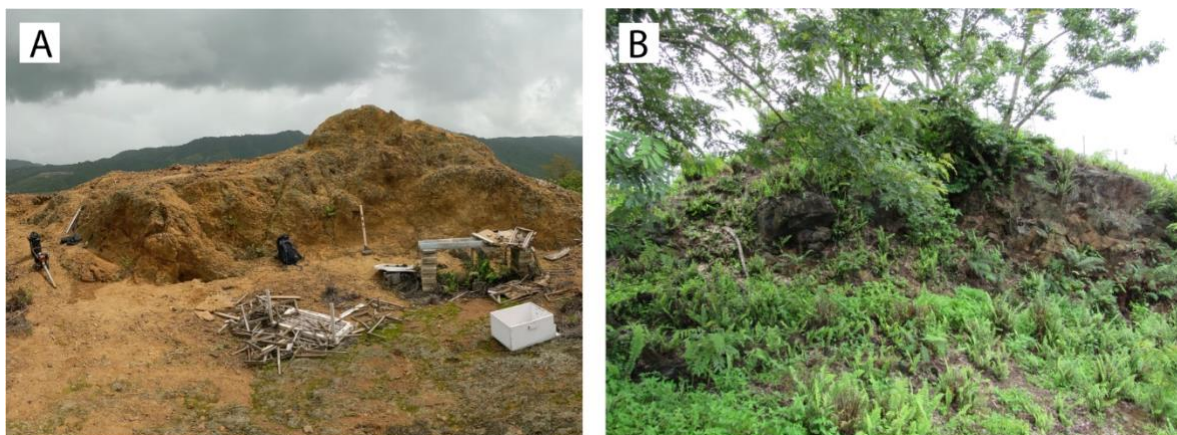


Figure 7: Field photos of the ore ridges on Cell Tower Hill. (A) The western extent of the northern ridge on the Cell Tower Hill. (B) The eastern extent of the southern ridge by the cell tower.



Figure 8: Field photo of a quartz pocket in sample KS-17 taken from a section of the northern ridge that borders the alteration zone seen in Figure 9A.

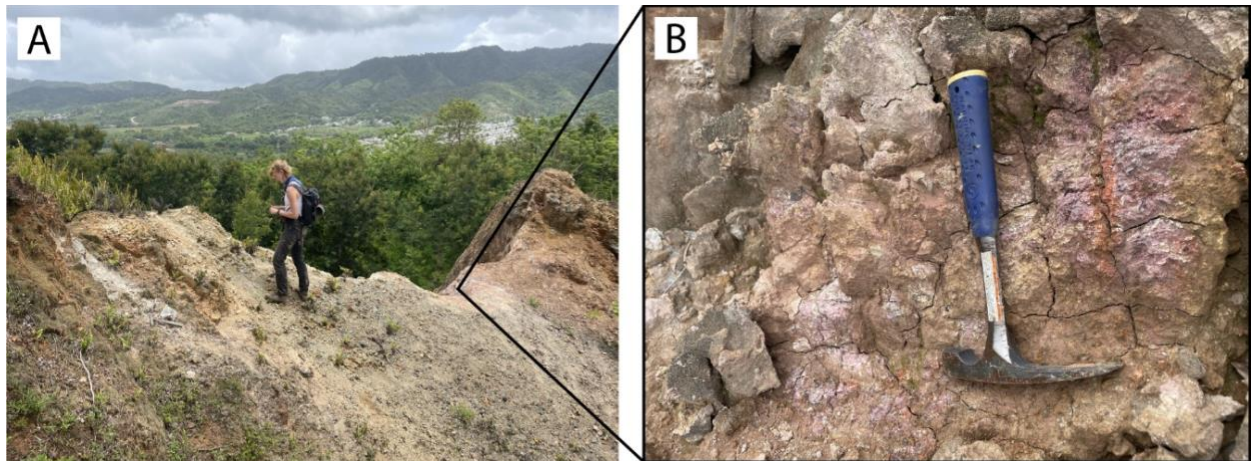


Figure 9: (A) Field photo of variable clay mineralogy between north and south ridge. Sample KS-17 (Figure 8) was extracted from the ore outcrop in the right-most side of this photo. (B) Field photo of pink alteration and where sample KS-22 was extracted.



Figure 10: Field photo of previously unmapped and undated local igneous intrusion (Figure 6) by the East Hill, hosted in weakly magnetic volcanoclastics with cross-cutting felsic dikes.

5. Methods

5.1 Sample Collection

Twenty-five samples were collected of the ore, weathered product, alteration, host rock, and local igneous intrusions (Table 1). There were 15 additional samples available from collaborators at UPRM and earlier work by Barefoot, 2021. Four samples from the earlier field work were available as thin sections although the GPS coordinates are not available for three of them (Table 1, “spatially unconstrained samples”). A portable core drill was used to collect three of the 40 total samples, allowing for minimally weathered samples to be obtained (Figure 11). Samples were targeted with the goal of building a spatially constrained sample set representative of the range of ore compositions and weathering extent across the entirety of the Keystone skarn.

Table 1: Characteristics and locations of all samples collected or analyzed in this study. The first 25 samples were collected in 2022 (“spatially constrained samples”). Samples collected from Keystone in 2020 are missing coordinates and are listed at the end (“spatially unconstrained samples”). *KS-08 was extracted by hammer in 2022 from the same location as the core sample extracted in 2020 (20KS-08 at the bottom).

Sample	Sample Description	Area	Coordinates	
<i>Spatially constrained samples:</i>				
KS-08*	Ore	Cell Tower Hill	18.23110°N	65.89754°W
KS-15	Ore	Cell Tower Hill	18.23084°N	65.89687°W
KS-16	Alteration	Cell Tower Hill	18.23095°N	65.89714°W
KS-17	Ore	Cell Tower Hill	18.23107°N	65.89725°W
KS-18	Ore	Cell Tower Hill	18.23095°N	65.89788°W
KS-19	Ore	Cell Tower Hill	18.23089°N	65.89761°W
KS-20	Weathered Ore (Drill Core)	Cell Tower Hill	18.23088°N	65.89765°W
KS-21	Alteration	Cell Tower Hill	18.23117°N	65.89759°W
KS-22	Alteration	Cell Tower Hill	18.23105°N	65.89750°W
KS-23	Alteration	Cell Tower Hill	18.23114°N	65.89757°W
KS-24	Alteration	Cell Tower Hill	18.23090°N	65.89735°W
KS-25	Weathered Product of Ore	Cell Tower Hill	18.23090°N	65.89735°W
KS-26	Ore (Drill Core)	Cell Tower Hill	18.23110°N	65.89754°W
KS-27	Host Rock	Cell Tower Hill	18.23196°N	65.89841°W
KS-28	Host Rock	Cell Tower Hill	18.23167°N	65.89861°W
KS-29	Host Rock	Cell Tower Hill	18.23017°N	65.89385°W
KS-30	Host Rock	Cell Tower Hill	18.23268°N	65.89709°W
KS-31	Igneous Intrusion	Cell Tower Hill	18.23288°N	65.89390°W
KS-32	Altered Host Rock	Cell Tower Hill	18.23288°N	65.89390°W
KS-33	Igneous Intrusion (veins)	East Hill	18.22544°N	65.88889°W
KS-34	Host Rock	East Hill	18.22544°N	65.88889°W
KS-35	Host Rock	East Hill	18.22544°N	65.88889°W
KS-36	Igneous Intrusion	East Hill	18.22544°N	65.88889°W
KS-37	Weathered Product of Igneous Intrusion	East Hill	18.22544°N	65.88889°W
KS-38	Ore	East Hill	18.22875°N	65.89248°W
<i>Spatially unconstrained samples and earlier drill core:</i>				
20KS-02	Ore	Cell Tower Hill	-	-
20KS-03	Ore	Cell Tower Hill	-	-
20KS-05	Ore	Cell Tower Hill	-	-
20KS-08	Ore (Drill Core)	Cell Tower Hill	18.23110°N	65.89754°W

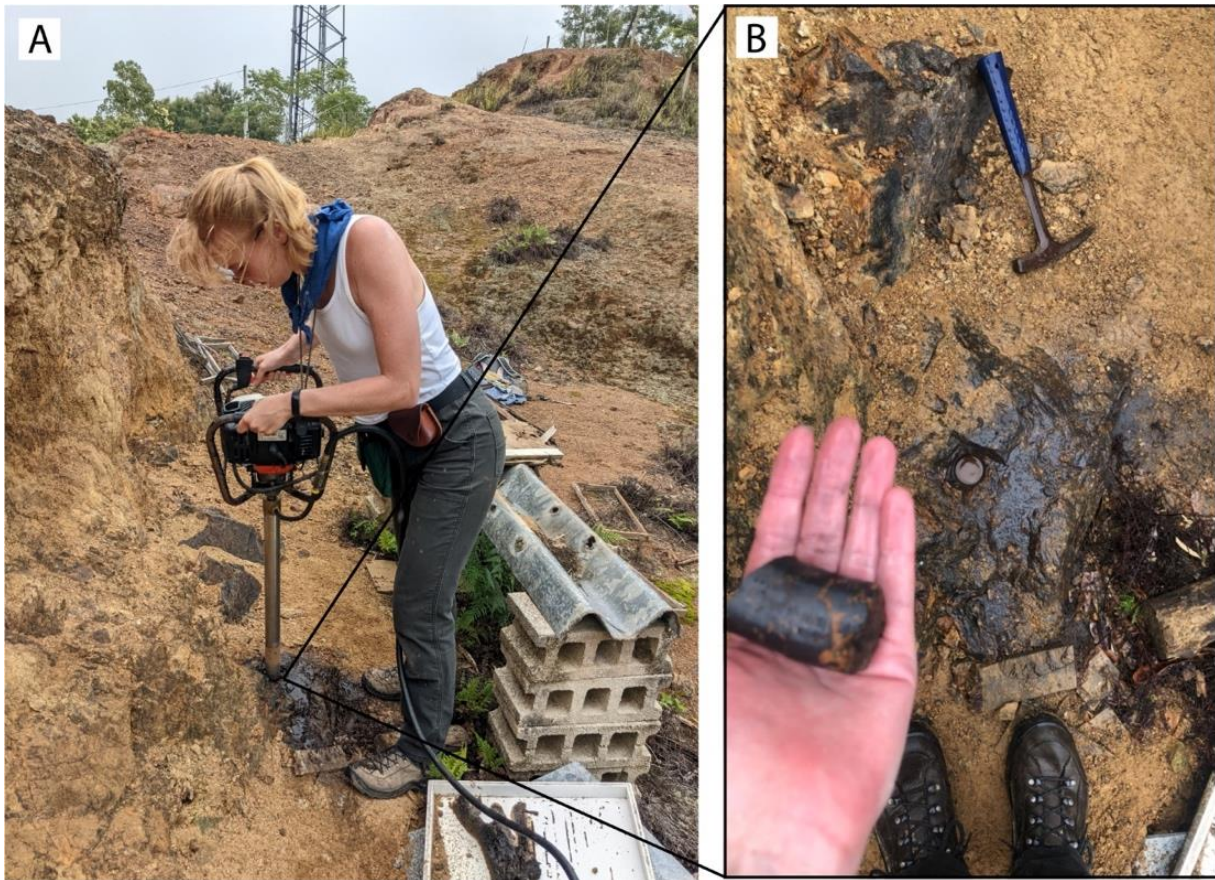


Figure 11: (A) Field photo of the portable core drill in use. (B) Rock core acquired of sample KS-26 and corresponding hole in the outcrop.

5.2 Petrography

Hand samples of ore, alteration, and host rock were examined, and thin sections were made of the ore from the Keystone skarn. Thin sections were analyzed and photographed using a Nikon Eclipse Ci POL petrographic microscope paired with a DS-Ri2 camera and NIS-Elements BR imaging software in the Department of Geosciences at AU. Transmitted light (plane-polarized light, PPL; cross-polarized light, XPL) and reflected light (RL) microscopy techniques were used; transmitted light allows for the identification of transparent minerals while reflected light permits the identification of opaque minerals such as oxides (magnetite, hematite) and sulfides. Relative abundance and textures of individual minerals, relationships between grains,

crystal size, and the presence of fluid inclusions were described. False color was applied to some RL images using the ImageJ software, to discern subtle changes within magnetite. Powdered X-Ray Diffraction (XRD) was also performed as a secondary check on mineral identification (Appendix A, Supplemental Figure A1).

5.3 Major and Trace Element Geochemistry

5.3.1 Laser Ablation-Inductively Coupled Plasma-Mass Spectrometry

Twelve ore dominated thin sections, four from 2020 field work by colleagues at UPRM, and eight spatially constrained samples from 2022 field work, were analyzed for their trace element compositions at AU using Laser Ablation-Inductively Coupled Plasma-Mass Spectrometry (LA-ICP-MS). The laser ablation system is a 193 nm Excimer laser (NWR193 by Elemental Scientific Lasers) attached to an Agilent 7900 ICP-MS. The LA-ICP-MS was the primary instrument used to quantify the abundance of trace elements due to its low detection limit and ability to simultaneously measure the entire suite of elements. Iron content measured by Electron Microprobe Analyzer (EMPA) at AU was used as an internal standard to process the LA-ICP-MS data. The analytical methods used for LA-ICP-MS and EMPA followed the procedures of Dare et al. (2014) and Barefoot (2021). Elements of interest were chosen based on expected substitutions in Fe oxide ore minerals (i.e., magnetite) and their ability to identify deposit type, metal source, compositional changes during mineral precipitation, and mineral heterogeneity such as fluid or other inclusions (Dupuis and Beaudoin, 2011; Dare et al., 2014; Nadoll et al., 2014; Nadoll et al., 2015). The concentrations of ^{23}Na , ^{24}Mg , ^{25}Mg , ^{27}Al , ^{29}Si , ^{43}Ca , ^{44}Ca , ^{47}Ti , ^{49}Ti , ^{51}V , ^{52}Cr , ^{53}Cr , ^{55}Mn , ^{56}Fe , ^{57}Fe , ^{59}Co , ^{60}Ni , ^{63}Cu , ^{66}Zn , ^{71}Ga , and ^{118}Sn were measured during LA-ICP-MS analyses.

In preparation for the analyses, whole thin sections were photographed using a camera-equipped Leica S9i stereoscope and stitched together using Adobe Photoshop. Areas of interest for spot and line analyses of trace elements were identified on these thin section maps using a petrographic microscope. Spot and line dimensions were chosen based on the width of the grain (<10 microns), amount of inclusions, and extent of alteration. Spots/lines were placed predominantly on minimally contaminated ore when possible. Lines were primarily placed across grains to evaluate whether the trace element composition of the mineral changed. The placement of the spots/lines were photographed at a scale of 10-100 microns utilizing the laser system's ActiveView 2 software and roughly labeled on the thin section maps to aid in later EMPA set up. The amount of alteration of the magnetite within each analysis area was noted (e.g., magnetite altered to hematite).

Synthetic glass standards NIST 610 and 612 from the National Institute for Standards and Technology (NIST; National Institute of Standards and Technology, 2012a, 2012b) and the Columbia Basalt glass standard BCR-2GA from the United States Geological Survey (USGS; U.S. Geological Survey, 2022b) were used as reference materials and analyzed at the beginning, middle, and end of each session. Preliminary analyses of one sample and NIST 612 were performed to refine the LA-ICP-MS conditions (Table 2). All spots and lines were pre-ablated before the batch was run to remove any impurities on the surface of the thin sections. The iolite v.4 software (Elemental Scientific Lasers) was used to process LA-ICP-MS data from counts detected per second into concentrations (Woodhead et al., 2007; Paton et al., 2011). The limits of detection were determined following Howell et al. (2013); NIST 610 was set as the primary standard and NIST 612 was used as the secondary standard (Nadoll et al., 2014). Calcium mass 44 and ^{57}Fe were used as internal standards for reference materials and ore samples, respectively

(Dare et al., 2014). The ^{57}Fe concentrations used for internal standard values in final data processing were obtained by EMPA. Dwell time was 20-30 seconds to minimize contamination from thin section glass and/or other minerals. Samples collected in 2020 (20KS-02, 20KS-03, 20KS-05, 20KS-08) and 2022 had a dwell time of 30 seconds and 20 seconds, respectively. Concentrations of trace elements in magnetite were measured 3-11 times within each thin section and values were averaged. Spots in grains that were heavily altered or had high standard deviations were not included within the averages in order to compare Keystone magnetite to published data for magnetite.

Table 2: LA-ICP-MS conditions used for analysis.

	Type of analysis	Spot Size (microns)	Frequency (Hz)	Dwell Time (sec)	Energy (J/cm ²)
Standard	Spot	30	16	20-30	2.69
	Line	30	16	1	2.69
Sample	Spot	30	16	20-30	2.69
	Line	30	16	1	2.69
Pre-ablation	Spot	50	2	2	0.09
	Line	50	2	1	0.09

5.3.2 Electron Microprobe Analysis

The AU EMPA is a JEOL JXA-8600 with secondary electron (SE) and backscattered electron (BSE) detectors and four wavelength dispersive spectrometers (WDS). All analyzed thin sections were carbon coated in house prior to analysis. WDS spot and line analyses and elemental maps were used to quantify changes in elemental concentrations across ore mineral grains, with a focus on Fe. The locations of EMPA analyses were chosen based on their proximity to magnetite grains that were ablated during LA-ICP-MS. Ablation locations were previously located using a petrographic microscope, photographed, and mapped on printed thin section images for EMPA analyses. Two to three WDS spots were taken near ablation spots/lines

and averaged to determine sample Fe concentration for final LA-ICP-MS data processing. Elemental maps were acquired to identify Fe, Si, Al, Ti or Ca variations within samples. BSE imaging was utilized to identify phases, textures, and zonation. Zonation was quantified via WDS spots and lines. For all EMPA analyses, the magnetite standard NMNH 114887 from the Smithsonian National Museum of Natural History was analyzed at the beginning and end of each session (Appendix B, Table B1; Jarosewich et al., 1980a, 1980b). These magnetite analyses were based on standards in Table 3 and ZAF matrix corrections. Spot analyses and line transverses were performed via WDS under beam conditions of 15kV and 20nA. BSE images and WDS maps were acquired under beam conditions of 15kV and 50.5nA with 600-400 pixels per line with a 20 second dwell time. False color was applied to elemental maps using the ImageJ software, to discern subtle changes in concentrations.

Table 3: EMPA setup for each element of interest including the mineral formula assumed during data processing, standard, crystal, and WDS spectrometer number.

Element	Formula	Standard	Crystal	WDS Spectrometer
Mg	MgO	Olivine	TAP	1
Al	Al ₂ O ₃	Anorthite	TAP	2
Si	SiO ₂	Wollastonite	TAP	2
Ca	CaO	Wollastonite	PET	3
Ti	TiO ₂	Ilmenite	PET	3
Cr	Cr ₂ O ₃	Chromite	LIF	4
Fe	Fe ₃ O ₄	Magnetite	LIF	4
Mn	MnO	Garnet	LIF	4
Na	Na ₂ O	Albite	TAP	1
V	VO ₂	Vanadium Wire	PET	3

5.4 Isotope Geochemistry

5.4.1 Stable Fe Isotope Analysis

The stable Fe isotope composition of eight Keystone magnetite samples were measured on a Nu Plasma 1700 Multi-Collector Inductively Coupled Mass Spectrometer (MC-ICP-MS) in the Pacific Centre for Isotopic and Geochemical Research (PCIGR) at the University of British Columbia (UBC). All analyses were performed in dry plasma mode using a DSN-100. In preparation for the analyses at the UBC, magnetite-rich ore samples were picked and crushed into a fine powder. Using a Lecia S9i Stereoscope and up to 55x magnification, impurities (e.g., quartz grains) and larger pieces were removed from the powder and the extent of oxidation was estimated and recorded (Table 4). Around 2mg of powdered magnetite ore and 8ml of *aqua regia* (1HNO₃:3HCl) were combined in capped 15ml Savillex vials and heated at 120°C until samples completely dissolved. Samples were uncapped, dried down, and resealed with Parafilm around the cap for safe transportation to UBC.

Table 4: Estimated extent of oxidation of each magnetite powder sample.

Sample Name	Estimated extent of oxidation
KS-08	Mild to moderate
KS-15	Moderate
KS-17	Not to mild
KS-18	Mild
KS-19	Not to mild
KS-25	Heavily
KS-26	Not
KS-38	Mild

In the clean laboratories at PCIGR, which include class 100 fume hoods within a class 1000 clean room, samples were prepared to be analyzed by the MC-ICP-MS. First, samples were redissolved into approximately 10ml of 7N HCl overnight at 120°C in capped Savillex vials. They were then uncapped and dried down before being redissolved into 1ml 7N HCl for column chromatography. Following the procedure of Bilenker et al. (2018), clean BioRad AG MP-1M resin (100-200 mesh) was loaded into clean 5ml BioRad columns. The resin was conditioned with 10ml HCl before the dissolved samples were loaded. Then, 25ml of HCl was passed through the columns to remove matrix elements. Clean Savillex vials were placed under each column and Fe was eluted from the resin with a solution of 1N HF + 0.5N HCl. The samples were dried down at 120°C and redissolved and dried down in 500µl of 2% HNO₃ two times, then dissolved in 10ml of 2% HNO₃ for MC-ICP-MS analysis.

Next, the stable Fe isotope compositions were measured by using the Nu Plasma 1700 MC-ICP-MS. The Nu 1700 measures Fe isotope abundances at such high resolution that ⁵⁴Fe, ⁵⁶Fe, and ⁵⁷Fe are fully separated from their isobaric interferences (⁴⁰Ar¹⁴N, ⁴⁰Ar¹⁶O, ⁴⁰Ar¹⁶O¹H). Chromium with a mass of 54 was subtracted from the ⁵⁴Fe signal by monitoring ⁵²Cr, through a correction performed by the MC-ICP-MS software. Standard-sample bracketing was used such that IRMM-14, a synthetic Fe standard produced by the Institute for Reference Materials and Measurements, was analyzed before and after every sample and reference material. The USGS reference material BCR-2 (Columbia River Basalt) was processed and analyzed alongside the samples to check for accuracy throughout the run sessions. Iron concentrations were matched between the reference material, samples, and standard within 10% by diluting with 2% HNO₃; the goal ⁵⁶Fe signal was approximately 10V. Each sample was analyzed at least three times and the results are reported relative to IRMM-14 following Equation 1:

$$\delta^{56}\text{Fe} (\text{‰}) = [({}^{56}\text{Fe}/{}^{54}\text{Fe})_{\text{sample}} / ({}^{56}\text{Fe}/{}^{54}\text{Fe})_{\text{IRMM-14}} - 1] * 1000 \quad (\text{Eq. 1})$$

Mass dependent fractionation was monitored throughout the session (Appendix A, Supplemental Figure A2).

5.4.2 Stable O Isotope Analysis

From the same magnetite-rich ore powder that was used for Fe isotope analyses, around 2.5mg of sample and duplicates were sent to the lab of Dr. Ilya Bindeman at the University of Oregon, home to a MAT 253 gas Isotope Ratio Mass Spectrometer (IRMS). The IRMS is connected to a custom laser fluorination line that is ideal for vaporizing oxide minerals and isolating the O₂ gas produced for isotopic measurement (Bilenker et al., 2016). The samples were pretreated overnight to eliminate alteration products such as goethite and clays. The Gore Mountain garnet was analyzed alongside the magnetite samples to monitor for accuracy throughout the analytical session. Oxygen isotope ratios are reported relative to Standard Mean Ocean Water (SMOW) following Equation 2:

$$\delta^{18}\text{O} (\text{‰}) = [({}^{18}\text{O}/{}^{16}\text{O})_{\text{sample}} / ({}^{18}\text{O}/{}^{16}\text{O})_{\text{SMOW}} - 1] * 1000 \quad (\text{Eq. 2})$$

6. Results

6.1 Petrography of the Keystone Fe Ore

The Keystone Fe ore makes up 65-25% of each sample and is dominantly magnetite with a range of euhedral to anhedral grains that are massive to tabular containing variable amounts of martite (hematite pseudomorph after magnetite; Figure 12), vesicles (<200µm), fractures, and zonation (Table 5, Figures 12, 13). Smaller sections of hematite, and minute amounts of goethite (<2%; Figure 13A, C) and maghemite (<1%; Figure 13D) were identified within or near magnetite. Martite forms along the edges and center of magnetite grains and tends to be associated with areas of high porosity and fractures. Areas of complete martitization, often in the

center of magnetite grains, display a sponge-like texture (Figures 12B, E, 13C). Martite tends to form a cross-hatched pattern (Figure 13C, D) that can follow zonation within the magnetite grain. Along with martite, maghemite also displays the same hatched pattern and only appears beside martite (Figure 13D). Goethite occurs in fractures and vesicles within magnetite and forms in areas with high proportions of martite (Figure 13A, C). Specular hematite is hosted within quartz encompassed by magnetite (Figure 13B).

Table 5: Petrographic observations of Keystone ore including habit, amount of martite, amount of vugs/vesicles, portion of fractures, and geochemical zonation.

Sample	Texture & Habit(s)	Estimated % Martite	Estimated % Vugs/Vesicles	Relative Proportion of Fractures	Zonation Observed?
KS-08	Massive, anhedral	5	30	Highly fractured	Yes
KS-15	Massive, euhedral-subhedral	50	25	Minimally fractured	No
KS-17	Massive, subhedral	5	10	Moderately fractured	No
KS-18	Tabular/needle-like	20	15	Minimally Fractured	No
KS-19	Massive, euhedral-subhedral	15	20	Minimally fractured	Yes
KS-25	Massive, anhedral	20	30	Highly Fractured	No
KS-26	Massive, subhedral	10	20	Moderately Fractured	Yes
KS-38	Tabular, euhedral	20	20	Moderately Fractured	Yes

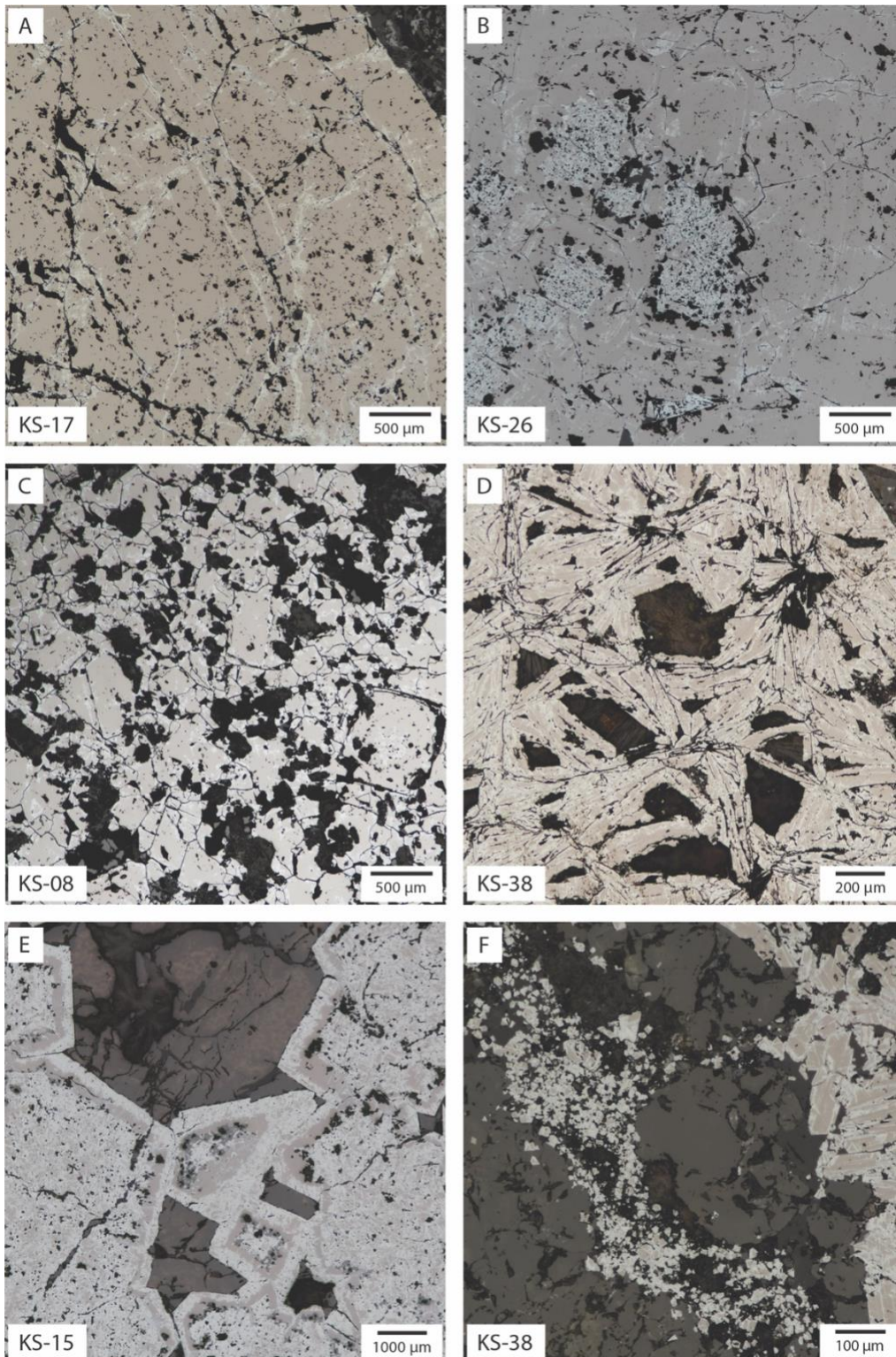


Figure 12: Reflected light (RL) observations of magnetite and Fe oxides. (A) RL image of massive magnetite with minor martite (white). (B) RL image of sponge-like martite (white) within massive magnetite. (C) RL image of highly vesicular and fractured magnetite with minor martite (white). (D) RL image of tabular magnetite with martite (white) and vesicles. (E) RL image of euhedral magnetite with extreme martite (white) forming along the edges and center of the grains. (F) RL image of small euhedral magnetites beside larger tabular magnetite, both with martite (white).

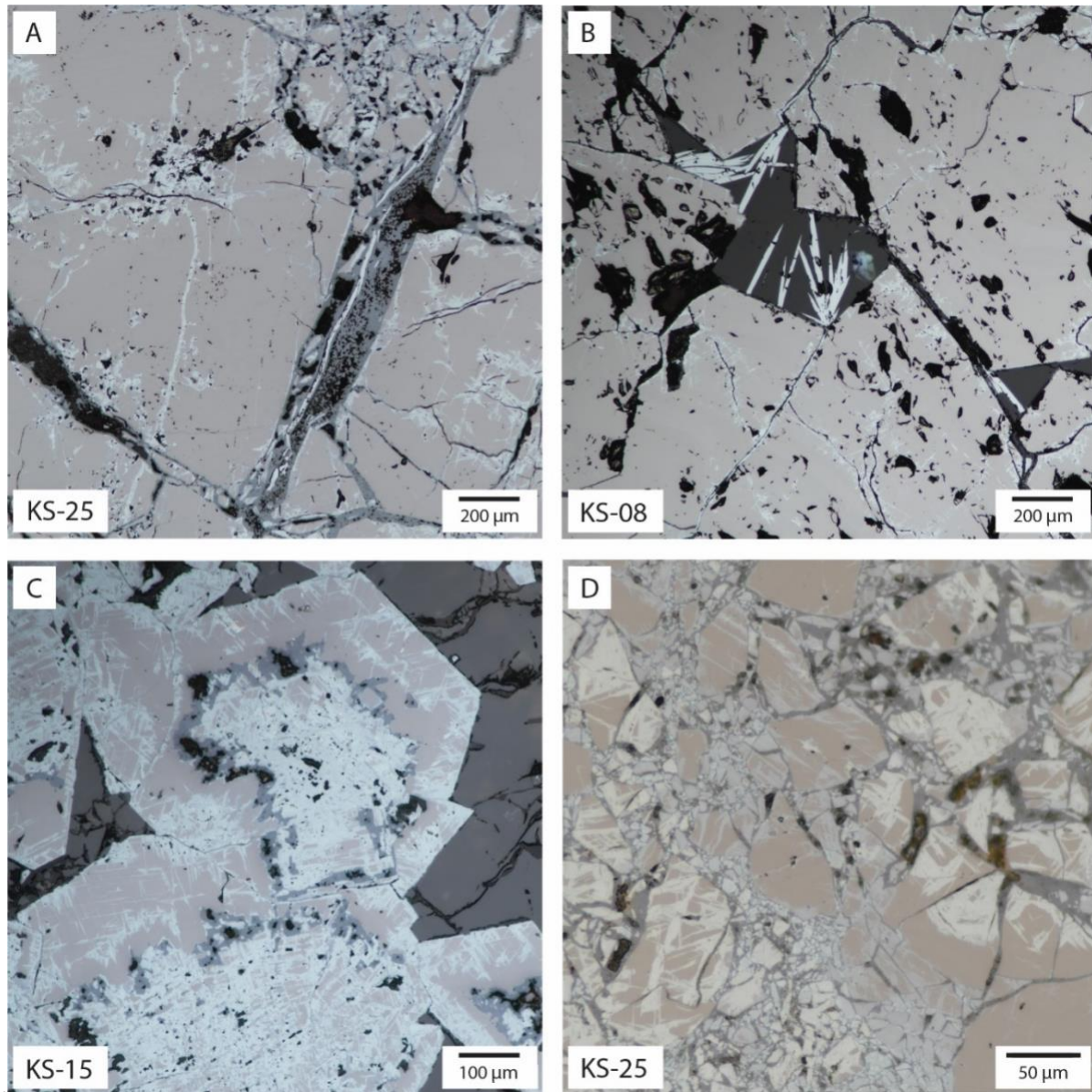


Figure 13: (A) RL image of fractured magnetite filled with hematite (white), goethite (grey), and silicates (black). (B) RL image of specular hematite (white) in quartz (dark grey) surrounded by magnetite. (C) RL image of sponge-like martite (white) and goethite (grey) centered in euhedral magnetite grains. (D) RL image of brecciated magnetite being replaced by maghemite (light grey/blueish tint) and martite (white) and goethite in fractures.

6.2 Geochemical Zonation of the Keystone Magnetite

Much of the Keystone magnetite ore is geochemically homogenous (Figure 14), but oscillatory and simple zonation were observed within four of the eight thin sections analyzed (Table 5). The changes between zones can be vaguely differentiated using reflected light

microscopy (Figures 15A, 16A, C, E) and clearly distinguished using false coloration produced by ImageJ on RL images (Figures 16B, D, F) or BSE imaging (Figure 15B). The zonation correlates to changes in trace amounts of Fe, Si, and Al such that higher Fe is associated with lower Si and Al and vice versa. These changes in geochemistry are based on EMPA elemental maps (Figures 15C, 17) and WDS spot and line analyses across the zonation (Figure 17, Table 6). Both magnetite and hematite were identified in RL but the differences in their Fe content were not detected in the WDS maps (e.g., Figure 14C).

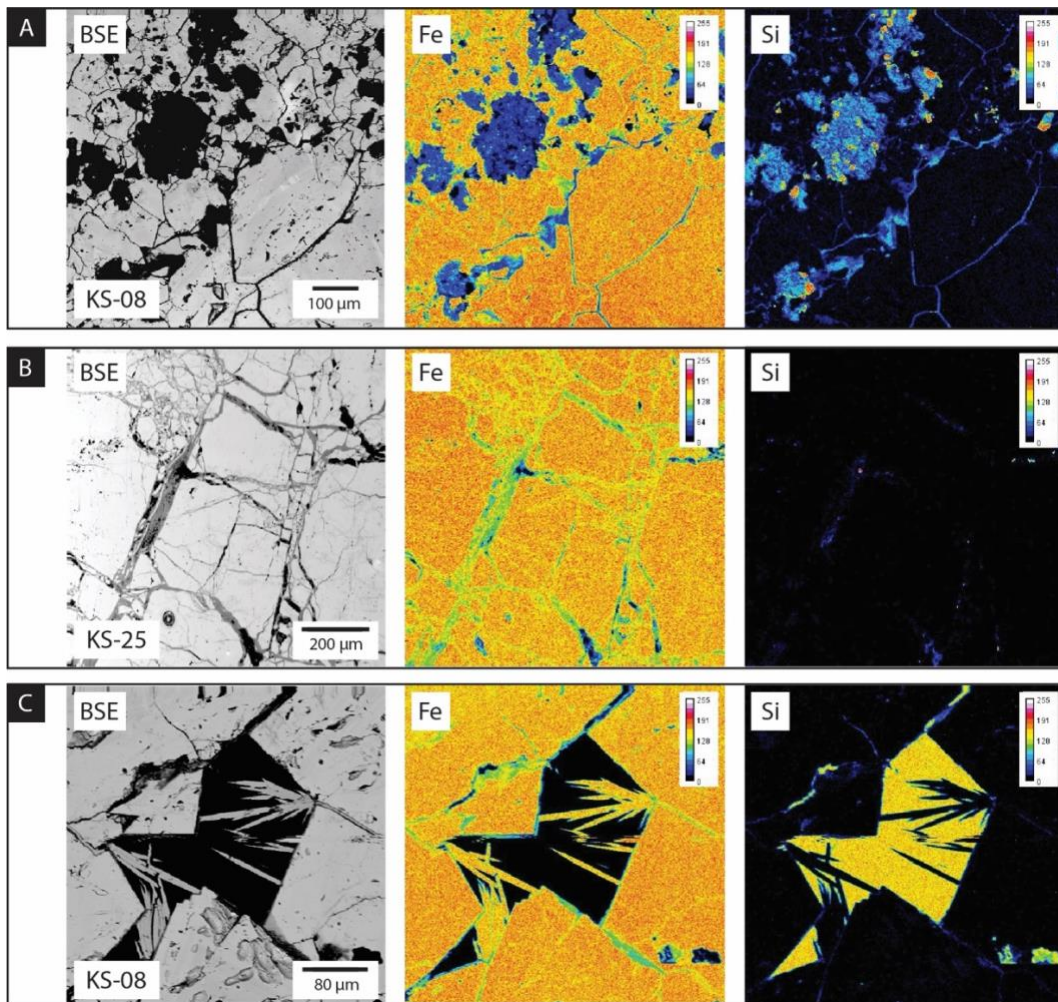


Figure 14: (A) BSE, Fe, and Si maps of fractured magnetite and garnet. (B) BSE, Fe, and Si maps corresponding to Figure 13A, with fractured magnetite with minor amounts of martite. Goethite and silicates fill the fractures. (C) BSE, Fe, and Si maps of specular hematite in quartz surrounded by magnetite (Figure 13B). The color scale bar in each WDS map (Fe and Si) represents the color assigned to counts for the characteristic x-rays, with 0 (black) representing the lowest concentration and 255 (white) the highest concentration. Warmer colors represent relatively higher counts compared to cooler colors.

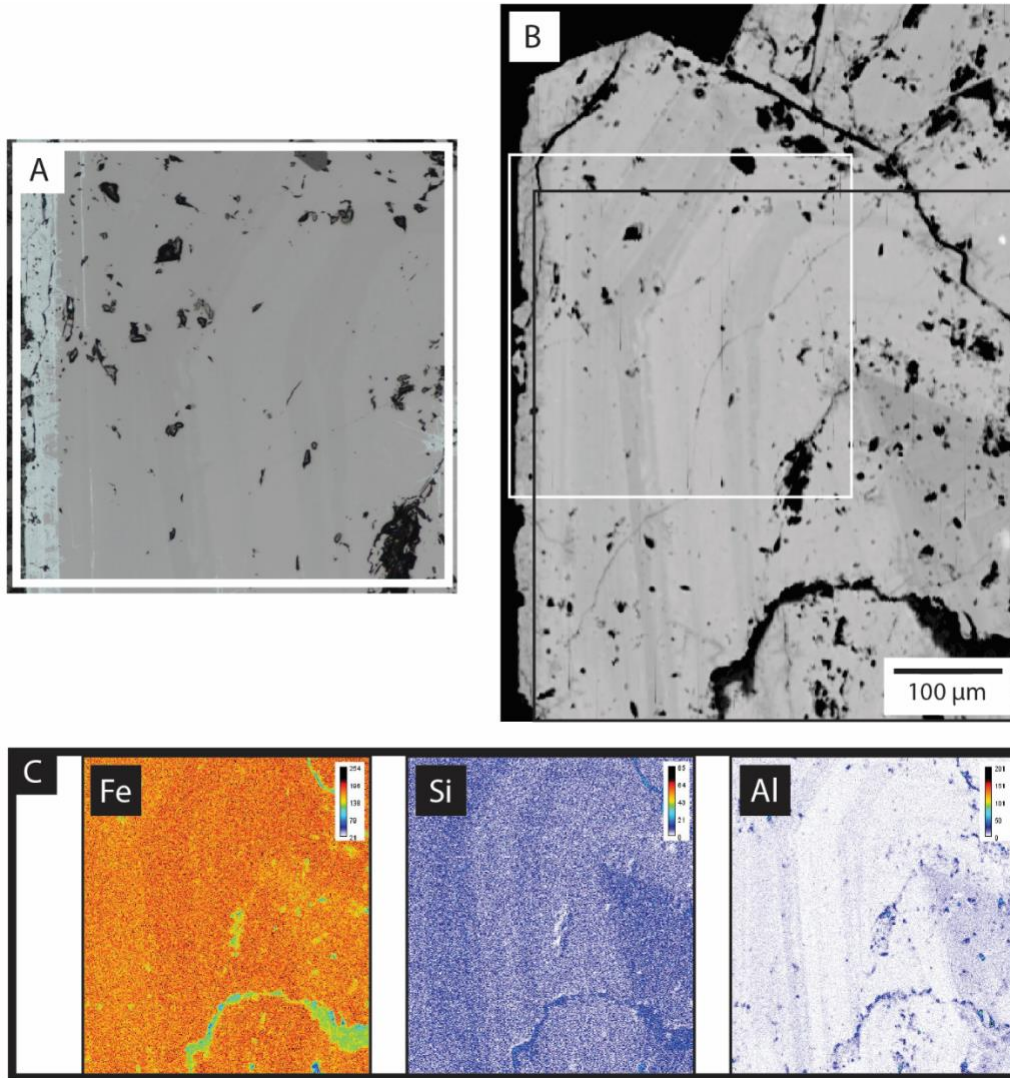


Figure 15: (A) RL image of oscillatory zoning along the edge of a euhedral magnetite grain from KS-19. (B) BSE image of oscillatory zoning. White box represents area of image in panel A. (C) WDS maps of Fe, Si and Al of oscillatory zoning from of the area outlined in black in panel B. Higher Fe is associated with lower Si and Al, and vice versa. The color scale bar in each WDS map (Fe, Si, and Al) represents the color assigned to counts for the characteristic x-rays with the cooler colors representing the lower concentrations and warmer colors representing higher concentrations.

Some truncations were also observed in RL within oscillatory zonation (Figures 16A, C).

Truncations are non-uniform structures such as curvatures that change in thickness and cut off one another. These textural features most likely correlate with changes in trace element concentrations (Figure 15). This is consistent with interpretations in the literature of truncations found commonly in Fe-bearing ore deposits like skarns (Hu et al., 2015; Dare et al., 2015) and

iron oxide-apatite deposits (Dare et al., 2015). However, defects in the magnetite structure cannot be ruled out as a cause of the truncations.

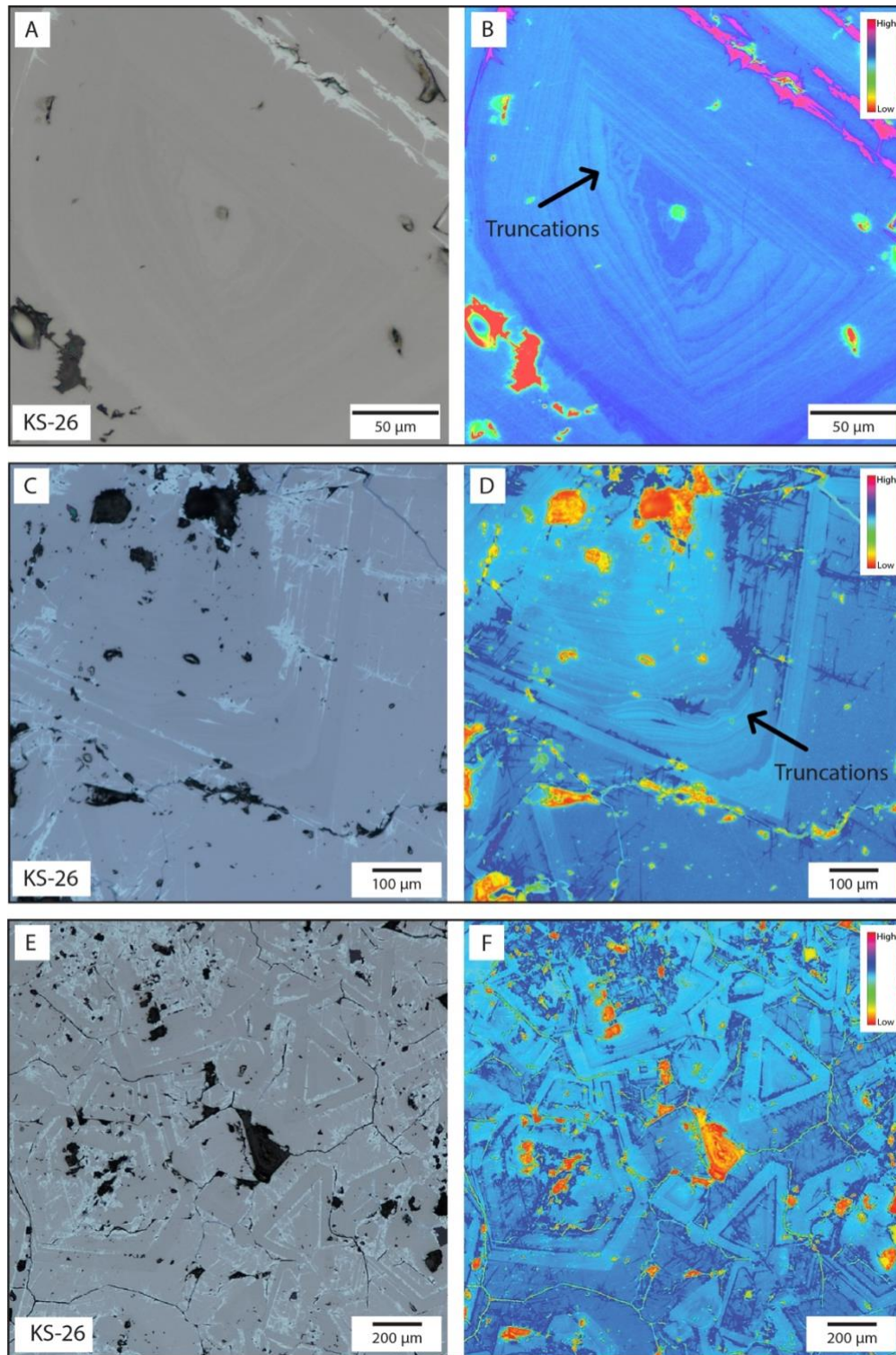


Figure 16: please see next page for caption.

Figure 16 (previous page): Reflected light and false color images of ore magnetite from KS-26. (A, C) RL images of oscillatory zonation exhibiting truncations. (B) False color enhancement of panel A made with ImageJ to highlight textural features. (D) False color enhancement of panel C made with ImageJ to highlight textural features. (E) RL image of zonation and martite aligned with the magnetite crystal habit. (F) False color enhancement of panel E made with ImageJ to highlight textural features. The color scale bar in each RL false color image (B, D, F) represents the color assigned to the RL image in grey scale; warm colors represent low reflectivity and cool colors represent high reflectivity.

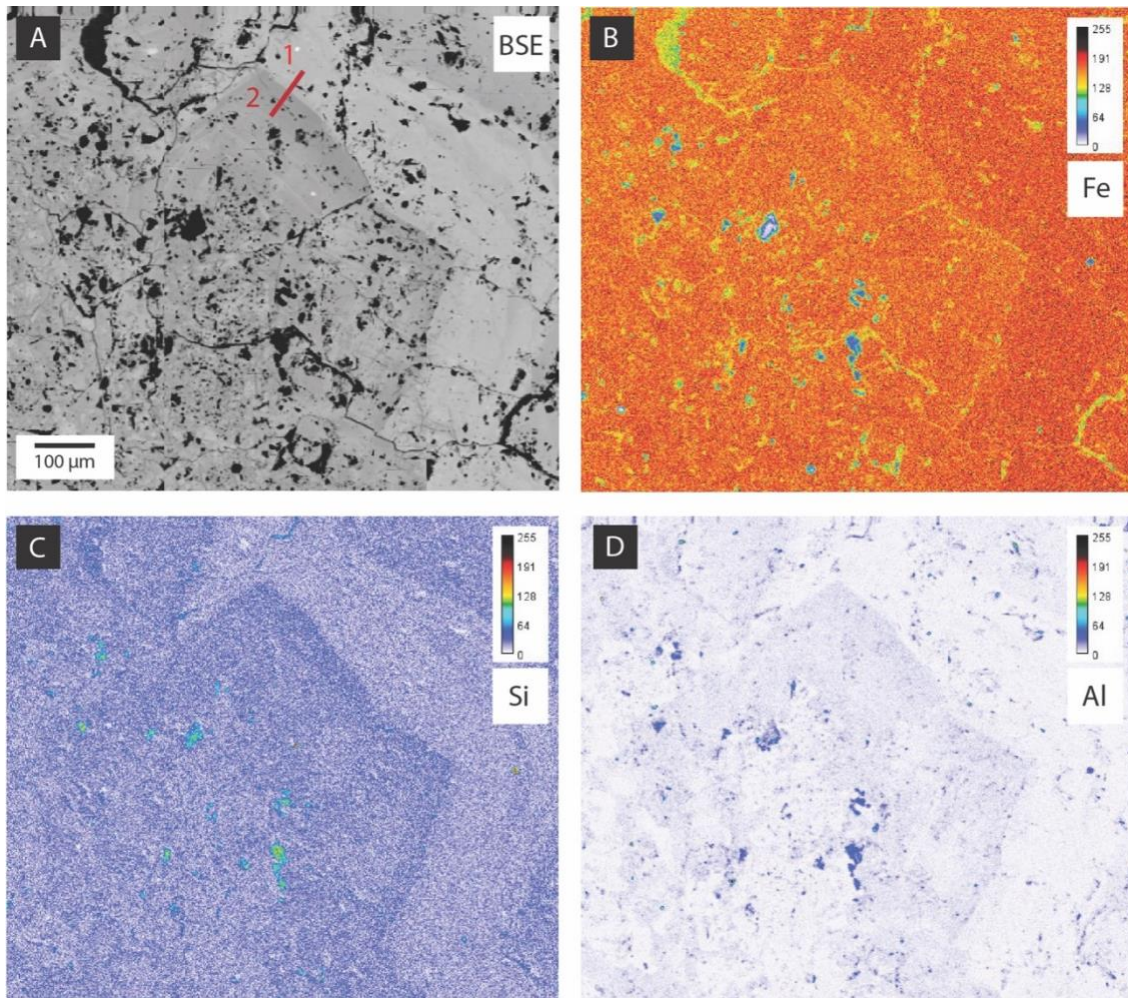



Figure 17: BSE image (A) and corresponding Fe, Si, and Al WDS maps (B, C, D, respectively) of zoned massive magnetite from KS-19. Higher Fe is associated with lower Si and Al, and vice versa. The location of two WDS spots are indicated by the red numbers 1 and 2 in the BSE image, and one line traverse is indicated by the arrow within the BSE image. Table 6 contains the Fe, Si, and Al concentrations measured during those analyses. The color scale bar in each WDS map (Fe, Si, and Al) represents the color assigned to counts for the characteristic x-rays with the cooler colors representing the lower concentrations and warmer colors representing higher concentrations.

Table 6: Iron, Si, and Al concentrations from a WDS line traverse and two WDS spots on KS-19. The line started in the light grey magnetite and ended in the dark grey, as noted by the red line in Figure 17A. The two WDS spots, indicated as “1” and “2” in Figure 17A, were located in the light grey and dark grey magnetite, respectively.

Type of WDS Analysis	Greyscale on BSE	Fe (wt%)	Si (wt%)	Al (wt%)
Line Start	Light grey	70.69	0.14	0.24
	Light grey	71.12	0.16	0.34
	Light grey	70.28	0.23	0.47
	Dark grey	67.6	1.32	0.98
Line End	Dark grey	68.42	0.83	0.74
Spot 1	Light grey	70.76	0.12	0.22
Spot 2	Dark grey	67.78	0.89	0.71

6.3 Observations of Non-Ore Minerals

Garnet, quartz, and chlorite were observed across the seven spatially constrained thin sections of Fe ore (Figure 18). Epidote was observed in one sample from the East Hill (KS-38). Malachite and pyrite were also identified in the field and in thin sections from spatially unconstrained samples. Samples collected from the Cell Tower Hill were mineralogically zoned radiating outwards from the ore (Figure 18A). Highly fractured, birefringent garnet is typically adjacent to the ore, which can be brecciated with Fe-hydroxide and or chlorite between fractures (Figure 18E). Quartz-hosted spherical chlorite outlines the garnet-quartz boundary in samples KS-19, KS-18, and KS-26. Epidote and minimal quartz were observed in KS-38 (collected at the East Hill) with no garnet or chlorite. Between Fe ore grain boundaries, altered non-ore minerals and vesicles occur (Figures 12, 14). The garnet present in Keystone ore samples is birefringent and zoned in XPL (Figure 18A, B), consistent with the observations of optical anomalies and twinning by Fettke (1924) and work at the Tibes Fe skarn in southern Puerto Rico (Giovannetti-Nazario, 2022).

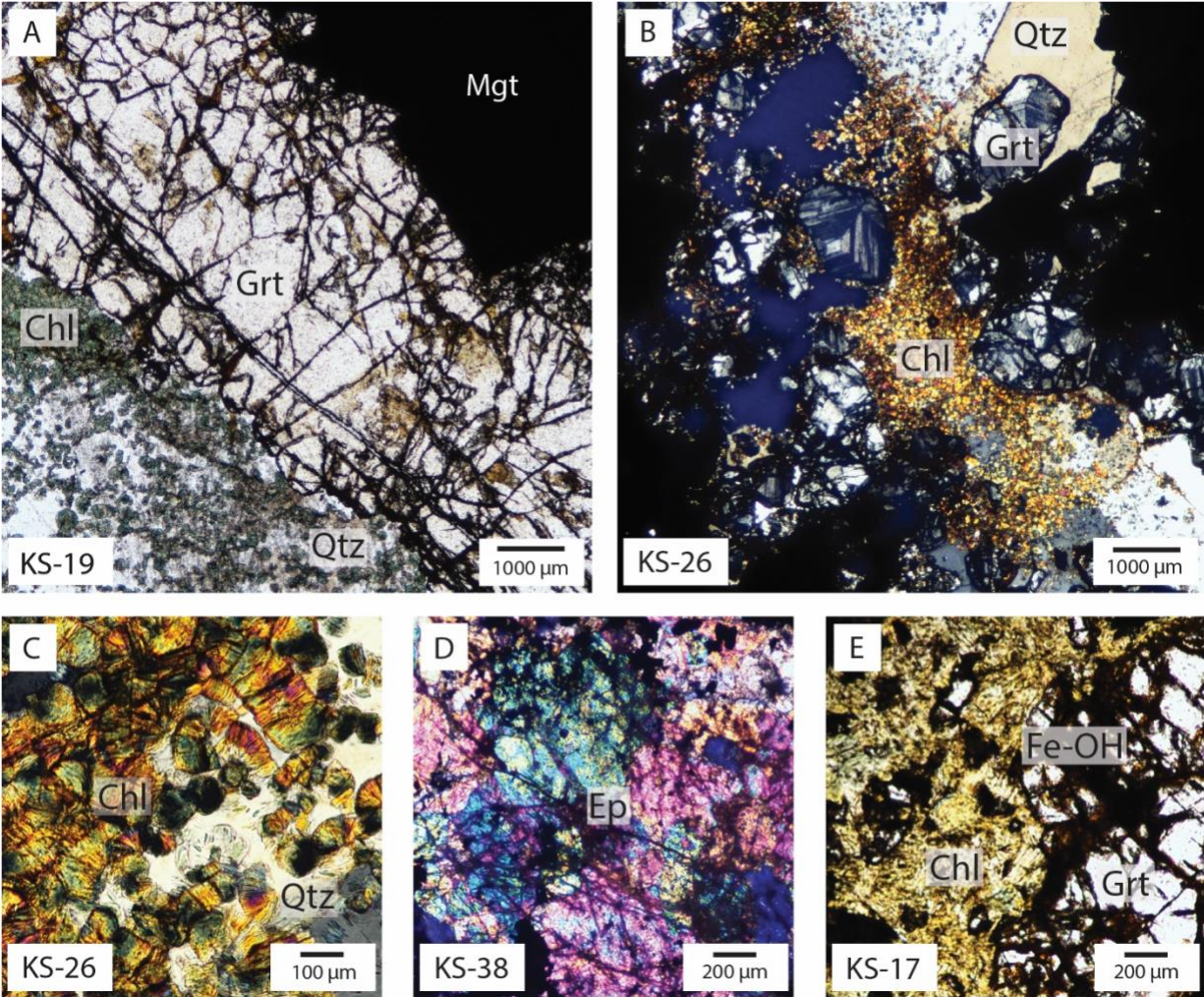


Figure 18: (A) PPL image of representative mineralogical zonation seen in all samples except KS-38. Zonation consists of magnetite (Mgt; opaque) followed by fractured garnet (Grt), and spherical chlorite (Chl; green) in quartz (Qtz). (B) XPL image centered on spherical chlorite in quartz surrounded by zoned garnets enclosed by magnetite (opaque) (C) XPL image of spherical chlorite in quartz. (D) XPL image of epidote (Ep). (E) PPL image of chlorite (green) and Fe-hydroxide along fractured garnet (clear).

6.4 Iron Content and Trace Element Composition of Keystone Magnetite Ore

The Fe content of eight spatially constrained ore samples measured by EMPA range from 63.81 to 71.70wt% (summarized in Table 7 with a full dataset in Appendix B, Table B2).

Differences in Fe concentration within magnetite and the other Fe oxides were not significant (Figure 14). The average trace element composition of these eight samples (Table 8) plus four spatially unconstrained ore samples were determined by LA-ICP-MS and makeup <2wt% within magnetite. KS-08, KS-17 and KS-25 contain the highest concentrations of Si, Al, and Ca. KS-25 contains the highest Al, Si, and Mn content. The full LA-ICP-MS trace element dataset is reported in Appendix C, Table C4. The ThO/Th ratios measured during the three sessions of LA-ICP-MS ranged from 0.102% to 0.233%.

Table 7: Iron concentrations (wt%) for Keystone magnetite determined by EMPA based on seven or more analyses, see Appendix B, Table B2 for details.

Fe (wt%)	KS-08	KS-15	KS-17	KS-18	KS-19	KS-25	KS-26	KS-38
Minimum	63.87	67.16	68.29	68.31	68.9	63.81	66.96	67.22
Maximum	67.29	71.70	70.8	71.72	70.97	67.17	70.86	70.72
Average	65.28	69.93	69.63	70.75	70.09	65.50	69.33	69.48

Table 8: Average trace element concentrations (ppm) in Keystone magnetite determined via LA-ICP-MS based on eight or more analyses. Chromium, Cu, and Sn analyses were often below the limit of detection (<LOD). See Appendix C, Table C4 for details.

	KS-08	KS-15	KS-17	KS-18	KS-19	KS-25	KS-26	KS-38
²³ Na	792	325	1018	187	114	1207	115	424
²⁴ Mg	2099	843	2782	347	607	2928	248	505
²⁷ Al	6945	2161	7148	762	2688	8854	2358	2759
²⁹ Si	8045	5283	9879	4939	2210	11088	1920	6960
⁴⁴ Ca	3108	1243	3527	822	463	3518	490	1538
⁴⁷ Ti	1052	337	419	73	1326	732	874	290
⁵¹ V	145	153	124	232	208	130	144	276
⁵² Cr	48	28	9	163	420	93	13	30
⁵⁵ Mn	1259	838	1369	756	1215	2069	926	854
⁵⁹ Co	73	57	109	251	71	96	53	72
⁶⁰ Ni	18	21	5	23	13	10	10	42
⁶³ Cu	63	549	121	1126	<LOD	16	112	66
⁶⁶ Zn	304	226	328	122	262	314	138	120
⁷¹ Ga	10	4	10	3	3	13	3	2
¹¹⁸ Sn	5	9	1	1	0	0	1	9

6.5 Stable Fe and O Isotope Composition of Magnetite ore from the Keystone Skarn

The $\delta^{56}\text{Fe}$ values of eight Keystone samples of magnetite ore (with two duplicates) range from $-0.12\text{‰} \pm 0.03$ to $0.21\text{‰} \pm 0.04$, with an average $\delta^{56}\text{Fe}$ value for Keystone ore of 0.02‰ ($n=10$; Table 9). The BCR-2 reference material measured during the analytical session had a $\delta^{56}\text{Fe}$ value of $0.09\text{‰} \pm 0.03$ ($n=4$) relative to IRMM-14, which is within error of the accepted $\delta^{56}\text{Fe}$ value ($0.09 \pm 0.011\text{‰}$, Craddock and Dauphas, 2011). The undiluted blank value was 0.069‰ , negligible compared to the sample solutions that were diluted to a 10V signal.

The $\delta^{18}\text{O}$ values of the same eight Keystone magnetite ore samples (with seven duplicates) range from $0.10\text{‰} \pm 0.07$ to $2.00\text{‰} \pm 0.07$ with an average $\delta^{18}\text{O}$ value of 1.56‰

(n=15) (Table 10). The Gore Mountain Garnet in-house standard yielded a $\delta^{18}\text{O}$ value range of 6.22‰ \pm 0.07 to 6.71 ‰ \pm 0.07), which encompasses the expected value of 6.52‰ (Bilenker et al., 2016).

Table 9: The Fe isotope composition of Keystone magnetite samples. Where both A and B samples are listed, they correspond to duplicate aliquots of the same sample powder.

Sample	Average $\delta^{56}\text{Fe}$ (‰)	$\pm 2\sigma$	n
KS-08A	0.08	0.02	4
KS-15A	0.21	0.04	3
KS-17A	-0.07	0.02	2
KS-17B	-0.08	0.02	5
KS-18A	0.12	0.07	3
KS-19A	-0.12	0.03	2
KS-25A	-0.05	0.04	3
KS-26A	0.10	0.02	2
KS-26B	0.01	0.04	5
KS-38A	0.04	0.05	3

Table 10: The O isotope composition of Keystone magnetite samples. Where there are sample names that end in both C and D, they were duplicates. These samples came from the same powder used for Fe isotope analyses (they correspond to the same sample numbers ending in A and B in Table 9).

Sample	Average $\delta^{18}\text{O}$ (‰)	$\pm 2\sigma$
KS-08C	2.00	0.07
KS-08D	1.98	0.07
KS-15C	1.52	0.07
KS-15D	1.50	0.07
KS-17C	1.73	0.07
KS-17D	3.14	0.07
KS-18C	1.13	0.07
KS-18D	1.73	0.07
KS-19C	0.60	0.07
KS-19D	1.90	0.07
KS-25C	1.80	0.07
KS-26C	1.48	0.07
KS-26D	1.75	0.07
KS-38C	0.10	0.07
KS-38D	1.05	0.07

7. Discussion

7.1 Updated Observations of the Keystone Fe Skarn Deposit and Characterization of the Magnetite Ore

The location, major ore mineralogy, length, and orientation of the Keystone deposit determined by this study support and refine the findings of Vázquez (1960) and of Fettke (1924) for the “Juncos Deposit”. The Keystone ore is dominantly magnetite and hematite, which is consistent with the deposits described early on in eastern Puerto Rico by Colony and Meyerhoff (1935) and references therein. The existence of “two lenses” as described by Fettke (1924), Vázquez (1960), and Bawiec (1998) could not be verified in this study, but it is possible that only the upper lens was observed because modern vegetation obscures the second lens. It is worth noting that the existence of a second lens has been doubted by others (Jackson, 1934). The occurrences of two main ridges or lens-like bodies were identified in this study on the Cell Tower Hill (Figures 6, 7) but the distance between them is significantly shorter than between the previously reported lenses (Fettke, 1924; Vázquez, 1960). The magnetite is more massive and higher grade on the southern ridge, making it the probable target of historic mining. It is possible the north and south ridges described here were originally one lens that bifurcated over time, from erosion or possibly due to the center of the ore being tunneled during early exploration efforts in 1906-1907 (Fettke, 1924) or during the open pit mining of the 1950s (Vázquez, 1960). Overall, the ore exposed at the surface is extremely weathered, and determining the grade requires further investigation. However, with the new microscopic observations of this study, the Keystone Fe ore can now be summarized as a mixture of magnetite, martite, specular hematite, goethite, and maghemite with varying amounts of fractures, vesicles and vugs.

7.2 Modification and Replacement of Keystone Magnetite

7.2.1 Trace Element and Textural Evidence for Modification of the Keystone Magnetite

Trace element concentrations within skarn magnetite can be modified by processes such as oxy-exsolution, recrystallization, and dissolution and reprecipitation (Hu et al., 2015). The Keystone magnetite does not exhibit lamellae, which are tell-tale textural signs of oxy-exsolution and generally occurs in a closed system under during cooling and/or under oxidizing conditions (Hu et al., 2015; Liao et al., 2023 and references therein). Keystone magnetite also does not display 120° triple junctions, which result from recrystallization in a high-temperature closed system or fluid-assisted open system (Hu et al., 2015 and references therein). The truncations that are observed within the oscillatory zonation (KS-19, KS-26; Figure 16) are commonly found in skarn magnetite and interpreted as indications of dissolution and reprecipitation processes (DRP; Hu et al., 2015; Dare et al., 2015 and references therein). It is worth noting that lattice defects and varying growth rates of the magnetite cannot be ruled out as the cause of truncations in Keystone magnetite.

During DRP, fluids are out of equilibrium with magnetite, which causes magnetite to dissolve at the mineral-fluid interface and reprecipitate (Putnis, 2009; Hu et al., 2014). The presence of truncated zonation indicates that DRP occurred episodically (Hu et al., 2015; Dare et al., 2015 and references therein). The truncated zones likely display similar trace element variations as the non-truncated zones (Figures 15, 16), indicating that the fluid present during the DRP was similar in composition to the fluid that formed the regular oscillatory zonation. The Keystone $\delta^{56}\text{Fe}$ values also reflect evidence of DRP replacement, as indicated by KS-19, and KS-26 having lower $\delta^{56}\text{Fe}$ values (Table 9). This is consistent with the work of Liao et al. (2023), which found that the magnetite that had undergone DRP was isotopically lighter than the

primary magnetite. Within the massive magnetite there are also sections of microporosity. When microporosity is in sharp contact with non-porous magnetite, it can indicate the occurrence of DRP (Putnis, 2002; Hu et al., 2014; Wen et al., 2017). However, due to the heavily fractured nature of the Keystone samples, it is difficult to determine whether this is observed. Therefore, the process of DRP cannot be ruled out as the cause of the microporosity.

7.2.2 Oxidation and Redox-Independent Replacement of Keystone Magnetite

Magnetite can be replaced by hematite by two mechanisms: either due to solid state oxidation or redox-independent DRP reactions (Yin et al., 2022). The resulting mineral is often called martite, which is compositionally the same as hematite but a pseudomorph of magnetite. The diagnostic features of these processes are volumetric changes and the orientation of hematite to the dodecahedral (110) planes of magnetite. During solid state oxidation of magnetite to hematite, Fe^{3+} ion diffusion from Fe_2O_3 within magnetite creates an intermediate phase of maghemite before turning into hematite and results in a slight volume increase. On the other hand, during redox-independent DRP reactions of magnetite to hematite, Fe^{2+} is leached from magnetite and forms an aqueous ferric species from which hematite can then grow (Yin et al., 2022). This causes a volume decrease, which results in porous hematite, especially during pseudomorph replacement (Yin et al., 2022 and references therein). The presence of maghemite (Figure 13D) and the sponge-like texture of martite (Figures 12B, 13C) within Keystone Fe ore indicates that both solid state oxidation and non-redox DRP have occurred, respectively.

In general, Fe^{3+} is correlated with higher $\delta^{56}\text{Fe}$ values while Fe^{2+} is correlated with lower $\delta^{56}\text{Fe}$ values. Thus, magnetite is predicted to have an isotopically lighter $\delta^{56}\text{Fe}$ value compared to hematite that formed under the same conditions (e.g., Dauphas et al., 2017). This is because heavier Fe isotopes tend to form stronger bonds and the oxidation state (Fe^{2+} versus Fe^{3+})

controls the bond strength (Sharp, 2017; Sossi and O'Neill, 2017). Therefore, the $\delta^{56}\text{Fe}$ value of Fe ore comprised of more hematite (or martite) is expected to be higher due to the presence of more Fe^{3+} compared to magnetite. Magnetite that has undergone redox-independent DRP to partially replace it with hematite (i.e., martite), will likewise have a higher $\delta^{56}\text{Fe}$ value due to the initial leaching of Fe^{2+} from the magnetite into the co-existing fluid.

The Keystone $\delta^{56}\text{Fe}$ values display evidence of non-redox DRP replacement, as indicated by KS-15 having both the highest $\delta^{56}\text{Fe}$ values (Table 9) and the highest proportion of martite (50%; Table 5). KS-08 and KS-17 have lower $\delta^{56}\text{Fe}$ values (Table 9) and a lower proportion of martite (5%; Table 5). It is important to note that within a thin section, the distribution of martite is heterogenous, so these estimates should be confirmed through additional petrography throughout the samples.

7.3 The Source of Keystone Magnetite

7.3.1 Trace Element Evidence for the Source of Keystone Magnetite

The variations in trace element concentrations in Keystone magnetite measured via LA-ICP-MS can be used to confirm the deposit type (Figure 19), help identify sources of metals (i.e., magmatic versus hydrothermal; Figures 20, 21), and track fluid changes during mineral precipitation (Dupuis and Beaudoin, 2011; Dare et al., 2014; Nadoll et al., 2014, 2015). Titanium, V, Ca, Al, and Mn concentrations in the Keystone magnetite were plotted on a discrimination diagram following Dupuis and Beaudoin (2011) to compare this skarn to a variety of well-characterized global magnetite-bearing deposits (Figure 19).

The concentrations of trace elements within magnetite can vary in response to numerous factors during formation (e.g., temperature, pressure, fluid, and melt composition; Dare et al., 2014). The behavior of trace elements in magnetite have been the focus of numerous studies

(e.g., Dupuis & Beaudoin, 2011, Dare et al., 2014; Nadoll et al., 2014; Knipping et al., 2015; Nadoll et al., 2015; Duran et al., 2020) and new trends of trace element relationships are still being discovered (e.g., Hu et al., 2022, 2023). In general, magnetite that crystallizes from a magma is depleted in incompatible elements such as Si and Ca and enriched in Ti and Al (Dare et al., 2014; Nadoll et al., 2014). Magmatic-hydrothermal magnetite is enriched in Ni, V, Co, Zn, Mn, and Sn (Dare et al., 2014), whereas hydrothermal magnetite is depleted in immobile elements such as Ti (<2 wt%) and Al (<1 wt%) (Dare et al., 2014 and references therein; Nadoll et al., 2014).

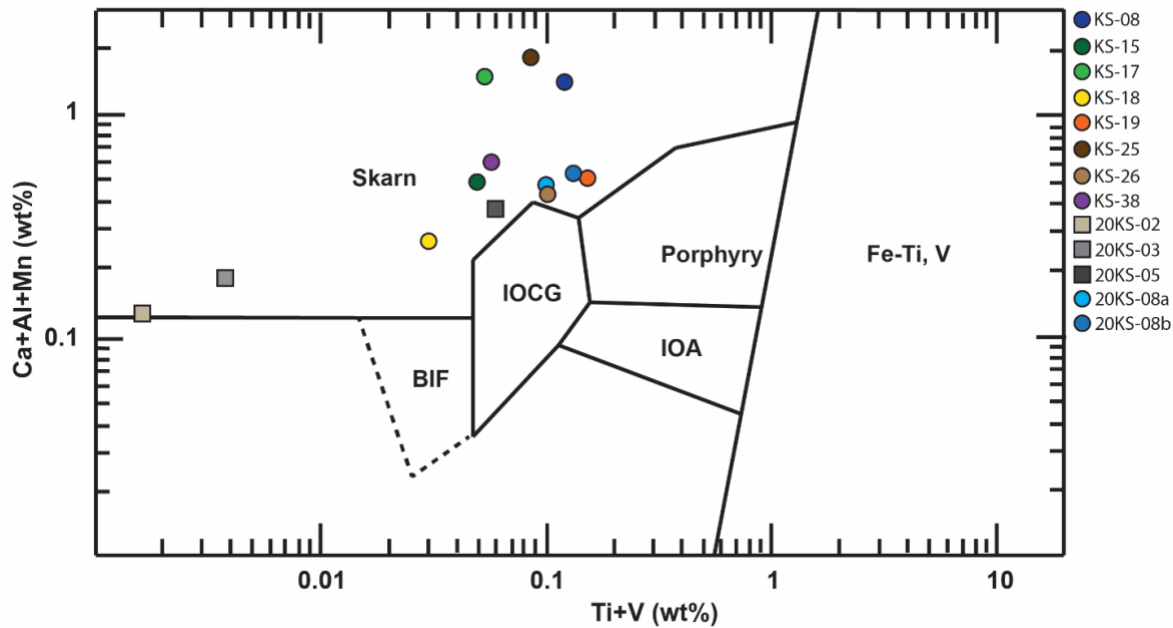


Figure 19: Plot of Ti+V (wt%) vs. Ca+Al+Mn (wt%) measured in Keystone magnetite via LA-ICP-MS. Keystone plots within the skarn field compared to other Fe oxide deposit types (banded iron formation, BIF; iron oxide copper-gold, IOCG; Kiruna/iron oxide-apatite, IOA; porphyry; Fe-Ti-V deposits). Circles represent spatially constrained samples; squares represent spatially unconstrained samples from 2020 field work (after Dupuis and Beaudoin, 2011).

The trace element composition of Keystone magnetite is consistent overall with what is expected from a typical skarn, with both low-temperature (low-T, e.g., meteoric) and high-temperature (high-T, e.g., magmatic or magmatic-hydrothermal) fluid sources. The average trace

element composition of Keystone magnetite is enriched in Ca, Si, and Al relative to all other trace elements including Ti and V (Table 8). Although Al is relatively enriched, it still falls within the hydrothermal range reported by Dare et al. (2014). The high concentrations of Si and Ca and the low concentrations of Ti and V (Figure 20) correspond with magnetite forming from hydrothermal sources rather than from direct crystallization from a magma.

Spatially unconstrained samples 20KS-02 and 20KS-03 have significantly lower Ti+V and Ca+Al+Mn, indicating that lower-T, non-magmatic source fluids were dominant in those locations. This is consistent with petrographic observations of specular hematite enclosed by silicates (mainly quartz) as the dominant ore mineralogy of 20KS-02 and 20KS-03. However, although these two samples were certainly collected from the Cell Tower Hill of Keystone, their exact locations are unknown, so it is not possible to put this interpretation into a deposit-scale context and they are treated as outliers.

Overall, Keystone magnetite has a trace element composition in line with a typical skarn deposit. The source fluids evolved during the growth of the magnetite, as indicated by changes in the concentrations of Al, Si, and Fe content within and across grains of a given sample (Table 6, Figure 17). The broader deposit-scale patterns of trace element concentrations are discussed in detail in Discussion section 7.6.

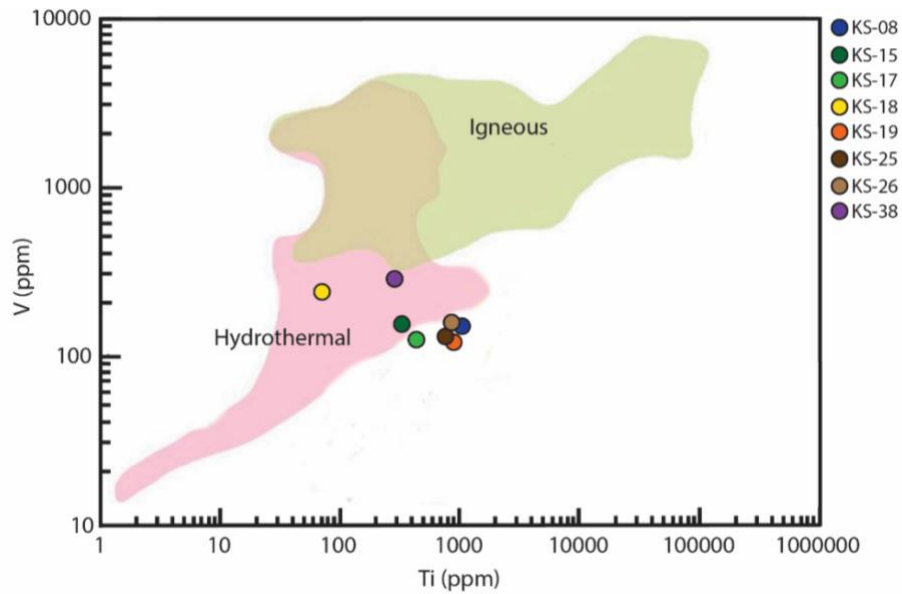


Figure 20: Plot of V (ppm) vs. Ti (ppm) in the Keystone magnetite. Keystone plots within and around the hydrothermal region rather than the igneous region (after Knipping et al., 2015 and Hu et al., 2023).

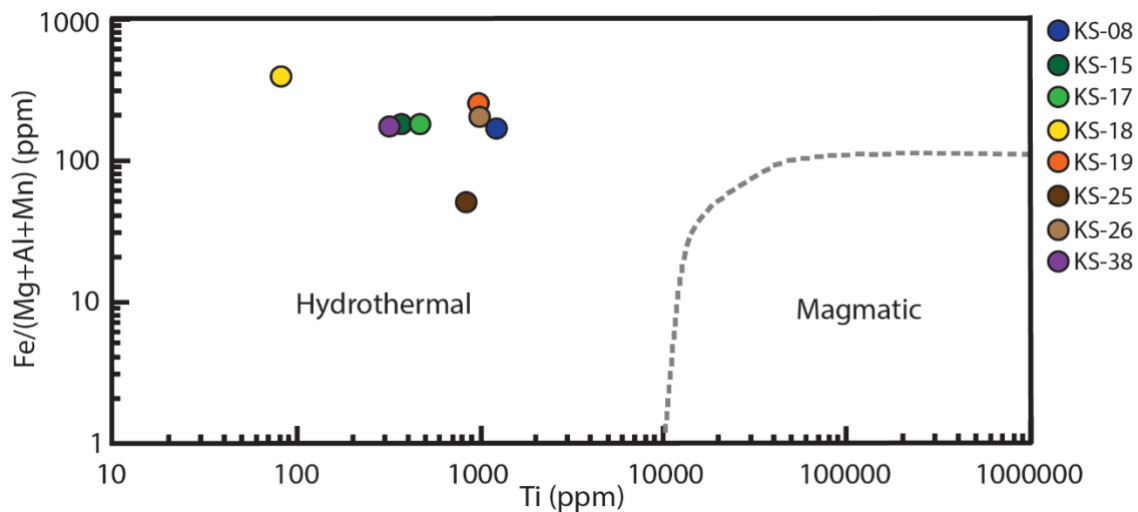


Figure 21: Plot of Fe/(Mg+Al+Mn) (ppm) vs. Ti (ppm) in the Keystone magnetite. All Keystone samples plot within the hydrothermal region (after Hu et al., 2023).

7.3.2 Stable Fe and O Evidence for the Source of Keystone Magnetite

Iron and O stable isotope ratios measured in ore magnetite have been used to identify the source of fluid(s) that formed Fe oxide deposits and the processes that transported the Fe (e.g., Simon et al., 2018 and Troll et al., 2019 and references therein). Lower Fe and O isotope ratios

generally correspond to a non-magmatic/low-T source of fluid (i.e., meteoric) whereas relatively isotopically heavy Fe and O ratios correspond to a magmatic/high-T fluid source (i.e., crystallized from a silicate melt or precipitated from a magmatic-hydrothermal fluid; Bilenker et al., 2016 and references therein).

The method of pairing Fe and O isotopes of magnetite is based on the approach of Hedenquist and Lowenstern (1994) with O and H isotopes in minerals, rocks, and crustal fluids. It can be used to identify fluid source (e.g., non-magmatic/low-T origin and magmatic/high-T origin), multiple fluid generations, and alteration. The Fe and O isotope framework that has been applied to magnetite ore (Figure 22) is based on reported Fe-oxide deposits including banded iron formations (BIF), iron oxide-copper-gold deposits (IOCG), iron oxide-apatite deposits (IOA), porphyry deposits, layered mafic intrusions and skarns (e.g., Bilenker et al., 2016 and references therein; Simon et al., 2019 and references therein; Troll et al., 2019 and references therein).

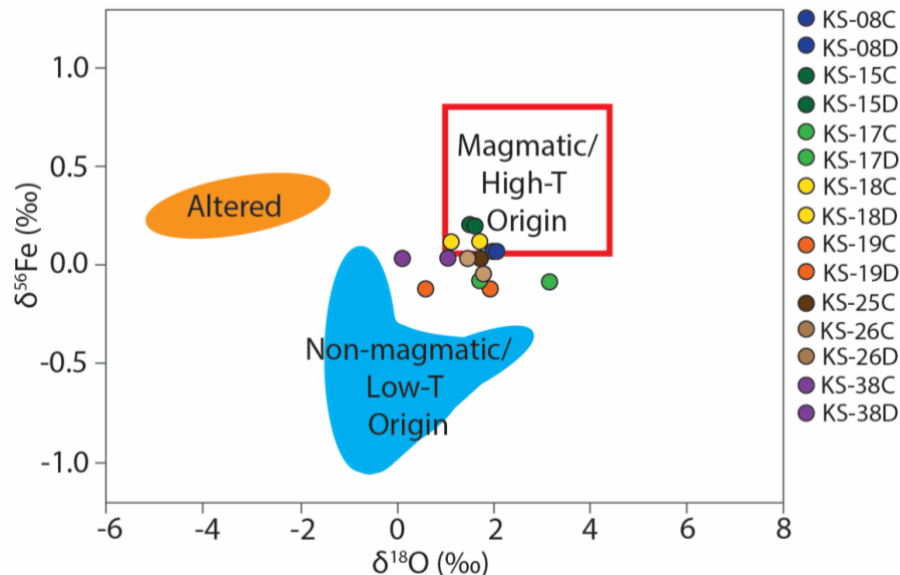


Figure 22: Discrimination diagram of $\delta^{56}\text{Fe}$ vs. $\delta^{18}\text{O}$ to determine the fluid source(s) of Keystone magnetite. The C and D at the ends of sample names refer to analytical duplicates of $\delta^{18}\text{O}$ values of magnetite ore, when available. Errors (2σ) for $\delta^{56}\text{Fe}$ averaged 0.03‰ (Table 9) and 0.07‰ for $\delta^{18}\text{O}$. Altered, Non-magmatic/Low-Temperature (T), and Magmatic/High-T areas are based on reported $\delta^{56}\text{Fe}$ and $\delta^{18}\text{O}$ values of magnetite from Fe-oxide deposits around the world. The magmatic range is based on reports from Taylor (1968), Bindeman (2008), Heimann et al. (2008), and Bilenker et al. (2016) (after Simon et al., 2018).

The Fe isotope composition of Keystone magnetite falls both within and below the magmatic/high-T range ($\delta^{56}\text{Fe} = 0.06\text{‰}$ to 0.86‰ ; Bilenker et al., 2016 and references therein), indicating both magmatic/high-T (KS-15, KS-18, KS-26) and non-magmatic formation/low-T (KS-08, KS-17, KS-19, KS-25, KS-38) fluid sources (Figures 22, 23B). Samples on the Cell Tower Hill, located closest to the zone of alteration, have non-magmatic/low-T isotopic compositions except for KS-08. The O isotope compositions of Keystone magnetite are generally within the magmatic/high-T range ($\delta^{18}\text{O} = 1.0\text{‰}$ to 4.4‰ ; Bilenker et al., 2016 and references therein), apart from two samples with lower $\delta^{18}\text{O}$ values (KS-19C, KS-38C), which are consistent with a non-magmatic/low-T origin (Figures 22, 23C). Sample KS-19 was taken by ore with pockets filled with quartz, perhaps explaining why one data point is within the non-magmatic/low-T range for O isotopes.

In general, the bulk $\delta^{18}\text{O}$ composition of magnetite can be easily altered after deposition by meteoric water at low temperatures while $\delta^{56}\text{Fe}$ is less likely to be altered because meteoric water contains high concentrations of O and low concentrations of Fe (Weis, 2013 and references therein). Since Keystone magnetite samples were pretreated before O isotope analysis, the O isotope data reported here reflect the composition of primary source fluids (see Methods section for details). The Fe and O compositions of Keystone magnetite lie within the magmatic/high-T range and near the non-magmatic/low-T zone, indicating that fluids from more than one source formed and/or altered this deposit.

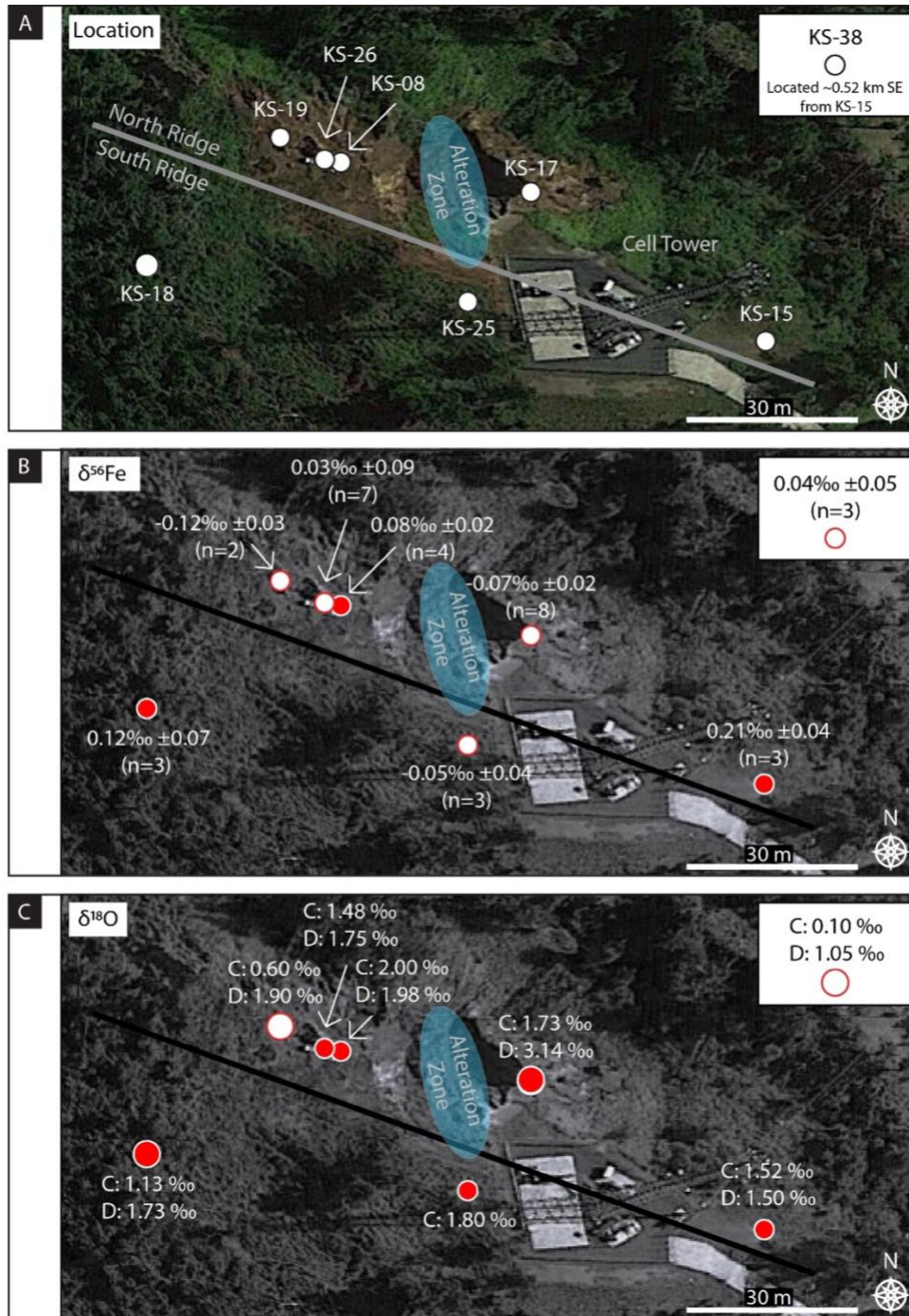


Figure 23: Spatial relationships and average $\delta^{56}\text{Fe}$ and $\delta^{18}\text{O}$ values of the spatially constrained ore samples from 2022 field work. (A) Reference map of the locations of Keystone Fe ore samples analyzed for their trace element geochemistry and Fe and O isotope ratios along the Cell Tower Hill. Inset in the upper right represents KS-38, collected on the East Hill. (B) Average $\delta^{56}\text{Fe}$ values of magnetite ore. Red circles indicate samples within the magmatic/high-T range based on Bilenker et al. (2016) and white circles indicate compositions that are in the non-magmatic/low-T range. (C) The $\delta^{18}\text{O}$ values of magnetite ore, where C and D refer to analytical duplicates, when available. Red circles indicate samples that are in the magmatic/high-T range based on Taylor (1968) and white circles indicate that one data point is within the non-magmatic/low-T range. Larger circles indicate that the difference between the $\delta^{18}\text{O}$ values measured for each duplicate is greater than 0.5‰.

7.4 Keystone Stable Isotope Geochemistry Compared to Global Fe Skarn Data

Only a handful of studies on Fe skarn deposits report magnetite Fe or O isotope data and only two studies report Fe and O pairs (Dannemora, Sweden, Troll et al., 2019; Tibes, Puerto Rico, Barefoot, 2021). The range in Fe isotope compositions of Keystone magnetite is in line with the data available in the literature for other Fe (and Fe-polymetallic or Cu-S-Fe-Au) skarns (Figure 24; Wang et al., 2011; Troll et al., 2019; Zhu et al., 2020; Barefoot, 2021). Most of the skarn deposits reported in the published global magnetite $\delta^{56}\text{Fe}$ dataset (Xinqiao, Dannemora, Han-Xing) lie within or below the magmatic range that was established by Bilenker et al. (2017) after Heimann et al. (2008). Compared to unpublished Fe isotope data of magnetite from one other Puerto Rican skarn (Tibes, Barefoot, 2021), average Keystone magnetite is isotopically lighter (Figure 24). Tibes magnetite $\delta^{56}\text{Fe}$ values (n=18) are consistent only with a magmatic fluid source, but Keystone magnetite $\delta^{56}\text{Fe}$ values (n=10) indicate fluids sources from both magmatic and meteoric sources.

The range in O isotope compositions of Keystone magnetite is in line with the data available in the literature for other Fe (and Fe-Cu or Fe-polymetallic) skarns (Figure 25; Oyman, 2010; Xie et al., 2017; Troll et al., 2019; Dong et al., 2021). Most of the skarn deposits reported in the published global magnetite $\delta^{18}\text{O}$ dataset (Dannemora, Ayazmant, Akesayi, Zhangmantun) lie within or below the magmatic range that was established by Taylor (1968) from measurements of natural igneous magnetite. Compared to unpublished O isotope data of magnetite from the two other Puerto Rican skarns (Tibes and Island Queen, Barefoot, 2021), Keystone magnetite is isotopically lighter than Tibes but isotopically heavier than Island Queen (Figure 25). Tibes magnetite $\delta^{18}\text{O}$ values (n=15) are consistent only with a magmatic fluid source and all measured Island Queen magnetite (n=4) indicate non-magmatic fluid source(s).

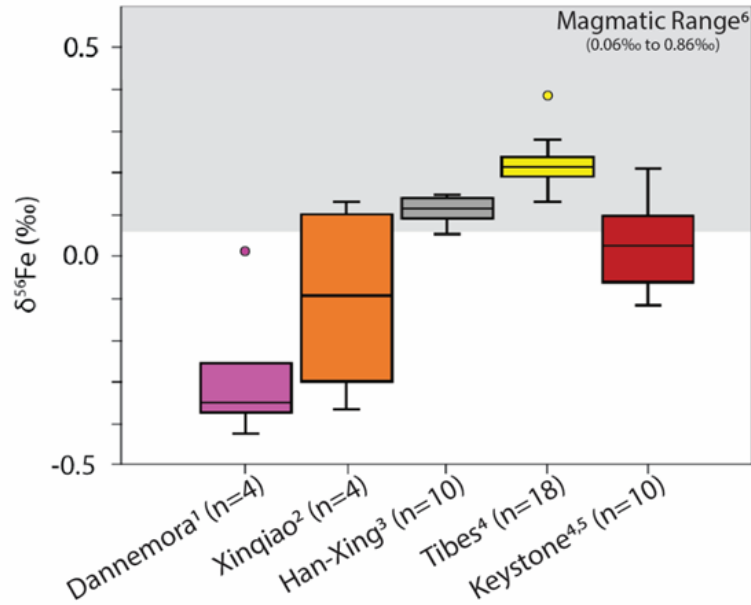


Figure 24: $\delta^{56}\text{Fe}$ values of Keystone magnetite (red) compared to five global Fe-associated skarns: Dannemora in Sweden; (¹Troll et al., 2019), Xinqiao in China (²Wang et al., 2011), Han-Xing in China (³Zhu et al., 2020) Tibes in Puerto Rico (⁴Barefoot, 2021), and Keystone in Puerto Rico (⁵this study; ⁴Barefoot, 2021). All deposits are Fe skarns, but Dannemora and Xinqiao, which are Fe-polymetallic and Cu-S-Fe-Au skarns, respectively. Grey area denotes the range of $\delta^{56}\text{Fe}$ for magmatic magnetite, as modified by ⁶Bilenker et al. (2016).

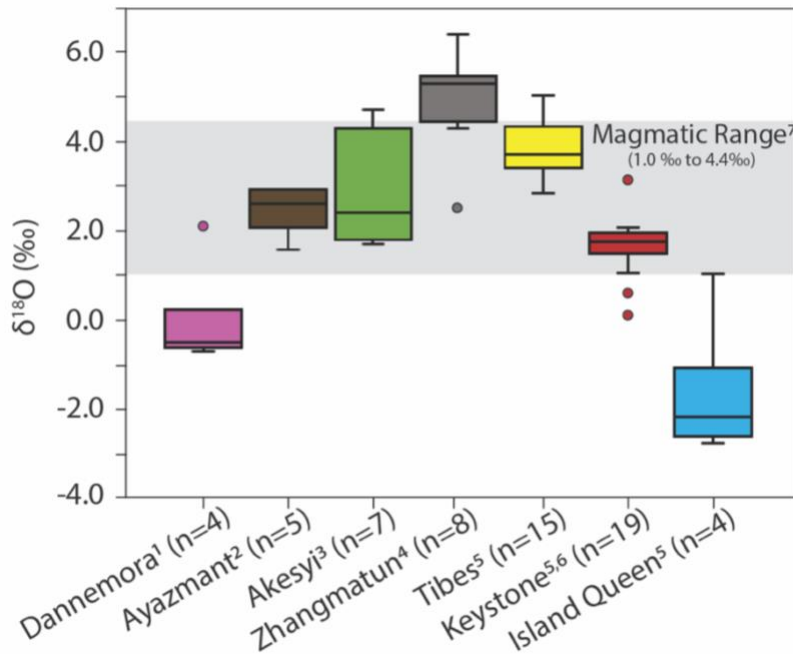


Figure 25: $\delta^{18}\text{O}$ values of Keystone magnetite (red) compared to six global Fe-associated skarns: Dannemora in Sweden (¹Troll et al., 2019), Ayazmant in China (²Oyman, 2010), Akesayi in China (³Dong et al., 2021), Zhangmatun in China (⁴Xie et al., 2017), Tibes in Puerto Rico (⁵Barefoot, 2021), Keystone in Puerto Rico (⁶this study; ⁵Barefoot, 2021), and Island Queen in Puerto Rico (⁵Barefoot, 2021). All deposits are Fe skarns except for Dannemore and Ayazmant which are Fe-polymetallic and Fe-Cu, respectively. The magmatic range (1.0‰ to 4.4‰) established by ⁷Taylor (1968) is indicated by the grey box.

The Keystone skarn is unique compared to the global O isotope dataset in that samples display a range in O isotope compositions that extend from igneous $\delta^{18}\text{O}$ values (magmatic or magmatic-hydrothermal) to non-igneous values (Figure 25). This pattern is observed for Fe isotopes, too (Figure 24). The range may indicate multiple generations of fluids, recording the initial magmatic signatures and then late-stage isotopically lighter signatures. From the published data, only magnetite from the Dannemora Fe-polymetallic skarn sits fully in the non-magmatic field (n=3), except for one geochemical anomaly (Troll et al., 2019). Island Queen magnetite data are also only consistent with non-magmatic fluid sources, but this unpublished dataset is small (n=4) and requires additional field, petrographic, and geochemical investigation to interpret its O isotope signature.

Although the global magnetite Fe and O isotope database is small, one would expect to see a difference in isotopic values between accreted and unaccreted Fe skarns since most Fe skarns form on island arcs that are now accreted onto continents. During the accretion process, skarns undergo metamorphism and associated alteration that would likely change the isotopic composition of their minerals such as magnetite. The Fe and O isotope compositions of magnetite from the unaccreted Fe skarns in Puerto Rico (Keystone, Tibes, Island Queen) extend from igneous values to non-igneous values, detailing the lack of significant isotopic differences between unaccreted and accreted Fe skarns.

7.5 Keystone Skarn Geology and Geochemistry Compared to Puerto Rican Fe Skarns: Tibes and Island Queen

The three Fe skarns in Puerto Rico have both similarities and differences in their geology and geochemistry. First, the Fe and O isotope ratios of Tibes magnetite fall solely within the magmatic range but Keystone and Island Queen magnetite do not. One potential reason for this is

that Tibes is associated with a small igneous stock that is accessible within meters of the ore bodies (Barefoot, 2021; Giovannetti-Nazario, 2022) while Keystone and Island Queen are associated with a much larger igneous body, the San Lorenzo batholith, and formed farther from their source intrusion. Therefore, the fluids that formed Keystone and Island Queen would have traveled a greater distance, allowing for more fluid rock interactions. This distance also potentially allowed for more meteoric input than at Tibes, and the size of the source intrusion provided late-stage Si-Ca-Al rich fluids, causing lighter isotopic signatures and more extensive alteration of the magnetite ore. The differences in the respective source intrusions are also a potential reason that Tibes contains higher grade ore than Keystone. The mineralogy of Tibes ore includes a higher percentage of magnetite ($\geq 80\%$; Barefoot, 2021) with a lack of martite and minimal hematite, indicating that Tibes did not undergo the same amount of alteration as Keystone.

Another major geological difference between the Tibes and Keystone systems, is that Tibes is hosted in limestone and calc-silicate rocks while Keystone is hosted in volcanoclastics. Thus, the elemental budget for reactions between the fluids and host rocks in each system will be different. This may explain why Tibes and Keystone do not contain many of the same secondary minerals except for garnet and pyrite (Barefoot, 2021). Similarly, though, the garnet found at both localities is optically birefringent with oscillatory zoning (Giovannetti-Nazario, 2022). The garnet zonation may be caused by compositional changes in the hydrothermal fluids (Giovannetti-Nazario, 2022 and references therein), which also likely caused the Si-rich zonation seen in both Tibes and Keystone magnetite.

Overall, continuing extensive research on each Fe skarn deposit of Puerto Rico will help determine how source intrusion size, intrusion distance, and host rock composition affect the characteristics of skarn deposits, their ore grade, and geochemical signatures.

7.6 The Formation Model of the Keystone Fe Skarn

The formation of the Keystone skarn can be divided into three main stages: 1) intrusion of an Fe-rich pluton 2) magmatic-hydrothermal fluid release and metal deposition and 3) introduction of late Si-Al-Ca-rich fluids and meteoric water. These stages are based on the spatial relationships, petrography trace element concentrations, and Fe and O isotope ratios of the spatially constrained Keystone Fe ore samples.

7.6.1 Stage 1: Intrusion of Fe-rich Pluton

Volcaniclastic rocks were intruded by an Fe-rich pluton around 69 Ma during the formation of the Antilles (Jolly et al., 1998; Schellekens, 1998; Meinert et al., 2005). The magmatic source of Keystone ore is assumed to be the San Lorenzo batholith (Figure 2; e.g., Vázquez, 1960; Bawiec, 1998) but additional field work needs to be done to consider previously unmapped intrusions (e.g., 375m southeast of Keystone; Figures 6, 10). When the pluton heated surrounding host rocks, garnet began to form.

7.6.2 Stage 2: Magmatic-Hydrothermal Fluid Release and Metal Deposition

As the pluton cooled, magmatic-hydrothermal Fe-bearing fluids were episodically released (Figure 26). The evidence for this is the primarily magmatic/high-T Fe and O isotope compositions of the Fe ore (Figures 22, 24, 25) and the zoned garnets (Figure 18B; Giovannetti-Nazario, 2022 and references therein). The fluid pathways were likely controlled by the local lithology based on the lenticular shape of the deposit.

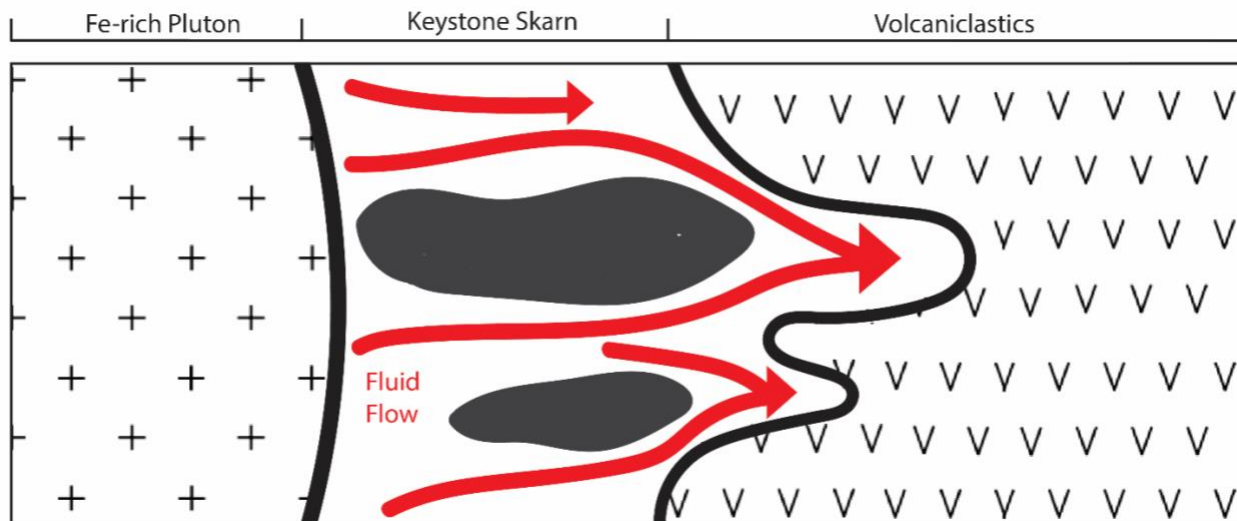


Figure 26: Schematic illustration of magmatic-hydrothermal fluid flow from the Fe-rich pluton interacting with the volcaniclastic host rocks to form the magnetite ore bodies within the Keystone skarn (after Barefoot, 2021).

The magmatic-hydrothermal fluids first precipitated massive magnetite that was enriched in Si and Al (Figure 27A). As the massive magnetite precipitated, the concentrations of Fe, Si and Al in the fluid fluctuated, producing zonation that mirrors the crystal habit (Figure 27B). The fluctuations could have been caused by additional input of magmatic fluids or changes in the fluid composition from interaction with the host rocks. The physicochemical parameters of the fluid also may have changed, such as T and redox (Dare et al., 2014 and references therein). It is possible that micro to nanoscale inclusions produced the zonation, even though they were not observed in this study (Dare et al., 2014 and references therein).

Next, redox dependent (oxidation) and redox-independent processes (DRP) modified the magnetite (Figure 27C, D). Under oxidizing conditions, possibly induced by fluid-host rock reactions or the redox evolution of the source pluton, martite formed by Fe^{3+} ion diffusion along some of the zones (Figure 16E, F), fractures, and within grains. The additional input of magmatic fluids or changes in the fluid composition without oxidation caused episodic DRP within the center or along the edges of zoned magnetite, producing the observed truncations (Figure 16B, D). The occurrence of both martite and truncations within the same sample (e.g., KS-26), and

martite within some of the truncations, indicate that both pathways (Figure 27C, D) can occur.

The order of these processes is unclear with the evidence available so far.

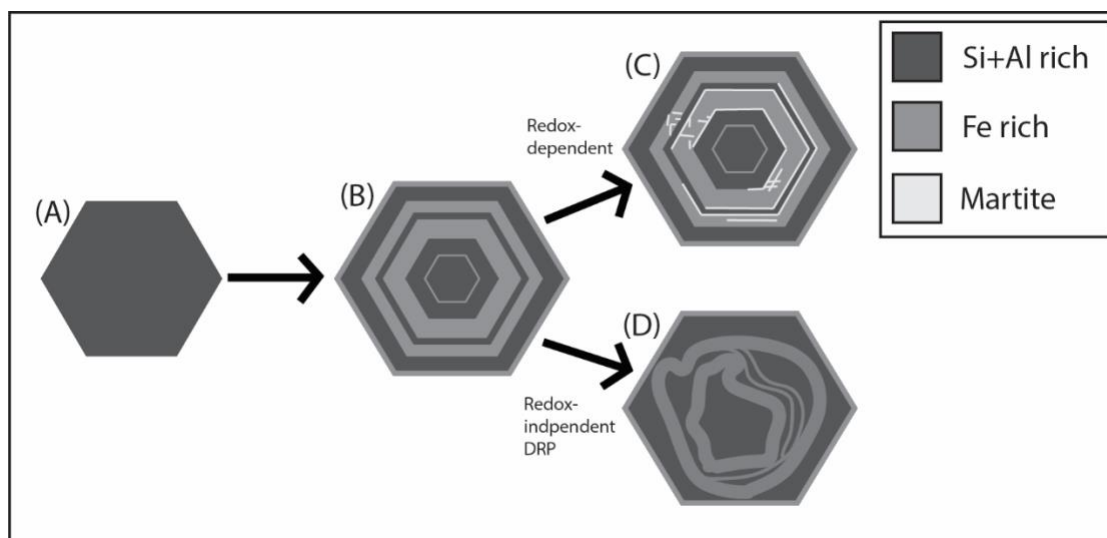


Figure 27: Sketch illustrating the textures that result from modification of Keystone magnetite due to redox-dependent (top, C) and redox-independent (DRP, bottom, D) processes. Dark grey layers are relatively enriched in Si+Al compared to light grey, which is relatively enriched in Fe. (A) Massive magnetite grains enriched in Si+Al. (B) Geochemically zoned magnetite with the same crystal habit (C) Geochemically zoned magnetite under later oxidizing conditions, during which martite formed by ion diffusion along the crystals habit. (D) Redox-independent dissolution-precipitation processes (DRP) form truncated zonation within the grain. Both C and D can happen within the same sample and the order of which came first is unclear (after Hu et al., 2015).

There are at least three generations of ore magnetite, distinguished by their habit and size: massive magnetite (Figure 12A), tabular magnetite (Figure 12D), and smaller individual euhedral magnetite (Figure 12F). The exact relationship between massive and tabular magnetite is unclear because they were not observed within the same sample; the fine-grained euhedral magnetite seems to have formed last. Tabular magnetite likely formed from the same fluids and redox conditions as the massive magnetite because the tabular grains display similar compositional zonation and proportions of martite (Figure 12D).

7.6.3 Stage 3: Late Si-Al-Ca-Rich Fluids and Meteoric Water Input

Lastly, after the Fe ore had been deposited and the system transitioned into a retrograde regime, an oxidized Si-Al-Ca-rich late magmatic-hydrothermal fluids came through the system,

forming the clay minerals of the zone of alteration (Figures 9, 28). The ore that interacted with these fluids (KS-08, KS-17, KS-25) has higher Si, Al, and Ca concentrations (Figures 19, 28B, C). As the Si-Al-Ca-rich fluids came through, meteoric waters may have been introduced as well. These fluids filled vugs, forming goethite and altering portions of magnetite to martite by non-redox DRP reactions.

The proportion of meteoric fluid input was too small to be recorded in the O isotope values indicating the Si-Al-Ca-rich fluids caused the lighter $\delta^{56}\text{Fe}$ values. Thus, the Si-Al-Ca-rich fluids preferentially mobilized and reprecipitated Fe in the form of Fe^{2+} , due to its relative mobility compared to Fe^{3+} and/or Fe^{3+} was remobilized from the magnetite to form specular hematite. This is consistent with the isotopically lighter Fe signature within the ore magnetite near the zone of alteration (KS-17, KS-19, KS-25, KS-26; white circles in Figure 23B). The late-stage fluids formed specular hematite (Figure 14C), and spherical chlorite (Figure 18C) within euhedral quartz.

The euhedral, unfractured nature of the late-stage quartz indicates that the fractures observed in most of the minerals throughout the deposit (e.g., magnetite, garnet, epidote) is likely a result of the episodic release of fluids and volumetric changes associated with martite formation (Putnis, 2009). Overall, the formation of the Keystone skarn is complex, leaving much up for interpretation and more extensive research to be done.

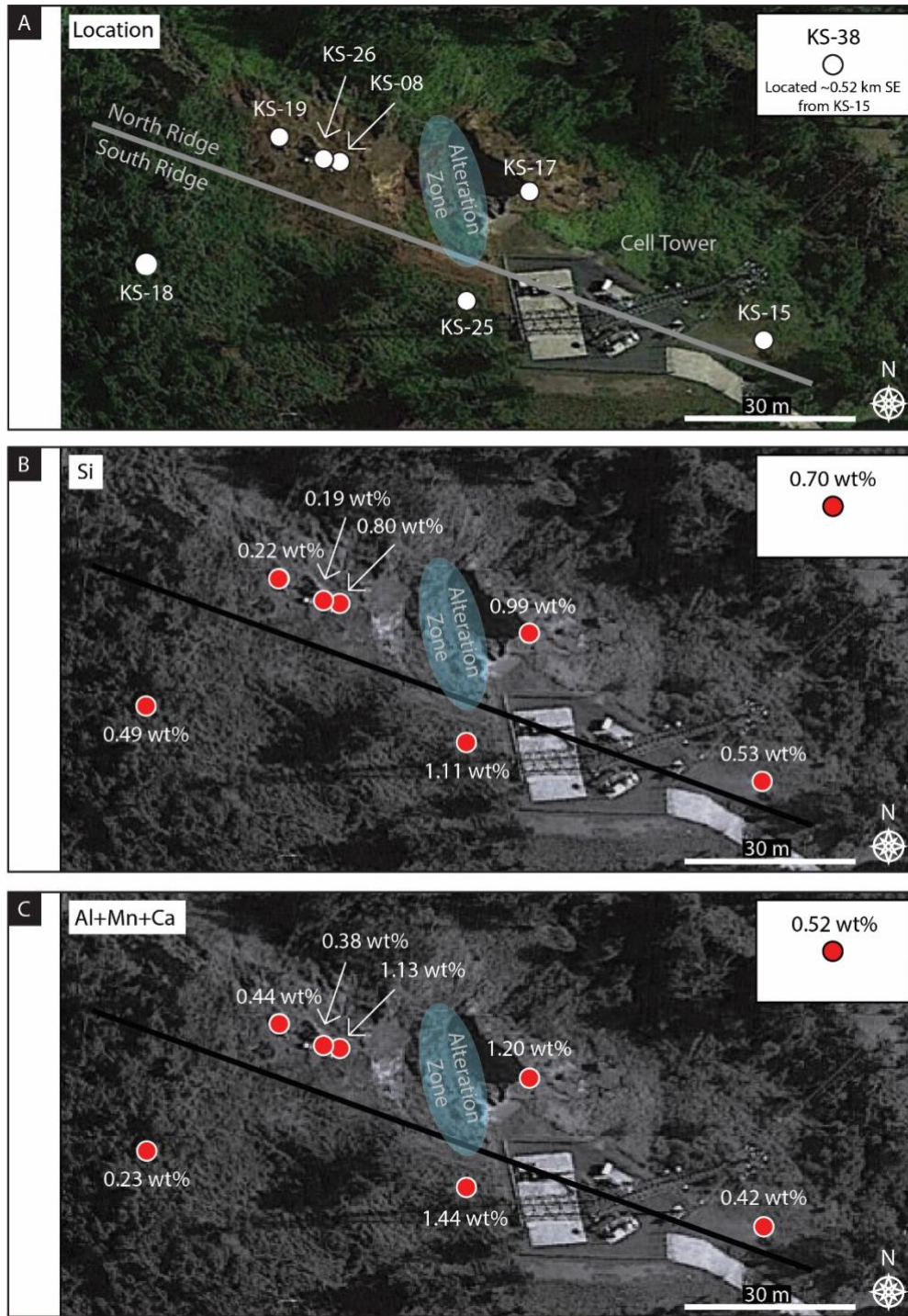


Figure 28: Spatial relationships and trace element results of the spatially constrained ore samples from 2022 field work. (A) Reference map of the locations of Keystone Fe ore samples analyzed for their trace element geochemistry along the Cell Tower Hill. Inset in the upper right represents KS-38, collected on the East Hill. (B) Average Si concentrations in magnetite. (C) Average concentrations of Al+Mn+Ca (wt%) in magnetite as reported in the Ti+V vs. Al+Mn+Ca discrimination plot (Figure 19).

8. Future Work

In this study, the Fe ore of the Keystone skarn was extensively characterized, and for the first time, trace element concentrations and Fe and O isotopic signatures of the Fe ore and fluid sources were determined. However, the examination of the Fe ore is not sufficient to thoroughly describe the entire picture of the Keystone skarn formation or evaluate its economic potential. A better understanding of the geology, mineralogy, and geochemistry of the deposit as a whole is needed for this work to be as useful as possible for the people of Puerto Rico in mineral resource assessment and exploration of other understudied Puerto Rican Fe deposits (e.g., the Humacao deposit; Colony and Meyerhoff, 1935 and references therein; Cadilla, 1963).

To refine and expand the formation model, future work must determine the exact source pluton and the timing associated with the creation of the Keystone skarn. One way to do this is to perform U-Pb geochronology on the Keystone garnets to constrain the age of mineralization. The age of Keystone mineralization could then be compared to the age of the San Lorenzo batholith and the previously unmapped intrusion (Figure 6). The location and extent of the previously unmapped intrusion needs to be determined in detail, the mineralogy must be investigated, and it should be dated. This information will provide the context necessary to fully understand the differences between Tibes, Keystone, and Island Queen and how each formed. It will also allow for improved interpretation of accretion signatures preserved in the trace element and isotopic compositions of Fe skarn magnetite.

Extensive mapping of the Keystone deposit itself is also needed to determine the shape and continuity of the ore body or bodies, evidence of past mining efforts, and a possible genetic connection to Island Queen. An aeromagnetic survey may be the best way to accomplish this task, as the intense vegetation, steep topographical changes, and residential area inhibited sample

collection and mapping efforts. There will also be limitations with aeromagnetic data, and field mapping may be needed to differentiate between the magnetic ore and the magnetic volcanoclastic host rocks, as observed on the East Hill of the deposit. Older maps in the literature have reported a limestone belt (Collores limestone; Fettke, 1924) starting on the East Hill with a similar strike as the Keystone deposit. Carbonate rocks were observed near the East Hill during 2022 field work, but it could not be verified whether they were in place. The lenticular shape of the Keystone deposit and absence of limestone on the Cell Tower Hill could be due to complete replacement of the limestone, although one would expect to see higher concentrations of Ca within the Fe ore. Through extensive mapping of the Keystone deposit and mineralogical investigations of the host rock and zone of alteration, the shape and placement of the ore deposit can be explained.

Improved constraints on the number of episodic events and composition of fluids would help explain the lower quality of the Keystone Fe ore compared to the Tibes skarn. One way to do this is to perform powder XRD on the samples collected from the zone of alteration to better constrain the late-stage fluids that came through the system during Stage 3. Stable O isotope analysis of the late euhedral quartz as well as the alteration may help to determine how much meteoric water, if any, contributed to stages 2 and 3. Another approach would be to analyze the trace element compositions of the Keystone garnets, as Giovannetti-Nazario (2022) did for the Tibes garnets, to better illustrate the chemical changes within the fluids that formed the deposit.

Detailed mapping and characterization of the source pluton, ore, host rock, and alteration can advance our overall understanding of the formation of the Keystone skarn and help us better interpret global geochemical signatures (trace elements, Fe and O isotopes) of Fe skarns.

9. Conclusions

The examination of the Keystone Fe ore through field work, petrography, major and trace element geochemistry, and Fe and O stable isotope analysis detail the complexity of ore formation and reveals the following:

- The Keystone Fe skarn deposit remains accessible as two main ridges on a hill with a cell tower (“Cell Tower Hill”). Additional ore outcrops on another hill to the east (“East Hill”), about 0.52km or less from the ore near the cell tower.
- The Keystone Fe ore is made up of magnetite, martite, specular hematite, goethite, and maghemite, in order of decreasing abundance. The magnetite can be massive, tabular, or euhedral with variable amounts of fractures, vesicles, and vugs.
- Trace element compositions of the Keystone magnetite are consistent with global skarn deposits and indicate a hydrothermal origin rather than crystallization from a magma. The magnetite is enriched in Si, Al, and Ca relative to all other trace elements analyzed.
- The Fe and O isotope signatures of the Keystone magnetite are in line with the small dataset available in literature for other Fe skarns. The $\delta^{56}\text{Fe}$ and $\delta^{18}\text{O}$ values indicate multiple fluid sources of Keystone magnetite but point to initial magmatic-hydrothermal source fluids and only small proportions of meteoric influx in later stages.
- Oscillatory zonation within the Keystone magnetite indicates that the concentrations of Fe, Si, and Al fluctuated during precipitation due to additional fluid input or changes in physicochemical parameters. Truncations of some of the oscillatory zoning within Keystone magnetite indicate dissolution and reprecipitation processes (DRP) due to

additional fluid input, which had a composition different than the fluid that caused the earlier zonation.

- Both redox dependent and independent reactions produced replacement of Keystone magnetite. Martite within the ore was formed as a result of later oxidizing conditions as well as DRP from additional fluid input. The presence of maghemite is evidence that a portion of the magnetite was replaced by martite during solid state oxidation. The presence of porous martite indicates where magnetite was replaced during redox-independent DRP.
- The Keystone Fe skarn formed in three stages: 1) intrusion of an Fe-rich pluton 2) magmatic-hydrothermal fluid release and metal deposition, and 3) introduction of late Si-Al-Ca-rich fluids and meteoric water.
- The Keystone magnetite has higher Si, Al, and Ca concentrations near the zone of alteration, indicating that a late-stage, oxidized Si-Al-Ca-rich magmatic-hydrothermal fluid came through the system (Stage 3).

Additional work needs to be done on the characterization and mapping of the pluton associated with the Keystone skarn, the ore, host rock, and alteration for resource assessment and exploration purposes. Future work should also entail further examination of the Tibes and Island Queen skarns in Puerto Rico to better identify geochemical signatures of unaccreted versus accreted Fe skarns.

References

- Barefoot, M. (2021). Developing a Genetic Model for Puerto Rico's Tibes Iron Deposit through Field Observations and Geochemical Analyses. Master's Thesis, Auburn University.
- Bawiec, W. J. (1998). Geology, geochemistry, geophysics, mineral occurrences, and mineral resource assessment for the commonwealth of Puerto Rico. *U.S. Geological Survey Open-File Report* 98-038.
- Berkey, C. P. (1915) Geological Reconnaissance of Porto Rico. *Annual New York Academy of Sciences Annals*, 26, 1-70.
- Bilenker, L. D., Simon, A. C., Reich, M., Lundstrom, C. C., Gajos, N., Bindeman, I., Barra F., & Munizaga, R. (2016). Fe–O stable isotope pairs elucidate a high-temperature origin of Chilean iron oxide-apatite deposits. *Geochimica et Cosmochimica Acta*, 177, 94-104.
- Bilenker, L. D., VanTongeren, J. A., Lundstrom, C. C., & Simon, A. C. (2017). Iron isotopic evolution during fractional crystallization of the uppermost Bushveld Complex layered mafic intrusion. *Geochemistry, Geophysics, Geosystems*, 18(3), 956-972.
- Bilenker, L. D., Weis, D., Scoates, J. S., & Perry, E. (2018). The application of stable Fe isotopes to magmatic sulfide systems: Constraints on the Fe isotope composition of magmatic pyrrhotite. *Economic Geology*, 113(5), 1181-1192.
- Bindeman, I. (2008). Oxygen isotopes in mantle and crustal magmas as revealed by single crystal analysis. *Reviews in Mineralogy and Geochemistry*, 69, 445–478, <https://doi.org/10.2138/rmg.2008.69.12>.
- Boschman, L. M., van Hinsbergen, D. J., Torsvik, T. H., Spakman, W., & Pindell, J. L. (2014). Kinematic reconstruction of the Caribbean region since the Early Jurassic. *Earth-Science Reviews*, 138, 102-136.
- Cadilla, J. F. (1963). Geology of the Humacao titaniferous iron deposit. *Caribbean Journal of Science*, 3(4), 243-247.
- Colony, R. J., & Meyerhoff, H. A. (1935). The Magnetite deposit near Humacao. Puerto Rico: *American Institute of Mining and Metallurgical Engineers Transactions*, 115, 247-272.
- Craddock, P. R., & Dauphas, N. (2011). Iron isotopic compositions of geological reference materials and chondrites. *Geostandards and Geoanalytical Research*, 35(1), 101-123.
- Dare, S. A., Barnes, S. J., Beaudoin, G., Méric, J., Boutroy, E., & Potvin-Doucet, C. (2014). Trace elements in magnetite as petrogenetic indicators. *Mineralium Deposita*, 49(7), 785-796.
- Dare, S. A., Barnes, S. J., & Beaudoin, G. (2015). Did the massive magnetite “lava flows” of El Laco (Chile) form by magmatic or hydrothermal processes? New constraints from magnetite composition by LA-ICP-MS. *Mineralium Deposita*, 50, 607-617.
- Dauphas, N., John, S. G., & Rouxel, O. (2017). Iron isotope systematics. *Reviews in Mineralogy and Geochemistry*, 82(1), 415-510.

- Dong, R., Wang, H., Li, W., Yan, Q. H., & Zhang, X. (2021). The geology, magnetite geochemistry, and oxygen isotopic composition of the Akesayi skarn iron deposit, Western Kunlun Orogenic Belt, Xinjiang, northwest China: Implications for ore genesis. *Ore Geology Reviews*, 130, 103854, 1-19.
- Dupuis, C. & Beaudoin, G. (2011). Discriminant diagrams for iron oxide trace element fingerprinting of mineral deposit types. *Mineralium Deposita*, 46(4), 319-335.
- Duran, C. J., Barnes, S.-J., Mansur, E. T., Dare, S. A. S., Bédard, L. P., & Sluzhenikin, S. F. (2020). Magnetite Chemistry by Laser Ablation-Inductively Coupled Plasma-Mass Spectrometry Records Sulfide Fractional Crystallization in Massive Nickel-Copper-Platinum Group Element Ores from the Norilsk-Talnakh Mining District (Siberia, Russia): Implications for Trace Element Partitioning into Magnetite. *Economic Geology*, 115, 1245-1266.
<https://doi.org/10.5382/econgeo.4742>
- Einaudi, M. T., Meinert, L. D., & Newberry, R. J. (1981). Skarn deposits. *Economic Geology*, Seventy-Fifth Anniversary Volume, 317-391.
- Fettke, C. R. (1924). Magnetite Deposits of Eastern Porto Rico. *Mining and Metallurgy*, 70, 1024-1038 (Discussions by S.H. Hamilton and A.K. Knickerbocker, 1038-1042).
- Gelabert, P. (2011). Minería en Puerto Rico, 1-15.
- Giovannetti-Nazario, D. A. (2022). Insights into Fe-Skarn mineralization processes through garnet geochemistry and geochronology in Tibes, Puerto Rico. Master's Thesis, University of Puerto Rico, Mayagüez.
- Hedenquist, J. W. & Lowenstern, J. B. (1994). The role of magmas in the formation of hydrothermal ore deposits. *Nature*, 370, 519-527.
- Heimann, A., Beard, B. L., & Johnson, C. M. (2008). The role of volatile exsolution and subsolidus fluid/rock interactions in producing high $^{56}\text{Fe}/^{54}\text{Fe}$ ratios in siliceous igneous rocks. *Geochimica et Cosmochimica Acta*, 72, 4379-4396.
- Howell, D., Griffin, W. L., Pearson, N. J., Powell, W., Wieland, P., & O'Reilly, S. Y. (2013). Trace element partitioning in mixed-habit diamonds. *Chemical Geology*, 355, 134-143.
- Hu, H., Li, J. W., Lentz, D., Ren, Z., Zhao, X. F., Deng, X. D., & Hall, D. (2014). Dissolution–reprecipitation process of magnetite from the Chengchao iron deposit: insights into ore genesis and implication for in-situ chemical analysis of magnetite. *Ore Geology Reviews*, 57, 393-405.
- Hu, H., Lentz, D., Li, J. W., McCarron, T., Zhao, X. F., & Hall, D. (2015). Reequilibration processes in magnetite from iron skarn deposits. *Economic Geology*, 110(1), 1-8.
- Hu, B., Zeng, L. P., Liao, W., Wen, G., Hu, H., Li, M. Y. H., & Zhao, X. F. (2022). The origin and discrimination of High-Ti magnetite in magmatic-hydrothermal systems: Insight from machine learning analysis. *Economic Geology*, 117(7), 1613-1627.

- Hu, X., Xiao, B., Jiang, H., & Huang, J. (2023). Magnetite texture and trace element evolution in the Shaquanzi Fe-Cu deposit, Eastern Tianshan, NW China. *Ore Geology Reviews*, 154, 105306, 1-13.
- Jackson, C. F. (1934). Reconnaissance of mineral deposits in Puerto Rico: typewritten memo. (to the Director, U.S. Bur. Mines), Puerto Rico Econ. Dev. Adm., Dept. Indus. *Research, Mineralogy and Geology Sec. Files*, 6, 655-667.
- Jarosewich, E., Nelen, J. A., and Norberg, J. A. (1980a) Reference Samples for Electron Microprobe Analysis. *Geostandards Newsletter*, 4, 43-47
- Jarosewich, E., Nelen, J. A., and Norberg, J. A. (1980b) Corrections. *Geostandards Newsletter* 4, 257-258
- Jolly, W. T., Lidiak, E. G., Dickin, A. P., & Wu, T. W. (1998). Geochemical diversity of Mesozoic island arc tectonic blocks in eastern Puerto Rico. In *Special Paper of the Geological Society of America*, 322, 67 p.
- Knipping, J. L., Bilenker, L. D., Simon, A. C., Reich, M., Barra F., Deditius, A. P., Wälle, M., Heinrich, C. A., Holtz, F., Munizaga, R. (2015). Trace elements in magnetite from massive iron oxide-apatite deposits indicate a combined formation by igneous and magmatic-hydrothermal processes. *Geochimica et Cosmochimica Acta*, 171, 15-38.
- Knoerr, A. W. (1952). Minnesota Mining Men Open up Rich Puerto Rico Iron Mine. *Journal of Mining Engineering*, 153, 74-9.
- Liao, W., Zhao, X. F., Zeng, L. P., Weyer, S., Zhang, C., Horn, I., & Holtz, F. (2023). Iron isotope fractionation during fluid metasomatism and ore-forming processes in magmatic-hydrothermal systems. *Geochimica et Cosmochimica Acta*, 355, 161-172.
- Lidiak, E. G., & Larue, D. K. (Eds.). (1998). Tectonics and geochemistry of the northeastern Caribbean. In *Special Paper of the Geological Society of America*, 322, V.
- Meinert, L. & Dipple, G. (1992). Skarns and Skarn Deposits. *Geoscience Canada*, 19(4), 145-162.
- Meinert, L. Dipple, G. & Nicolescu, S. (2005). World Skarn Deposits. *Economic Geology*, 100th Anniversary Volume, 299-336.
- Minerals Education Coalition (2022). MEC Mineral Baby 2022 ([Mineralseducationcoalition.org/mining-minerals-information/mining-mineral-statistics/mec-mineral-baby-2022/](https://mineralseducationcoalition.org/mining-minerals-information/mining-mineral-statistics/mec-mineral-baby-2022/)).
- Nadoll, P., Angerer, T., Mauk, J. L., French, D., & Walshe, J. (2014). The chemistry of hydrothermal magnetite: A review. *Ore Geology Reviews*, 61, 1-32.
- Nadoll, P., Mauk, J. L., Leveille, R. A., & Koenig, A. E. (2015). Geochemistry of magnetite from porphyry Cu and skarn deposits in the southwestern United States. *Mineralium Deposita*, 50, 493-515.

National Institute of Standards and Technology (2012a). Certificate of Analysis, Standard Reference Material 610, Trace Elements in Glass.

National Institute of Standards and Technology (2012b). Certificate of Analysis, Standard Reference Material 612, Trace Elements in Glass.

Oyman, T. (2010). Geochemistry, mineralogy and genesis of the Ayazmant Fe–Cu skarn deposit in Ayvalik, (Balikesir), Turkey. *Ore Geology Reviews*, 37, 175-201.

Paton, C., Hellstrom, J., Paul, B., Woodhead, J., and Hergt, J. (2011) Iolite: Freeware for the visualisation and processing of mass spectrometric data. *Journal of Analytical Atomic Spectrometry*, doi:10.1039/c1ja10172b.

Putnis, A. (2002). Mineral replacement reactions: from macroscopic observations to microscopic mechanisms. *Mineralogical Magazine*, 66(5), 689-708.

Putnis, A. (2009). Mineral replacement reactions. *Reviews in Mineralogy and Geochemistry*, 70(1), 87-124.

Robb, L. (2005). Introduction to Ore-Forming Processes. John Wiley & Sons.

Schellekens, J. H. (1998). Geochemical evolution and tectonic history of Puerto Rico. In *Special Paper of the Geological Society of America*, 332, 35-66, <https://doi.org/10.1130/0-8137-2322-1.35>.

Sharp, Z. (2017). Principles of Stable Isotope Geochemistry, 2nd Edition.

Simon, A. C., Knipping, J., Reich, M., Barra, F., Deditius, A. P., Bilenker, L., & Childress, T. (2018). Kiruna-type iron oxide-apatite (IOA) and iron oxide copper-gold (IOCG) deposits form by a combination of igneous and magmatic-hydrothermal processes: evidence from the Chilean Iron Belt. *Economic Geology, Special Publication*, 21, 89-114.

Sossi, P. A. & O'Neill, H. S. C. (2017). The effect of bonding environment on iron isotope fractionation between minerals at high temperature. *Geochimica et Cosmochimica Acta*, 196, 121-143.

Taylor, H. P. (1968). The oxygen isotope geochemistry of igneous rocks. *Contributions to Mineralogy and Petrology*, 19, 1-71, <https://doi.org/10.1007/BF00371729>.

Troll, V. R., Weis, F. A., Jonsson, E., Andersson, U. B., Majidi, S. A., Högdahl, K., Harris, C., Millet, M., Chinnasamy, S. S., Kooijman, E., & Nilsson, K. P. (2019). Global Fe–O isotope correlation reveals magmatic origin of Kiruna-type apatite-iron-oxide ores. *Nature Communications*, 10, 1712, 1-12.

U.S. Geological Survey (2013). Juncos Quadrangle, Puerto Rico. 7.5-minute Map Series.

U.S. Geological Survey (2022a). Mineral Commodity Summaries 2022, Iron Ore.

U.S. Geological Survey (2022b). Reference Material Information Sheet BCR-2g and BCR-2ga (Columbia River Basalt Glass).

Vázquez, L. (1960). *Geology and Ore Deposits of the Keystone Iron Mine Near Juncos, Puerto Rico*. Commonwealth of Puerto Rico, Office of the Governor, Mining Commission. *Second Caribbean Geological Conference*, 143-146.

Wang, Y., Zhu, X. K., Mao, J. W., Li, Z. H., & Cheng, Y. B. (2011). Iron isotope fractionation during skarn-type metallogeny: a case study of Xinqiao Cu–S–Fe–Au deposit in the Middle–Lower Yangtze valley. *Ore Geology Reviews*, 43(1), 194-202.

Wang, S., Hausfather, Z., Davis, S., Lloyd, J., Olson, E. B., Liebermann, L., Núñez-Mujica, G. D., & McBride, J. (2023). Future demand for electricity generation materials under different climate mitigation scenarios. *Joule*, 7, 309-332.

Weis, F. (2013). Oxygen and iron isotope systematics of the Grängesberg mining district (GMD), central Sweden. Master's Thesis, Uppsala University.

Wen, G., Li, J. W., Hofstra, A. H., Koenig, A. E., Lowers, H. A., & Adams, D. (2017). Hydrothermal reequilibration of igneous magnetite in altered granitic plutons and its implications for magnetite classification schemes: Insights from the Handan-Xingtai iron district, North China Craton. *Geochimica et Cosmochimica Acta*, 213, 255-270.

Woodhead, J., Hellstrom, J., Hergt, J., Greig, A. & Maas, R. (2007). Isotopic and elemental imaging of geological materials by laser ablation Inductively Coupled Plasma mass spectrometry. *Journal of Geostandards and Geoanalytical Research*, 31, 331-343.

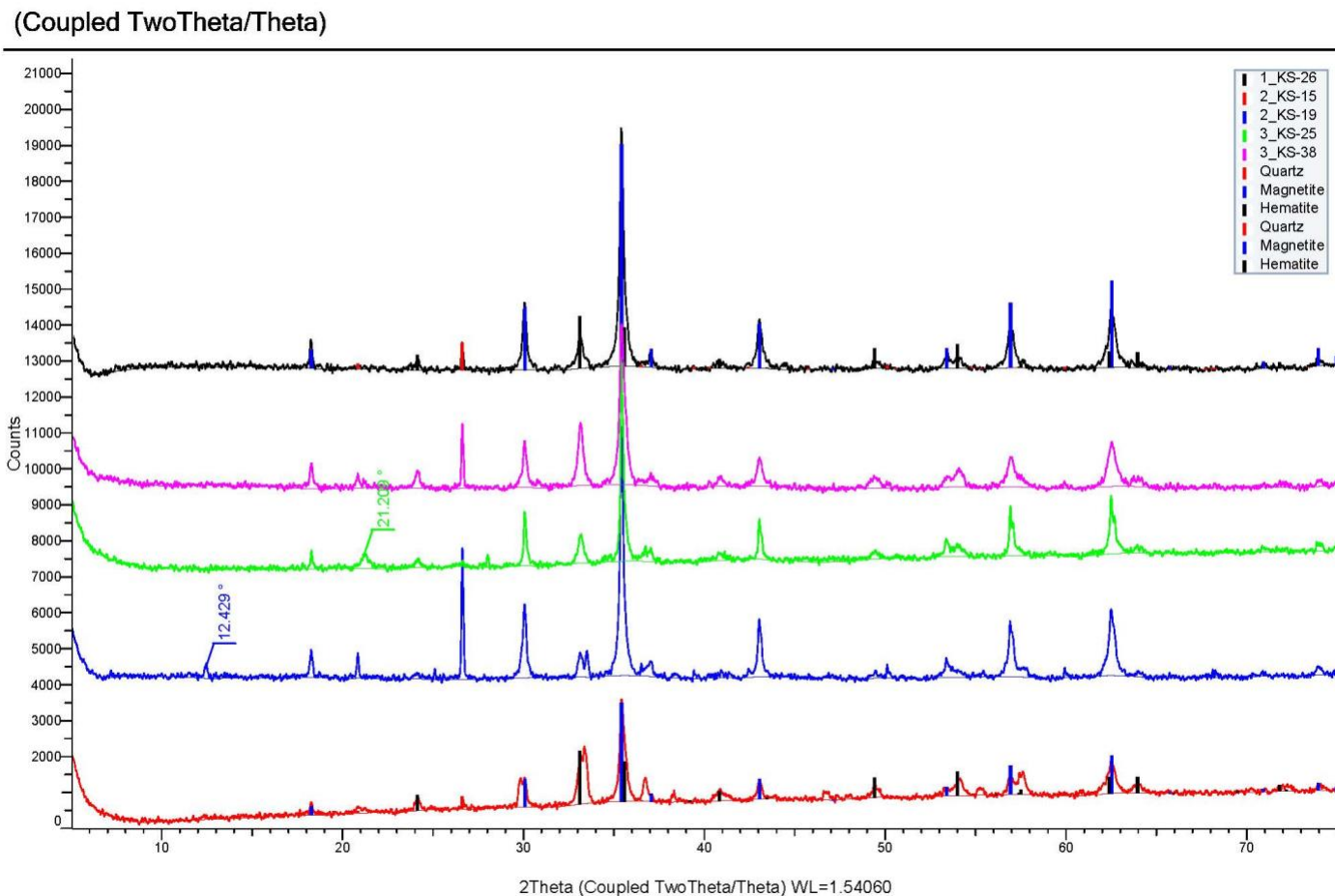
Xie, Q., Zhang, Z., Hou, T., Jin, Z., & Santosh, M. (2017). Geochemistry and oxygen isotope composition of magnetite from the Zhangmatun deposit, North China Craton: Implications for the magmatic-hydrothermal evolution of Cornwall-type iron mineralization. *Ore Geology Reviews*, 88, 57-70.

Yin, S., Wirth, R., He, H., Ma, C., Pan, J., Xing, J., Xu, J., Fu, J., & Zhang, X. N. (2022). Replacement of magnetite by hematite in hydrothermal systems: A refined redox-independent model. *Earth and Planetary Science Letters*, 577, 117-282.

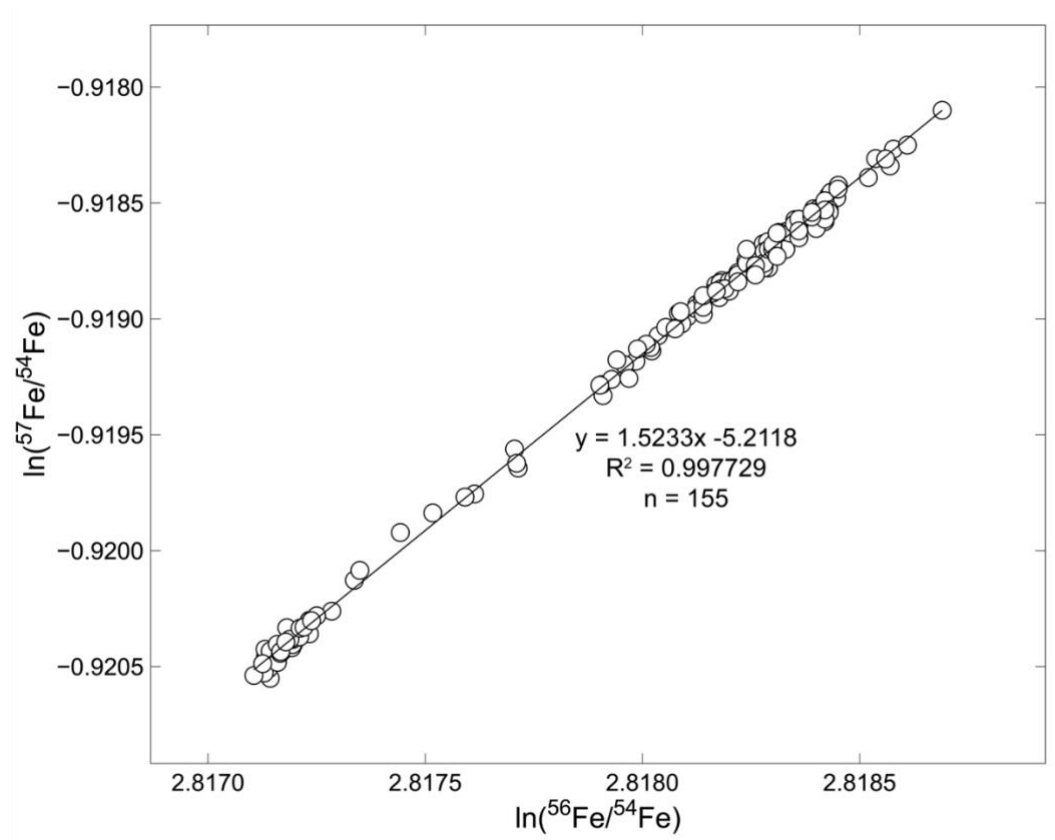
Zhu, B., Zhang, H., Santosh, M., Su, B., Zhang, P., Han, C., & He, Y. (2020). Iron Isotopes Constrain the Metal Sources of Skarn Deposits: A Case Study from the Han-Xing Fe Deposit, China. *Minerals*, 10(11), 951, 1-17.

Appendix A: Supplemental Figures

Supplemental Figure A1. X-Ray Diffraction (XRD) spectra for the analysis of five representative Keystone ore samples. XRD analyses were performed in the Auburn University Department of Geosciences using a Bruker D2 Phaser with a LynxEye detector. The two-theta range was 5.0° to 75.0° with a step size of 0.02. The data were processed using Difrac.Eva version 4.2 and the Crystallography Open Database was used for phase identification. Vertical lines in the spectra represent major peaks for quartz (red), magnetite (blue), and hematite (black).



Supplemental Figure A2. Mass dependent fractionation check for Fe isotope analysis. Each data point represents a single analysis of the standard (IRMM-14), reference material (BCR-2), or Keystone magnetite samples. The slope of the line is consistent with ideal, mass dependent fractionation (~ 1.5 ; Dauphas et al., 2017) and serves as a quality control check for potential instrument or procedural induced mass independent fractionation.



Appendix B: Full Fe and Trace Element Dataset by Electron Microprobe Analysis

Table B1. Elemental (wt%) concentrations in magnetite standard 114887 (USNM 114887) from the Smithsonian National Museum of Natural History measured by EMPA. *Fe (wt%) represents total Fe. Analysis computer optimized to balance FeO and Fe₂O₃. The average value of all measurements and accepted values by Jarosewich et al., (1980a, 1980b) are given at the end the end of the table.

Sample	Mg (wt%)	Al (wt%)	Si (wt%)	Ca (wt%)	Ti (wt%)	Cr (wt%)	Fe* (wt%)	Mn (wt%)	Na (wt%)	V (wt%)	O (wt%)	Total
USNM 114887	0.04	0.00	0.00	0.00	0.07	0.06	71.29	0.02	0.00	0.23	27.47	99.17
USNM 114887	0.06	0.02	0.00	0.03	0.08	0.04	72.85	0.02	0.00	0.26	28.14	101.49
USNM 114887	0.22	0.10	0.01	0.00	0.07	0.02	71.33	0.01	0.00	0.24	27.70	99.70
USNM 114887	0.04	0.01	0.00	0.00	0.06	0.07	73.26	0.01	0.00	0.20	28.23	101.88
USNM 114887	0.05	0.04	0.00	0.00	0.05	0.02	72.60	0.02	0.00	0.24	28.00	101.03
USNM 114887	0.05	0.02	0.00	0.00	0.05	0.00	72.62	0.01	0.07	0.25	28.01	101.08
USNM 114887	0.08	0.01	0.00	0.03	0.07	0.00	69.29	0.01	0.00	0.29	26.77	96.53
USNM 114887	0.02	0.01	0.02	0.01	0.06	0.04	69.50	0.02	0.00	0.30	26.85	96.83
USNM 114887	0.01	0.06	0.00	0.02	0.22	0.02	68.42	0.01	0.00	0.30	26.55	95.60
USNM 114887	0.06	0.01	0.00	0.01	0.06	0.00	70.25	0.01	0.00	0.26	27.09	97.75
USNM 114887	0.03	0.01	0.00	0.03	0.04	0.00	70.45	0.01	0.00	0.26	27.15	97.99
USNM 114887	0.11	0.04	0.05	0.01	0.06	0.05	70.30	0.06	0.03	0.24	27.26	98.20
USNM 114887	0.04	0.01	0.00	0.00	0.04	0.04	70.84	0.04	0.00	0.24	27.30	98.55
USNM 114887	0.01	0.03	0.00	0.00	0.04	0.02	69.92	0.08	0.00	0.19	26.93	97.23
USNM 114887	0.10	0.03	0.00	0.00	0.05	0.03	70.93	0.10	0.05	0.22	27.42	98.92
USNM 114887	0.06	0.03	0.00	0.01	0.04	0.05	70.86	0.04	0.05	0.26	27.38	98.77
USNM 114887	0.06	0.02	0.00	0.00	0.06	0.08	69.04	0.13	0.00	0.28	26.72	96.38
USNM 114887	0.04	0.01	0.00	0.00	0.06	0.03	69.72	0.11	0.06	0.28	26.95	97.27
USNM 114887	0.02	0.05	0.01	0.00	0.06	0.01	71.54	0.08	0.10	0.25	27.65	99.76
USNM 114887	0.07	0.02	0.00	0.00	0.04	0.02	70.45	0.05	0.00	0.27	27.19	98.11
USNM 114887	0.04	0.00	0.06	0.02	0.05	0.06	71.11	0.03	0.00	0.24	27.48	99.08
USNM 114887	0.04	0.03	0.00	0.00	0.06	0.04	70.88	0.10	0.00	0.28	27.39	98.81
USNM 114887	0.02	0.01	0.00	0.01	0.09	0.07	71.98	0.07	0.00	0.26	27.80	100.32
USNM 114887	0.03	0.05	0.00	0.00	0.06	0.05	72.99	0.07	0.00	0.25	28.19	101.69
USNM 114887	0.06	0.00	0.00	0.03	0.12	0.02	70.85	0.08	0.00	0.30	27.41	98.87
USNM 114887	0.04	0.06	0.00	0.02	0.09	0.06	70.79	0.09	0.00	0.27	27.41	98.83
USNM 114887	0.04	0.03	0.00	0.04	0.06	0.13	70.74	0.04	0.11	0.27	27.41	98.88
USNM 114887	0.03	0.04	0.00	0.00	0.08	0.09	70.94	0.05	0.03	0.26	27.43	98.96
USNM 114887	0.04	0.04	0.13	0.00	0.06	0.03	72.11	0.13	0.00	0.30	28.04	100.89

Sample	Mg (wt%)	Al (wt%)	Si (wt%)	Ca (wt%)	Ti (wt%)	Cr (wt%)	Fe* (wt%)	Mn (wt%)	Na (wt%)	V (wt%)	O (wt%)	Total
USNM 114887	0.05	0.02	0.00	0.02	0.05	0.07	71.24	0.06	0.04	0.25	27.53	99.33
USNM 114887	0.02	0.04	0.00	0.00	0.09	0.00	71.15	0.10	0.00	0.26	27.48	99.14
USNM 114887	0.06	0.03	0.00	0.01	0.05	0.02	70.59	0.04	0.12	0.24	27.28	98.44
USNM 114887	0.01	0.05	0.00	0.03	0.04	0.10	71.12	0.07	0.00	0.25	27.48	99.15
USNM 114887	0.05	0.02	0.00	0.02	0.04	0.12	71.38	0.02	0.00	0.26	27.57	99.48
USNM 114887	0.08	0.03	0.00	0.01	0.07	0.00	70.71	0.08	0.01	0.25	27.33	98.57
USNM 114887	0.03	0.01	0.00	0.03	0.04	0.00	71.71	0.07	0.10	0.27	27.68	99.94
USNM 114887	0.06	0.02	0.03	0.02	0.07	0.03	71.13	0.06	0.08	0.29	27.55	99.33
USNM 114887	0.08	0.02	0.00	0.03	0.06	0.02	70.92	0.08	0.02	0.26	27.42	98.91
USNM 114887	0.04	0.05	0.00	0.04	0.04	0.03	69.83	0.06	0.00	0.24	26.98	97.32
USNM 114887	0.03	0.02	0.00	0.00	0.07	0.02	70.82	0.09	0.00	0.25	27.34	98.65
USNM 114887	0.02	0.05	0.01	0.04	0.08	0.00	70.83	0.09	0.04	0.26	27.39	98.80
USNM 114887	0.04	0.04	0.00	0.01	0.06	0.04	70.49	0.08	0.00	0.26	27.23	98.25
USNM 114887	0.00	0.02	0.05	0.02	0.05	0.00	72.14	0.08	0.00	0.25	27.85	100.45
USNM 114887	0.10	0.02	0.00	0.00	0.09	0.05	71.77	0.03	0.00	0.26	27.75	100.07
USNM 114887	0.08	0.04	0.08	0.03	0.05	0.06	70.38	0.08	0.06	0.26	27.34	98.46
USNM 114887	0.03	0.04	0.00	0.01	0.06	0.00	72.26	0.06	0.00	0.29	27.90	100.66
USNM 114887	0.07	0.02	0.00	0.02	0.08	0.02	72.11	0.09	0.09	0.29	27.92	100.71
USNM 114887	0.10	0.02	0.00	0.02	0.08	0.00	71.20	0.03	0.00	0.27	27.52	99.24
USNM 114887	0.17	0.07	0.08	0.01	0.08	0.09	71.49	0.08	0.09	0.32	27.93	100.41
USNM 114887	0.07	0.04	0.03	0.02	0.06	0.04	71.46	0.02	0.07	0.24	27.66	99.71
USNM 114887	0.02	0.02	0.07	0.01	0.09	0.09	71.20	0.07	0.00	0.27	27.62	99.47
USNM 114887	0.04	0.04	0.00	0.03	0.21	0.04	71.35	0.03	0.01	0.28	27.68	99.72
USNM 114887	0.05	0.03	0.00	0.02	0.06	0.04	73.00	0.09	0.00	0.26	28.21	101.78
USNM 114887	0.04	0.02	0.00	0.02	0.05	0.00	72.35	0.11	0.04	0.27	27.94	100.84
USNM 114887	0.06	0.02	0.00	0.02	0.08	0.01	72.11	0.07	0.00	0.28	27.87	100.51
USNM 114887	0.10	0.01	0.00	0.04	0.06	0.04	71.36	0.06	0.00	0.28	27.60	99.55
USNM 114887	0.00	0.02	0.00	0.02	0.05	0.07	70.69	0.11	0.02	0.25	27.29	98.53
USNM 114887	0.05	0.03	0.00	0.02	0.04	0.00	71.01	0.08	0.00	0.24	27.39	98.86

Sample	Mg (wt%)	Al (wt%)	Si (wt%)	Ca (wt%)	Ti (wt%)	Cr (wt%)	Fe* (wt%)	Mn (wt%)	Na (wt%)	V (wt%)	O (wt%)	Total
USNM 114887	0.06	0.02	0.05	0.01	0.06	0.10	71.16	0.05	0.00	0.25	27.56	99.34
USNM 114887	0.04	0.04	0.00	0.00	0.07	0.00	71.54	0.10	0.00	0.29	27.65	99.73
USNM 114887	0.03	0.02	0.00	0.02	0.06	0.04	71.17	0.08	0.00	0.27	27.48	99.16
USNM 114887	0.01	0.02	0.10	0.00	0.31	0.00	70.11	0.06	0.10	0.27	27.35	98.33
USNM 114887	0.01	0.03	0.00	0.00	0.08	0.03	70.96	0.04	0.10	0.23	27.40	98.89
USNM 114887	0.06	0.01	0.00	0.00	0.07	0.00	71.08	0.06	0.00	0.27	27.43	98.98
USNM 114887	0.08	0.03	0.00	0.01	0.07	0.00	71.07	0.05	0.00	0.27	27.46	99.04
USNM 114887	0.04	0.00	0.00	0.00	0.06	0.00	71.00	0.08	0.00	0.27	27.38	98.82
USNM 114887	0.02	0.02	0.00	0.02	0.06	0.23	71.67	0.09	0.01	0.26	27.76	100.14
USNM 114887	0.05	0.06	0.08	0.01	0.09	0.06	71.09	0.09	0.00	0.26	27.60	99.37
USNM 114887	0.01	0.04	0.00	0.00	0.06	0.03	71.78	0.05	0.05	0.24	27.70	99.97
USNM 114887	0.11	0.02	0.07	0.00	0.08	0.00	71.22	0.06	0.04	0.22	27.60	99.42
USNM 114887	0.04	0.00	0.00	0.00	0.05	0.00	71.35	0.11	0.08	0.24	27.53	99.40
USNM 114887	0.04	0.05	0.00	0.00	0.09	0.00	71.38	0.02	0.09	0.25	27.60	99.52
USNM 114887	0.03	0.03	0.00	0.01	0.09	0.05	70.04	0.05	0.00	0.23	27.06	97.60
USNM 114887	0.03	0.03	0.00	0.00	0.06	0.07	71.35	0.11	0.00	0.23	27.56	99.45
USNM 114887	0.05	0.02	0.03	0.00	0.08	0.00	71.39	0.06	0.01	0.25	27.58	99.46
USNM 114887	0.00	0.02	0.00	0.00	0.07	0.05	70.71	0.07	0.00	0.24	27.27	98.43
USNM 114887	0.11	0.05	0.00	0.00	0.03	0.05	71.66	0.08	0.09	0.24	27.73	100.04
USNM 114887	0.06	0.03	0.15	0.00	0.07	0.00	71.86	0.04	0.00	0.21	27.89	100.32
USNM 114887	0.04	0.02	0.00	0.01	0.06	0.00	71.61	0.11	0.00	0.25	27.63	99.74
USNM 114887	0.07	0.04	0.00	0.00	0.04	0.05	72.57	0.04	0.03	0.23	28.02	101.08
USNM 114887	0.06	0.02	0.00	0.00	0.05	0.00	72.13	0.05	0.11	0.21	27.83	100.45
USNM 114887	0.05	0.03	0.00	0.00	0.03	0.05	72.75	0.05	0.03	0.25	28.07	101.30
USNM 114887	0.09	0.03	0.00	0.01	0.04	0.02	72.29	0.08	0.10	0.23	27.94	100.83
USNM 114887	0.08	0.00	0.00	0.00	0.06	0.06	72.38	0.07	0.03	0.22	27.93	100.81
USNM 114887	0.02	0.02	0.00	0.01	0.06	0.07	70.45	0.06	0.00	0.25	27.19	98.12
USNM 114887	0.18	0.07	0.24	0.00	0.05	0.07	71.19	0.05	0.02	0.27	27.90	100.04
USNM 114887	0.03	0.03	0.00	0.01	0.05	0.01	72.56	0.07	0.03	0.28	28.01	101.07

Sample	Mg (wt%)	Al (wt%)	Si (wt%)	Ca (wt%)	Ti (wt%)	Cr (wt%)	Fe* (wt%)	Mn (wt%)	Na (wt%)	V (wt%)	O (wt%)	Total
USNM 114887	0.04	0.05	0.00	0.01	0.07	0.01	71.35	0.04	0.00	0.25	27.56	99.40
USNM 114887	0.02	0.21	0.00	0.04	0.11	0.17	70.85	0.10	0.11	0.06	27.54	99.22
USNM 114887	0.04	0.02	0.00	0.00	0.12	0.00	71.82	0.07	0.06	0.25	27.77	100.16
USNM 114887	0.00	0.00	0.00	0.00	0.07	0.07	71.80	0.10	0.00	0.23	27.68	99.95
USNM 114887	0.04	0.02	0.00	0.00	0.09	0.00	71.57	0.05	0.03	0.24	27.61	99.65
USNM 114887	0.05	0.03	0.00	0.00	0.05	0.09	71.87	0.06	0.03	0.26	27.77	100.21
USNM 114887	0.05	0.05	0.00	0.00	0.06	0.07	70.95	0.05	0.03	0.26	27.43	98.93
USNM 114887	0.03	0.00	0.02	0.00	0.06	0.03	71.95	0.12	0.00	0.29	27.79	100.28
USNM 114887	0.02	0.03	0.00	0.00	0.08	0.06	71.30	0.08	0.00	0.24	27.54	99.36
USNM 114887	0.09	0.05	0.03	0.00	0.07	0.00	71.76	0.05	0.00	0.26	27.77	100.08
USNM 114887	0.02	0.03	0.00	0.01	0.39	0.06	72.17	0.15	0.05	0.33	28.16	101.37
USNM 114887	0.14	0.04	0.12	0.00	0.05	0.00	71.32	0.08	0.00	0.28	27.74	99.77
USNM 114887	0.01	0.02	0.00	0.00	0.07	0.12	72.74	0.03	0.00	0.24	28.07	101.30
USNM 114887	0.04	0.02	0.00	0.00	0.06	0.04	72.52	0.07	0.00	0.30	28.01	101.05
USNM 114887	0.02	0.03	0.00	0.00	0.09	0.06	71.46	0.11	0.00	0.29	27.64	99.69
USNM 114887	0.12	0.05	0.06	0.01	0.05	0.01	70.86	0.07	0.00	0.27	27.49	98.99
USNM 114887	0.05	0.02	0.00	0.01	0.08	0.00	71.13	0.03	0.03	0.27	27.47	99.09
USNM 114887	0.08	0.08	0.00	0.02	0.04	0.05	71.25	0.09	0.00	0.25	27.58	99.44
USNM 114887	0.09	0.04	0.00	0.00	0.06	0.05	70.76	0.05	0.00	0.23	27.35	98.63
USNM 114887	0.04	0.03	0.00	0.01	0.06	0.03	71.90	0.14	0.00	0.24	27.77	100.23
USNM 114887	0.05	0.01	0.00	0.00	0.06	0.07	71.46	0.01	0.00	0.23	27.56	99.44
USNM 114887	0.04	0.03	0.00	0.00	0.05	0.02	71.96	0.10	0.00	0.21	27.74	100.14
USNM 114887	0.16	0.05	0.15	0.00	0.06	0.06	71.10	0.09	0.00	0.21	27.71	99.58
Average	0.05	0.03	0.02	0.01	0.07	0.04	71.30	0.06	0.02	0.25	27.57	99.43
Accepted	0.03	-	-	-	0.1	0.17	70.69	<0.01	-	-	27.17	98.16

Table B2. Elemental (wt%) concentrations in Keystone Fe ore measured by EMPA. The numbers in parentheses represent the spot analysis number. *Fe (wt%) represents total Fe. Software optimized to balance FeO and Fe₂O₃.

Sample	Mg (wt%)	Al (wt%)	Si (wt%)	Ca (wt%)	Ti (wt%)	Cr (wt%)	Fe* (wt%)	Mn (wt%)	Na (wt%)	V (wt%)	O (wt%)	Total
KS-08(2)	0.08	0.18	0.09	0.05	0.05	0.02	65.53	0.13	0.14	0.03	25.51	91.79
KS-08(3)	0.16	0.44	0.62	0.26	0.08	0.02	65.58	0.08	0.13	0.02	26.50	93.88
KS-08(4)	0.19	0.49	0.32	0.13	0.10	0.02	67.29	0.12	0.05	0.05	26.84	95.60
KS-08(5)	0.16	0.65	0.96	0.32	0.06	0.03	63.87	0.11	0.11	0.03	26.45	92.75
KS-08(6)	0.07	0.27	0.20	0.12	0.01	0.03	65.00	0.07	0.16	0.03	25.51	91.46
KS-08(10)	0.05	0.36	0.29	0.17	0.04	0.02	64.27	0.09	0.10	0.03	25.43	90.86
KS-08(11)	0.07	0.44	0.35	0.20	0.06	0.02	64.15	0.11	0.15	0.03	25.58	91.17
KS-08(12)	0.13	0.32	0.36	0.18	0.04	0.03	66.54	0.06	0.21	0.04	26.42	94.31
KS-15(2)	0.07	0.27	0.45	0.17	0.04	0.00	68.90	0.11	0.12	0.04	27.31	97.48
KS-15(3)	0.04	0.14	0.38	0.13	0.05	0.03	71.25	0.10	0.03	0.08	27.99	100.22
KS-15(4)	0.05	0.18	0.44	0.17	0.03	0.00	70.28	0.09	0.17	0.03	27.74	99.19
KS-15(5)	0.01	0.04	0.31	0.04	0.01	0.01	68.98	0.08	0.10	0.01	26.83	96.40
KS-15(6)	0.04	0.22	0.53	0.12	0.05	0.01	67.16	0.11	0.14	0.04	26.66	95.06
KS-15(8)	0.04	0.13	0.32	0.04	0.02	0.01	71.70	0.08	0.04	0.02	27.97	100.37
KS-15(9)	0.04	0.07	0.25	0.07	0.03	0.00	70.31	0.07	0.02	0.02	27.32	98.21
KS-15(11)	0.00	0.03	0.23	0.01	0.02	0.01	70.86	0.11	0.02	0.03	27.44	98.75
KS-17(1)	0.10	0.30	0.22	0.12	0.00	0.02	69.35	0.13	0.00	0.03	27.19	97.47
KS-17(2)	0.18	0.68	0.62	0.23	0.06	0.00	69.38	0.07	0.05	0.02	28.12	99.40
KS-17(3)	0.06	0.26	0.38	0.22	0.00	0.04	70.10	0.07	0.03	0.02	27.63	98.82
KS-17(4)	0.05	0.26	0.56	0.22	0.02	0.01	69.66	0.05	0.09	0.02	27.67	98.60
KS-17(7)	0.09	0.44	0.60	0.28	0.01	0.02	69.78	0.13	0.03	0.02	27.97	99.34
KS-17(8)	0.07	0.45	0.52	0.29	0.00	0.03	70.27	0.11	0.08	0.01	28.08	99.92
KS-17(9)	0.29	0.56	0.50	0.22	0.05	0.09	70.80	0.09	0.00	0.05	28.51	101.14
KS-17(11)	0.42	0.52	0.61	0.27	0.03	0.00	69.36	0.19	0.03	0.03	28.14	99.59
KS-17(12)	0.43	0.58	0.69	0.30	0.05	0.00	69.34	0.18	0.00	0.03	28.29	99.87
KS-17(13)	0.63	0.86	0.79	0.27	0.09	0.02	68.29	0.16	0.03	0.03	28.43	99.60
KS-18(1)	0.01	0.03	0.00	0.03	0.03	0.00	71.04	0.04	0.04	0.06	27.27	98.57
KS-18(2)	0.02	0.07	0.20	0.06	0.01	0.02	68.31	0.09	0.03	0.08	26.52	95.39
KS-18(5)	0.00	0.03	0.01	0.02	0.02	0.02	70.37	0.05	0.04	0.02	27.00	97.60

Sample	Mg (wt%)	Al (wt%)	Si (wt%)	Ca (wt%)	Ti (wt%)	Cr (wt%)	Fe* (wt%)	Mn (wt%)	Na (wt%)	V (wt%)	O (wt%)	Total
KS-18(6)	0.00	0.02	0.00	0.02	0.01	0.03	71.72	0.03	0.07	0.06	27.51	99.47
KS-18(7)	0.00	0.03	0.00	0.00	0.01	0.00	71.47	0.02	0.05	0.04	27.39	99.01
KS-18(8)	0.03	0.04	0.21	0.06	0.02	0.03	71.10	0.06	0.03	0.04	27.57	99.21
KS-18(9)	0.04	0.07	0.48	0.28	0.03	0.01	69.55	0.10	0.01	0.06	27.40	98.02
KS-18(10)	0.03	0.04	0.09	0.08	0.02	0.00	71.61	0.05	0.02	0.08	27.62	99.64
KS-18(11)	0.04	0.03	0.19	0.11	0.01	0.05	71.59	0.10	0.11	0.03	27.78	100.04
KS-19(1)	0.00	0.08	0.06	0.01	0.04	0.02	69.36	0.07	0.00	0.04	26.72	96.40
KS-19(2)	0.07	0.27	0.45	0.17	0.04	0.00	68.90	0.11	0.12	0.04	27.31	97.48
KS-19(3)	0.09	0.21	0.08	0.03	0.14	0.03	70.34	0.20	0.07	0.05	27.44	98.68
KS-19(5)	0.11	0.37	0.35	0.12	0.09	0.03	70.97	0.11	0.00	0.05	28.09	100.29
KS-19(6)	0.02	0.31	0.05	0.02	0.15	0.11	70.43	0.11	0.01	0.04	27.47	98.71
KS-19(8)	0.13	0.19	0.00	0.01	0.12	0.00	70.43	0.13	0.09	0.02	27.33	98.46
KS-19(9)	0.07	0.28	0.14	0.05	0.11	0.06	70.59	0.10	0.04	0.03	27.60	99.07
KS-19(10)	0.09	0.43	0.44	0.14	0.14	0.02	69.71	0.14	0.05	0.04	27.82	99.03
KS-25(1)	0.17	0.57	0.46	0.22	0.03	0.01	67.17	0.08	0.10	0.02	26.99	95.82
KS-25(3)	0.12	0.58	0.51	0.21	0.03	0.03	65.88	0.12	0.03	0.03	26.53	94.08
KS-25(4)	0.12	0.51	0.39	0.15	0.06	0.00	66.67	0.12	0.05	0.02	26.62	94.72
KS-25(5)	0.17	0.55	0.05	0.23	0.05	0.00	64.95	0.01	0.08	0.06	25.67	91.83
KS-25(6)	0.40	0.70	0.09	0.35	0.08	0.04	63.81	0.02	0.11	0.04	25.65	91.29
KS-25(7)	0.20	0.51	0.03	0.17	0.08	0.01	65.39	0.03	0.02	0.05	25.78	92.28
KS-25(8)	0.11	0.54	0.03	0.15	0.08	0.01	65.12	0.03	0.01	0.03	25.60	91.69
KS-25(10)	0.08	0.41	0.04	0.24	0.02	0.00	64.71	0.03	0.12	0.05	25.38	91.08
KS-25(11)	0.13	0.35	0.04	0.17	0.02	0.02	66.34	0.02	0.02	0.04	25.91	93.06
KS-25(14)	0.21	0.62	0.05	0.19	0.11	0.03	64.94	0.03	0.13	0.02	25.78	92.10
KS-26(1)	0.02	0.22	0.41	0.10	0.10	0.01	68.71	0.15	0.04	0.01	27.10	96.87
KS-26(2)	0.05	0.50	0.47	0.17	0.12	0.00	69.39	0.13	0.06	0.03	27.74	98.65
KS-26(4)	0.05	0.29	0.30	0.19	0.05	0.01	69.41	0.07	0.00	0.02	27.29	97.67
KS-26(5)	0.03	0.30	0.02	0.04	0.12	0.02	67.39	0.11	0.02	0.06	26.23	94.33
KS-26(6)	0.03	0.30	0.25	0.10	0.10	0.03	66.96	0.20	0.00	0.06	26.36	94.37

Sample	Mg (wt%)	Al (wt%)	Si (wt%)	Ca (wt%)	Ti (wt%)	Cr (wt%)	Fe* (wt%)	Mn (wt%)	Na (wt%)	V (wt%)	O (wt%)	Total
KS-26(7)	0.00	0.07	0.00	0.01	0.04	0.01	70.46	0.06	0.00	0.02	27.04	97.72
KS-26(8)	0.06	0.37	0.44	0.13	0.12	0.01	69.89	0.07	0.08	0.04	27.77	98.97
KS-26(9)	0.01	0.18	0.12	0.02	0.10	0.01	70.57	0.07	0.00	0.04	27.38	98.49
KS-26(10)	0.04	0.36	0.27	0.15	0.11	0.03	69.68	0.08	0.03	0.06	27.49	98.29
KS-26(11)	0.07	0.23	0.08	0.07	0.08	0.02	70.86	0.09	0.01	0.05	27.56	99.13
KS-38(2)	0.03	0.15	0.31	0.10	0.01	0.00	70.72	0.06	0.00	0.07	27.63	99.08
KS-38(3)	0.02	0.05	0.16	0.07	0.00	0.00	68.92	0.04	0.01	0.03	26.64	95.93
KS-38(4)	0.02	0.19	0.33	0.14	0.03	0.11	69.90	0.07	0.05	0.04	27.46	98.35
KS-38(6)	0.06	0.26	0.61	0.20	0.05	0.02	68.98	0.10	0.02	0.06	27.52	97.88
KS-38(8)	0.12	0.43	0.71	0.09	0.02	0.00	67.22	0.04	0.04	0.03	27.04	95.74
KS-38(11)	0.02	0.20	0.19	0.10	0.04	0.00	70.11	0.05	0.06	0.03	27.31	98.11
KS-38(13)	0.05	0.20	0.42	0.17	0.02	0.01	70.53	0.07	0.05	0.01	27.76	99.29
KS-19 Light(1a)	0.04	0.24	0.14	0.05	0.13	0.05	70.69	0.09	0.02	0.03	27.58	99.06
KS-19 Light(1b)	0.06	0.34	0.16	0.06	0.14	0.04	71.12	0.12	0.04	0.04	27.90	100.04
KS-19 Light(1c)	0.09	0.47	0.23	0.16	0.12	0.00	70.28	0.06	0.03	0.00	27.76	99.19
KS-19 Dark(1d)	0.20	0.98	1.32	0.48	0.09	0.01	67.60	0.15	0.24	0.02	28.72	99.81
KS-19 Dark(1e)	0.24	0.74	0.83	0.21	0.04	0.00	68.42	0.14	0.17	0.01	28.12	98.92
KS-19 Light(2)	0.04	0.22	0.12	0.02	0.14	0.06	70.76	0.12	0.04	0.05	27.60	99.18
KS-19 Dark(3)	0.3549	0.7132	0.8916	0.2991	0.0824	0.0015	67.78	0.1145	0	0.0429	28.01	98.29

Appendix C: Full Trace Element Dataset by Laser Ablation-Inductively Coupled Plasma-Mass Spectrometry

Table C1. Trace element concentrations (ppm) in synthetic glass standard NIST 610 from the National Institute for Standards and Technology (NIST). The average value of all measurements and accepted values by National Institute of Standards and Technology (2012a) and reference therein are given at the end the end of the table. SD = Standard Deviation.

Sample	²³ Na (ppm)	2SD	²⁴ Mg (ppm)	2SD	²⁵ Mg (ppm)	2SD	²⁷ Al (ppm)	2SD	²⁹ Si (ppm)	2SD	⁴³ Ca (ppm)	2SD	⁴⁷ Ti (ppm)	2SD
NIST 610	98673	17410	428	92	438	125	10859	2125	330397	64638	81786	16115	450	98
NIST 610	100090	21897	440	98	428	107	10864	2126	328935	54232	82990	13924	460	111
NIST 610	98870	16886	434	73	432	97	10655	1533	324221	56196	81297	12691	451	117
NIST 610	102936	22367	433	92	434	127	10927	2075	326487	60388	82999	12957	451	90
NIST 610	97474	15921	418	85	430	91	10773	1742	323691	53818	81314	11974	446	99
NIST 610	100322	17706	436	80	432	118	10872	1857	326836	63187	81720	15295	449	90
NIST 610	99098	34462	446	168	434	179	10506	3031	327762	112298	83601	27074	451	172
NIST 610	98805	23032	425	90	435	121	10704	1936	328716	73218	82602	17566	477	182
NIST 610	99463	17355	433	82	432	126	10827	1490	331410	80802	83460	18093	456	114
NIST 610	100117	19397	438	97	431	102	10974	2419	327439	59508	81682	13168	449	102
NIST 610	99405	14323	432	82	434	123	10803	1231	327222	86959	82502	21403	453	140
NIST 610	99466	11594	433	91	430	145	10700	1171	328021	100708	82655	22807	453	138
NIST 610	98866	13863	431	117	431	131	10841	1036	331236	85550	82559	18381	453	139
NIST 610	100726	15905	432	92	432	107	10907	1397	329586	109013	81881	17811	451	133
NIST 610	98508	13765	424	98	430	145	10641	1598	320891	83960	81384	21380	445	125
NIST 610	98862	13342	436	90	433	119	10913	1192	325474	73211	82164	18554	456	119
NIST 610	99341	12945	431	89	425	116	10700	1121	324937	76259	81107	17336	444	132
NIST 610	100769	12712	436	84	439	120	10832	1207	329359	81585	81504	22132	460	115
NIST 610	99510	12278	428	93	427	109	10663	1316	328635	76640	82730	20192	443	135
NIST 610	98924	12341	435	99	441	137	10885	1044	328154	70062	83247	19838	461	143
NIST 610	99318	13218	431	104	434	137	10779	919	325859	84338	80910	22630	459	156
NIST 610	99507	12224	433	102	433	136	10829	1043	328162	81764	82924	17729	448	117
NIST 610	99921	13896	434	83	443	133	10807	1042	327946	72550	81966	18294	448	114
NIST 610	98920	12097	430	88	423	141	10795	1010	327060	81190	82111	21238	455	126
NIST 610	99463	11861	431	79	424	111	10806	984	327464	82777	81797	19681	450	110
NIST 610	99814	13982	437	91	437	147	10820	1183	326737	69086	82983	18819	457	103
NIST 610	98635	11555	430	90	434	130	10738	964	324553	87303	82327	21464	457	126
NIST 610	100355	16927	426	103	422	155	10739	1226	328952	87962	81479	20611	442	136
NIST 610	99632	26378	432	119	434	179	10957	1643	328939	89069	81969	18866	449	176
NIST 610	99479	23307	436	135	438	196	10742	1369	325534	95118	82457	22812	457	187
Average	99509	16498	432	96	432	130	10795	1468	327354	78446	82204	18694	453	128
Accepted	-	-	-	-	-	-	-	-	-	-	-	-	437	-

Sample	⁴⁹ Ti (ppm)	2SD	⁵¹ V (ppm)	2SD	⁵² Cr (ppm)	2SD	⁵³ Cr (ppm)	2SD	⁵⁵ Mn (ppm)	2SD	⁵⁶ Fe (ppm)	2SD	⁵⁷ Fe (ppm)	2SD
NIST 610	458	129	455	94	411	85	397	103	438	87	458	130	463	216
NIST 610	453	111	456	98	411	86	421	107	458	114	469	138	457	156
NIST 610	449	157	441	84	404	75	408	88	442	87	452	85	450	174
NIST 610	447	106	451	85	408	79	412	99	448	83	464	104	469	136
NIST 610	446	121	446	71	406	62	400	68	434	87	454	109	459	216
NIST 610	456	101	451	81	409	70	414	90	445	72	452	88	450	150
NIST 610	453	168	442	129	400	113	396	135	446	126	456	175	442	187
NIST 610	450	143	455	141	412	95	422	111	445	124	468	119	451	179
NIST 610	463	119	450	79	415	77	410	59	448	64	466	102	460	182
NIST 610	442	133	454	69	405	76	404	85	439	92	453	88	471	158
NIST 610	451	100	456	71	409	111	409	63	444	109	459	109	461	103
NIST 610	453	140	445	61	404	104	406	65	448	145	459	119	457	98
NIST 610	450	129	451	49	412	100	407	59	440	101	461	112	452	108
NIST 610	464	147	449	47	412	118	409	67	455	131	463	121	464	120
NIST 610	447	114	448	72	402	105	408	58	442	108	454	100	461	119
NIST 610	452	109	453	47	410	96	407	58	437	111	449	106	456	123
NIST 610	451	112	447	49	409	95	411	58	443	113	458	107	459	106
NIST 610	453	106	449	59	406	96	410	58	446	120	459	101	453	99
NIST 610	446	141	449	56	407	97	408	42	443	116	456	97	456	125
NIST 610	460	132	452	44	410	101	406	58	449	113	463	91	464	121
NIST 610	455	150	446	56	407	104	409	69	443	121	449	115	451	139
NIST 610	451	122	454	57	409	95	407	58	445	108	464	96	473	235
NIST 610	452	141	450	57	410	70	412	75	442	86	453	99	464	160
NIST 610	459	129	449	62	404	87	405	63	448	108	462	92	460	140
NIST 610	442	113	449	56	407	94	401	71	443	93	459	87	463	186
NIST 610	460	148	453	63	409	80	413	54	449	104	460	94	451	138
NIST 610	444	128	448	47	409	104	405	91	443	115	456	102	469	189
NIST 610	454	131	452	69	406	99	407	65	437	117	452	121	449	157
NIST 610	451	188	452	96	413	112	412	114	447	129	460	147	464	371
NIST 610	458	173	449	103	403	121	404	135	444	139	459	155	457	401
Average	452	131	450	72	408	94	408	78	444	107	458	110	459	166
Accepted	437	-	-	-	415	-	415	-	457	-	458	-	458	-

Sample	⁵⁹ Co (ppm)	2SD	⁶⁰ Ni (ppm)	2SD	⁶³ Cu (ppm)	2SD	⁶⁶ Zn (ppm)	2SD	⁷¹ Ga (ppm)	2SD	¹¹⁸ Sn (ppm)	2SD
NIST 610	406	87	446	93	446	89	467	120	433	90	421	87
NIST 610	416	102	472	82	441	82	454	125	437	111	435	104
NIST 610	409	72	457	89	438	85	455	91	432	93	434	100
NIST 610	413	88	469	106	445	85	467	99	440	98	440	112
NIST 610	409	67	452	73	434	53	460	93	426	69	424	71
NIST 610	409	64	454	62	444	84	460	88	434	100	437	96
NIST 610	403	142	467	138	447	131	462	155	430	134	440	141
NIST 610	411	99	463	95	448	101	446	122	434	106	433	100
NIST 610	412	81	455	79	449	85	462	98	438	86	428	81
NIST 610	411	87	466	86	436	77	465	107	433	89	428	80
NIST 610	410	101	456	76	441	102	458	100	436	112	431	67
NIST 610	410	118	459	92	447	110	461	109	430	108	427	67
NIST 610	410	108	466	81	439	96	463	84	432	98	425	68
NIST 610	414	129	460	85	440	125	457	91	435	126	432	79
NIST 610	403	117	456	75	439	103	456	88	430	106	431	79
NIST 610	413	106	458	82	443	93	466	83	436	105	437	82
NIST 610	408	111	455	69	437	91	462	87	429	96	432	77
NIST 610	410	102	460	88	440	99	455	96	437	101	432	73
NIST 610	404	105	458	72	443	102	457	84	434	104	423	74
NIST 610	419	114	462	75	446	116	463	87	432	106	431	68
NIST 610	406	109	455	92	441	120	462	101	428	129	427	94
NIST 610	414	110	462	81	440	126	458	93	442	127	434	103
NIST 610	409	92	460	72	429	101	462	78	437	124	431	121
NIST 610	410	102	457	70	456	105	457	96	432	120	427	84
NIST 610	410	102	456	84	449	110	456	95	428	116	432	120
NIST 610	413	100	464	80	434	109	461	85	431	111	433	91
NIST 610	407	108	457	86	433	108	464	94	425	123	424	114
NIST 610	406	115	456	101	445	144	461	101	432	137	431	118
NIST 610	409	127	461	143	456	133	443	288	439	165	446	173
NIST 610	413	144	458	138	426	146	466	268	436	173	419	153
Average	410	104	459	88	442	104	460	110	433	112	431	96
Accepted	390	-	459	-	444	-	433	-	-	-	-	-

Table C2. Trace element concentrations (ppm) in synthetic glass standard NIST 612 from the National Institute for Standards and Technology (NIST). The average value of all measurements and accepted values by National Institute of Standards and Technology (2012b) and reference therein are given at the end. SD = standard deviation.

Sample	²³ Na (ppm)	2SD	²⁴ Mg (ppm)	2SD	²⁵ Mg (ppm)	2SD	²⁷ Al (ppm)	2SD	²⁹ Si (ppm)	2SD	⁴³ Ca (ppm)	2SD	⁴⁷ Ti (ppm)	2SD
NIST 612	97297	31402	53	22	56	41	11170	3091	341238	99657	84482	25292	45	28
NIST 612	92607	29177	53	20	54	44	11458	4132	347971	109829	86296	18610	42	26
NIST 612	101866	28098	57	21	55	39	11062	2195	324750	67393	84250	20629	41	36
NIST 612	104717	38786	57	27	58	56	11773	2936	340796	77598	84771	18237	40	41
NIST 612	105328	30413	59	21	57	49	11524	2451	338558	60636	85712	13206	40	33
NIST 612	104108	20405	58	18	67	54	11447	2262	325643	59313	83718	16016	45	39
NIST 612	104416	33542	58	25	53	47	11016	3037	323565	93833	83853	17656	43	42
NIST 612	103573	39320	55	25	58	40	10771	2816	334839	110213	85696	22845	46	29
NIST 612	104722	24921	56	20	56	36	11519	3820	334950	100753	85441	20291	38	33
NIST 612	102799	18838	58	21	53	26	11065	2508	335343	86336	84774	21525	49	29
NIST 612	100918	27611	58	34	58	42	11387	2520	356268	228880	89808	52526	44	34
NIST 612	102656	24534	59	34	56	42	11249	2442	345525	212509	88149	54570	43	33
NIST 612	104529	19892	60	34	60	47	11332	1982	355067	236557	89030	51409	44	33
NIST 612	102257	22599	57	32	56	41	11318	2316	350146	223594	88389	51104	43	32
NIST 612	103354	21378	57	30	59	43	11372	2136	353115	219212	89115	52321	41	27
NIST 612	102474	22893	57	29	55	44	11190	1641	345647	218242	88253	51497	42	34
NIST 612	103313	23306	58	34	56	40	11205	2100	346807	225957	89128	52690	40	29
NIST 612	99431	22289	56	34	55	41	11061	2481	349071	227878	88425	52575	39	27
NIST 612	101639	21999	59	35	59	44	11411	1963	355622	228827	88899	50596	42	33
NIST 612	101252	19418	58	30	59	38	11237	2086	354960	207739	88597	50276	42	30
NIST 612	98406	14777	54	18	58	39	11118	1411	328382	69415	84668	15230	40	35
NIST 612	99873	13587	55	15	60	32	11295	1357	329186	70557	85839	17485	38	24
NIST 612	98634	17762	57	20	59	33	11228	1787	324062	58104	84286	17472	38	26
NIST 612	101306	21165	57	15	56	36	11341	1738	333943	57999	83804	14461	40	31
NIST 612	101762	17154	58	21	60	43	11307	1414	332485	58241	83991	17441	43	25
NIST 612	99638	21882	57	18	54	40	11199	2069	328682	71769	83995	16699	40	34
NIST 612	101473	19024	57	23	56	47	11289	1564	333672	87334	83445	19215	41	29
NIST 612	100646	15401	58	24	58	41	11168	1662	329538	82337	85079	21957	37	36
NIST 612	91873	24865	51	24	58	56	11022	2339	317664	74355	84508	19916	35	36
NIST 612	94115	29205	54	22	55	56	11063	2787	317919	80758	84459	23274	38	44
Average	101033	23855	57	25	57	42	11253	2301	337847	126861	86029	29901	41	32
Accepted	-	-	-	-	-	-	-	-	-	-	-	-	50	-

Sample	⁴⁹ Ti (ppm)	2SD	⁵¹ V (ppm)	2SD	⁵² Cr (ppm)	2SD	⁵³ Cr (ppm)	2SD	⁵⁵ Mn (ppm)	2SD	⁵⁶ Fe (ppm)	2SD	⁵⁷ Fe (ppm)	2SD
NIST 612	43	38	38	13	34	17	36	21	37	17	51	67	160	203
NIST 612	39	35	39	16	36	17	39	21	38	13	55	43	165	200
NIST 612	46	49	39	12	35	16	39	26	41	12	69	153	155	235
NIST 612	45	40	38	13	34	16	37	31	39	16	45	70	154	227
NIST 612	46	43	38	13	36	15	37	21	38	12	55	74	136	209
NIST 612	37	45	39	12	36	18	33	25	38	14	68	72	165	298
NIST 612	38	44	39	16	37	17	38	26	38	14	42	75	168	252
NIST 612	43	40	40	17	38	21	36	28	41	17	40	69	166	258
NIST 612	39	33	39	12	37	19	36	20	41	16	48	53	161	171
NIST 612	37	28	40	13	37	16	36	21	38	13	54	40	167	152
NIST 612	41	30	39	10	37	24	35	12	40	25	50	35	84	65
NIST 612	43	32	39	10	37	24	35	15	40	29	52	35	92	65
NIST 612	45	30	38	8	38	24	35	11	40	27	48	29	90	68
NIST 612	39	31	38	7	36	23	37	14	40	27	47	32	83	56
NIST 612	42	29	39	10	38	22	37	12	41	27	51	33	92	75
NIST 612	40	30	38	8	38	25	35	10	39	27	49	31	92	46
NIST 612	42	28	38	8	39	23	37	16	39	26	50	34	90	57
NIST 612	43	33	38	10	38	25	37	13	40	26	51	28	84	65
NIST 612	40	27	39	8	39	24	37	13	40	26	51	26	89	64
NIST 612	43	30	39	9	38	21	38	16	40	26	51	30	87	64
NIST 612	42	35	38	9	36	13	34	23	37	10	46	55	72	190
NIST 612	37	31	38	10	37	13	37	22	37	10	46	40	100	184
NIST 612	39	33	38	10	37	14	36	21	37	12	44	40	115	209
NIST 612	40	32	39	9	39	14	37	21	40	13	48	34	92	163
NIST 612	37	34	39	10	37	12	37	21	38	13	49	40	85	187
NIST 612	36	37	39	9	36	16	33	33	39	14	45	39	74	206
NIST 612	40	43	39	11	37	15	35	21	38	16	49	47	98	146
NIST 612	40	32	38	9	36	15	34	21	37	13	49	27	81	144
NIST 612	37	53	36	12	33	24	32	27	36	18	55	79	90	293
NIST 612	36	44	36	14	33	16	32	30	36	18	50	73	92	307
Average	41	36	38	11	37	19	36	20	39	18	50	50	113	162
Accepted	50	-	-	-	35	-	35	-	38	-	51	-	51	-

Sample	⁵⁹ Co (ppm)	2SD	⁶⁰ Ni (ppm)	2SD	⁶³ Cu (ppm)	2SD	⁶⁶ Zn (ppm)	2SD	⁷¹ Ga (ppm)	2SD	¹¹⁸ Sn (ppm)	2SD
NIST 612	32	13	37	19	38	14	32	23	36	15	36	16
NIST 612	35	14	37	22	39	12	34	25	36	15	36	13
NIST 612	37	16	40	22	41	15	38	33	37	14	40	16
NIST 612	36	17	41	23	42	16	38	32	38	21	39	15
NIST 612	35	12	38	24	41	13	38	24	40	17	40	18
NIST 612	35	12	38	22	42	16	39	32	41	13	39	13
NIST 612	37	19	40	24	42	18	42	28	40	19	38	18
NIST 612	36	19	40	21	41	17	39	21	39	17	39	19
NIST 612	35	12	40	23	42	19	35	25	38	14	39	11
NIST 612	34	12	41	17	40	12	36	20	36	11	37	13
NIST 612	36	23	41	16	39	20	36	15	37	22	37	12
NIST 612	36	26	40	14	40	22	37	15	37	22	37	12
NIST 612	37	26	39	15	40	22	36	18	38	22	38	11
NIST 612	36	27	39	16	38	20	37	20	37	21	37	13
NIST 612	36	24	38	14	41	24	36	18	39	22	38	11
NIST 612	36	23	40	15	39	25	38	18	37	21	37	12
NIST 612	36	25	38	16	41	23	38	17	38	23	39	14
NIST 612	35	24	40	18	40	24	36	17	36	20	37	10
NIST 612	37	25	39	14	41	24	37	20	38	22	38	13
NIST 612	37	24	40	15	41	22	37	20	38	20	38	11
NIST 612	34	10	37	13	38	10	36	21	33	10	35	9
NIST 612	33	9	37	15	39	13	36	20	35	11	35	7
NIST 612	32	11	37	16	39	12	36	26	35	11	34	9
NIST 612	35	13	41	20	39	15	34	27	34	13	35	12
NIST 612	34	10	37	17	41	11	37	28	35	10	36	11
NIST 612	34	12	36	17	39	14	36	25	34	9	35	11
NIST 612	34	12	37	17	40	11	34	30	35	12	37	10
NIST 612	34	11	37	16	39	14	36	25	33	11	36	11
NIST 612	32	14	34	23	35	17	39	43	34	14	33	14
NIST 612	31	14	33	22	37	19	38	35	34	15	35	15
Average	35	17	38	18	40	17	37	24	37	16	37	13
Accepted	36	-	39	-	38	-	-	-	39	-	-	-

Table C3. Trace element concentrations (ppm) in Columbia Basalt glass standard BCR-2GA, shortened to BCR2G within the table, from the United States Geological Survey (USGS). The average value of all measurements and accepted values by U.S. Geological Survey (2022b) and reference therein are given at the end the end of the table. SD = standard deviation.

Sample	²³ Na (ppm)	2SD	²⁴ Mg (ppm)	2SD	²⁵ Mg (ppm)	2SD	²⁷ Al (ppm)	2SD	²⁹ Si (ppm)	2SD	⁴³ Ca (ppm)	2SD	⁴⁷ Ti (ppm)	2SD
BCR2G	22650	4877	19117	2950	18101	2877	75192	11349	260242	51482	48647	8860	12725	1969
BCR2G	22767	4489	19480	2615	18540	3055	74786	11223	260072	51911	49760	7514	12956	1975
BCR2G	22739	4262	19390	2744	18944	2968	75396	12901	254952	51628	50207	8459	13135	2030
BCR2G	22568	3172	19643	2423	19012	3004	75315	9715	251617	35208	49499	8337	12931	1673
BCR2G	23148	4513	19818	3413	19392	2966	75498	11329	257815	45985	50026	10747	13120	1987
BCR2G	23219	3369	19772	2702	19314	3292	76001	10448	254242	43956	50039	8751	13242	1632
BCR2G	23224	5040	19892	2323	18482	2595	77272	10426	261780	57284	50463	9603	13276	2061
BCR2G	23279	4280	20113	3867	18615	3518	76390	14398	257632	54051	49604	10167	13377	2504
BCR2G	23247	5209	20609	4877	19167	3906	76644	14053	254990	59949	51747	11561	13389	2775
BCR2G	23848	4496	20602	3745	19390	3291	78585	14485	261707	64805	50905	8890	13649	2658
BCR2G	22651	2114	19179	1923	18636	1915	74417	6237	254799	44478	49473	6406	12784	1731
BCR2G	22821	3206	19326	4036	18733	4523	74288	7538	259124	64333	49977	9890	12741	2859
BCR2G	23791	3963	19886	5630	19126	6760	76012	7689	267943	105956	50594	17710	13060	4808
BCR2G	23949	3264	20236	5855	19103	6206	75390	6580	269512	94758	50243	14114	13191	4296
BCR2G	23559	3385	19903	3067	19006	3071	75443	6843	263329	56808	49224	7721	12878	2261
BCR2G	23336	3898	19933	2656	18989	3041	75339	6470	259950	45851	50411	8717	12922	1787
BCR2G	23287	3589	20110	3674	19158	4113	75163	7629	261217	65031	50005	9144	13053	2516
BCR2G	22944	4460	19703	4456	19006	5912	74759	7953	258723	75250	49753	13611	12962	3601
BCR2G	22968	3495	19824	3147	19114	4183	75226	8325	258927	55963	50542	10845	13175	3051
BCR2G	23114	4263	20507	4845	19420	4887	75576	8689	261937	72123	49436	11570	13168	3532
BCR2G	23127	4654	19768	4193	19506	5135	75379	7199	263679	78300	50664	12035	13032	3199
BCR2G	23258	4154	19804	4243	19628	4919	75244	5908	264066	76771	50920	12899	13066	3579
BCR2G	23633	4120	20223	5384	19575	6264	75930	6599	263903	93430	50391	14620	13475	4054
BCR2G	23592	4298	20250	4342	19654	4948	76317	7817	262134	74573	50034	14201	13342	3310
BCR2G	23524	4391	20323	4730	19433	5124	76901	6924	266836	79276	50528	15249	13212	3471
BCR2G	23550	4317	20449	4689	19564	5830	76628	6799	266123	81725	50532	13595	13095	3820
BCR2G	23799	4714	20190	5003	19292	6005	76319	8107	267816	89180	49797	14066	13442	3841
BCR2G	23758	4421	20212	5030	19292	5788	76772	8035	267320	93645	50403	14377	13438	4082
BCR2G	23240	6045	18683	3378	18911	4148	76265	8889	275920	88623	49839	12053	12305	2545
BCR2G	23412	6020	18577	2836	18829	3700	76033	7674	275709	86356	49762	11482	12153	2024
Average	23267	4216	19851	3826	19098	4265	75816	8941	262134	67956	50114	11240	13077	2854
Accepted	-	-	-	-	-	-	-	-	-	-	-	-	-	-

Sample	⁴⁹ Ti (ppm)	2SD	⁵¹ V (ppm)	2SD	⁵² Cr (ppm)	2SD	⁵³ Cr (ppm)	2SD	⁵⁵ Mn (ppm)	2SD	⁵⁶ Fe (ppm)	2SD	⁵⁷ Fe (ppm)	2SD
BCR2G	12845	2483	421	78	15	6	14	8	1473	252	92380	18989	66353	12569
BCR2G	13089	1784	433	80	15	5	15	9	1525	250	93559	17582	67278	11360
BCR2G	12998	1953	428	72	15	6	14	10	1508	249	95785	19914	68269	12651
BCR2G	12872	1843	421	61	15	6	14	9	1491	223	94367	13089	67411	9648
BCR2G	12995	1937	432	77	15	5	14	10	1519	273	97988	19097	69689	12977
BCR2G	12977	2055	430	44	18	18	17	22	1519	206	97293	14357	69136	10512
BCR2G	13163	2274	434	71	16	6	13	9	1532	294	96173	14877	69141	13113
BCR2G	12870	2403	435	81	16	6	16	8	1520	238	97573	21593	70256	12703
BCR2G	13487	2927	436	97	16	6	16	10	1534	325	98069	23843	70818	16512
BCR2G	13535	2564	433	69	17	7	15	10	1530	257	98917	21661	72199	13024
BCR2G	12962	1227	421	34	15	4	14	6	1505	192	91971	11084	82305	8122
BCR2G	13128	2613	417	45	15	5	15	6	1498	334	93654	19153	83171	10793
BCR2G	13460	4287	435	68	16	6	14	7	1550	575	96562	26489	85802	13515
BCR2G	13307	3393	428	66	15	6	15	7	1552	510	96144	23172	86246	13245
BCR2G	13182	2113	433	41	16	5	15	6	1543	277	96365	16614	86888	8780
BCR2G	13010	1805	430	46	15	4	16	7	1532	238	96048	15647	86005	9100
BCR2G	13103	2533	426	69	16	4	15	7	1539	309	97137	20299	87742	14445
BCR2G	13175	3812	419	55	15	5	15	7	1542	491	97226	24853	87846	10767
BCR2G	12992	2485	425	51	16	5	15	7	1533	303	97174	19156	88747	13775
BCR2G	13083	2562	430	61	16	6	16	7	1531	404	98159	20926	89730	12472
BCR2G	13134	3054	428	52	15	6	15	10	1549	443	95832	24329	87140	14953
BCR2G	13134	2996	431	57	16	6	15	9	1552	428	96781	22945	87689	14833
BCR2G	13479	3664	433	66	16	6	15	9	1567	508	97831	26150	84872	14083
BCR2G	13339	3060	433	56	16	6	15	9	1566	436	98171	23898	85177	13549
BCR2G	13389	3397	438	57	16	6	16	10	1574	425	99288	22424	88757	14956
BCR2G	13441	3560	436	60	17	6	15	12	1583	452	98696	25089	88285	14030
BCR2G	13289	3477	438	60	16	8	15	9	1563	492	98621	27884	88004	17275
BCR2G	13333	3658	442	62	16	7	16	10	1554	564	99150	28872	88411	15459
BCR2G	13146	2605	419	79	16	9	14	12	1498	369	98769	29895	90916	24433
BCR2G	13101	2321	418	74	16	9	14	13	1493	339	98205	29799	91030	23953
Average	13167	2695	429	63	16	6	15	9	1533	355	96796	21456	81177	13587
Accepted	-	-	-	-	-	-	-	-	-	-	-	-	-	-

Sample	⁵⁹ Co (ppm)	2SD	⁶⁰ Ni (ppm)	2SD	⁶³ Cu (ppm)	2SD	⁶⁶ Zn (ppm)	2SD	⁷¹ Ga (ppm)	2SD	¹¹⁸ Sn (ppm)	2SD
BCR2G	38	8	12	6	18	6	174	53	21	6	2	2
BCR2G	38	8	12	6	18	7	175	46	21	5	2	1
BCR2G	38	9	11	5	17	5	176	42	22	6	2	1
BCR2G	39	8	12	7	17	5	177	48	21	7	2	1
BCR2G	38	9	13	7	17	6	180	43	22	7	2	2
BCR2G	39	8	13	8	18	5	174	48	22	6	2	2
BCR2G	38	10	13	7	18	5	170	52	22	6	2	1
BCR2G	39	10	12	5	18	6	172	49	21	6	2	1
BCR2G	40	10	13	7	17	6	168	53	22	8	2	2
BCR2G	41	12	13	6	18	5	175	58	22	6	2	2
BCR2G	38	6	12	5	17	4	169	27	21	4	2	1
BCR2G	38	12	13	6	17	5	169	36	21	6	2	1
BCR2G	39	15	12	6	18	8	167	34	21	8	2	1
BCR2G	40	15	12	4	17	6	172	32	22	8	2	1
BCR2G	38	8	13	5	17	6	169	34	22	5	2	1
BCR2G	39	9	13	6	17	4	167	31	22	6	2	1
BCR2G	38	11	12	5	17	5	166	31	21	5	2	1
BCR2G	39	14	12	6	17	6	173	33	21	6	2	1
BCR2G	38	9	12	6	17	5	170	30	21	5	2	1
BCR2G	38	11	12	4	17	6	171	26	22	6	2	1
BCR2G	40	14	13	6	18	7	169	46	21	6	2	2
BCR2G	40	15	13	7	18	7	168	51	21	8	2	2
BCR2G	40	15	13	7	18	8	160	44	21	7	2	1
BCR2G	39	13	12	7	18	8	161	43	22	8	2	1
BCR2G	40	14	13	7	18	7	165	39	21	9	2	2
BCR2G	40	14	12	7	18	7	163	36	21	8	2	2
BCR2G	41	16	13	7	19	9	166	52	21	7	2	1
BCR2G	40	16	12	8	18	8	175	52	21	7	2	1
BCR2G	41	15	14	10	19	9	202	67	24	11	2	2
BCR2G	40	16	13	11	19	9	206	76	24	10	2	2
Average	39	12	13	7	18	6	172	44	22	7	2	1
Accepted	36	-	11	-	-	-	-	-	21	-	-	-

Table C4. Trace element concentrations (ppm) in Keystone Fe ore collected in 2022 measured by LA-ICP-MS. The numbers in parentheses represent the spot analysis number. All data were processed using Fe as the internal standard based on EMPA Fe analyses. SD = Standard Deviation; LOD = Limit of Detection.

Sample	²³ Na (ppm)	2SD	²⁴ Mg (ppm)	2SD	²⁵ Mg (ppm)	2SD	²⁷ Al (ppm)	2SD	²⁹ Si (ppm)	2SD	⁴³ Ca (ppm)	2SD	⁴⁴ Ca (ppm)	2SD
KS-08(2)	51	119	797	604	792	559	1924	653	2235	1289	351	995	253	583
KS-08(3)	1013	835	2988	516	3018	754	7309	1196	9772	3149	3550	2112	3587	1112
KS-08(4)	981	247	3193	1425	3245	1461	8317	2005	10000	2818	4897	2368	4781	1161
KS-08(5)	798	180	1403	377	1397	400	7220	1271	8452	2942	3164	1456	3400	875
KS-08(6)	665	168	1485	302	1480	252	5875	724	7171	1683	2913	1657	2947	643
KS-08(10)	1005	598	1748	1798	1735	1869	8420	4912	8643	5467	2573	2176	2891	1979
KS-08(11)	859	193	3337	739	3338	633	8051	1414	9844	3574	3933	1385	3985	953
KS-08(12)	965	1152	1838	456	1890	459	8443	1142	8241	4933	3083	2407	3019	1861
KS-15(2)	698	2397	1715	2861	1704	2831	2849	2432	8965	8792	1338	1162	1428	861
KS-15(3)	229	93	284	157	286	181	1161	441	4380	1930	942	818	986	475
KS-15(4)	239	138	1645	3451	1576	3353	2440	3426	6839	7783	1380	2151	1184	1139
KS-15(5)	66	43	279	406	277	463	578	402	2103	1724	296	508	397	352
KS-15(6)	251	51	250	60	255	65	2162	374	3734	1070	1156	599	1126	231
KS-15(8)	277	246	300	260	305	272	1411	1334	3736	2518	1019	1173	1029	1066
KS-15(9)	333	146	339	153	337	177	2477	1106	4297	1321	1558	877	1520	742
KS-15(11)	505	477	1932	3705	1910	3519	4209	4817	8214	9252	2244	2135	2275	1863
KS-17(1)	1602	741	3935	1500	4132	2018	8656	2867	12761	5195	5024	3141	4642	1555
KS-17(2)	1650	436	4241	1060	4365	1070	10973	2254	13354	3395	4742	2513	4328	1042
KS-17(3)	818	568	1853	892	1861	863	5202	2276	9501	6597	3582	3103	3167	1379
KS-17(4)	853	141	1965	620	2036	682	6135	1541	9957	2237	3239	1861	3170	800
KS-17(7)	635	135	1123	233	1169	353	5655	1118	8000	2223	3765	2558	3642	909
KS-17(8)	1121	356	2572	1073	2573	869	6873	2640	10968	4159	4367	3094	4324	1490
KS-17(9)	1016	258	3918	999	4042	1408	8013	1457	9403	2575	2980	2237	3051	692
KS-17(11)	974	174	4292	895	4343	796	7509	1256	10040	2419	3454	2091	3719	842
KS-17(12)	1082	602	3370	1631	3440	1744	8154	2810	10372	4393	3876	2994	3840	1728
KS-17(13)	431	173	549	183	561	227	4310	1200	4434	1944	1160	1286	1389	627
KS-18(1)	25	32	61	51	65	56	390	141	2756	2692	<LOD	-	135	216
KS-18(2)	98	61	122	87	120	94	475	167	2937	2397	555	1112	386	302
KS-18(5)	150	69	405	477	360	419	847	574	4950	3643	938	1220	722	461

Sample	⁴⁷ Ti (ppm)	2SD	⁴⁹ Ti (ppm)	2SD	⁵¹ V (ppm)	2SD	⁵² Cr (ppm)	2SD	⁵³ Cr (ppm)	2SD	⁵⁵ Mn (ppm)	2SD
KS-08(2)	719	279	722	226	91	43	<LOD	-	2	6	1149	321
KS-08(3)	772	165	764	196	103	21	<LOD	-	<LOD	-	1201	218
KS-08(4)	2681	1001	2773	869	244	52	<LOD	-	<LOD	-	1627	619
KS-08(5)	636	172	611	173	89	19	<LOD	-	<LOD	-	1154	254
KS-08(6)	530	135	515	145	90	16	5	6	4	7	1143	166
KS-08(10)	1009	561	1031	633	207	50	7	16	7	15	1153	363
KS-08(11)	804	220	736	177	150	26	5	6	5	6	1380	267
KS-08(12)	1263	243	1249	236	186	32	173	62	173	78	1268	217
KS-15(2)	316	106	323	130	209	27	45	100	43	98	926	299
KS-15(3)	273	217	250	163	159	29	9	8	8	8	784	309
KS-15(4)	163	113	174	133	164	34	135	149	143	156	775	422
KS-15(5)	575	654	574	588	252	59	3	4	2	5	645	283
KS-15(6)	340	72	340	82	90	16	1	3	1	3	794	156
KS-15(8)	224	171	222	156	137	26	2	4	2	4	823	344
KS-15(9)	389	102	385	98	104	17	<LOD	-	<LOD	-	930	161
KS-15(11)	411	174	417	177	109	36	2	5	<LOD	-	1026	369
KS-17(1)	424	177	427	190	108	14	<LOD	-	<LOD	-	1400	492
KS-17(2)	744	259	759	213	147	31	2	5	1	4	1184	262
KS-17(3)	152	79	151	81	110	36	<LOD	-	<LOD	-	1138	482
KS-17(4)	339	103	362	117	132	21	<LOD	-	<LOD	-	1041	192
KS-17(7)	180	76	177	66	109	21	<LOD	-	<LOD	-	1071	243
KS-17(8)	133	63	131	88	98	24	<LOD	-	<LOD	-	1159	414
KS-17(9)	725	271	731	266	121	25	4	5	4	7	1417	479
KS-17(11)	544	100	551	130	152	25	<LOD	-	<LOD	-	2855	543
KS-17(12)	461	164	456	180	125	18	1	4	<LOD	-	1488	399
KS-17(13)	493	213	504	165	138	27	29	27	29	29	940	260
KS-18(1)	49	31	46	28	177	37	8	7	8	10	627	163
KS-18(2)	75	58	75	48	203	41	55	29	55	34	647	233
KS-18(5)	97	107	102	127	230	81	93	33	88	30	737	270

Sample	⁵⁹ Co (ppm)	2SD	⁶⁰ Ni (ppm)	2SD	⁶³ Cu (ppm)	2SD	⁶⁶ Zn (ppm)	2SD	⁷¹ Ga (ppm)	2SD	¹¹⁸ Sn (ppm)	2SD
KS-08(2)	79	21	11	8	<LOD	-	420	332	7	3	<LOD	-
KS-08(3)	73	16	15	8	6	25	317	157	10	4	7	4
KS-08(4)	74	27	15	7	<LOD	-	340	84	10	4	<LOD	-
KS-08(5)	67	16	20	9	<LOD	-	159	42	11	4	<LOD	-
KS-08(6)	68	12	23	10	1	3	149	62	10	4	2	4
KS-08(10)	73	23	23	13	296	577	446	151	9	5	<LOD	-
KS-08(11)	74	18	19	7	8	40	213	67	10	4	5	4
KS-08(12)	74	13	19	9	2	9	388	133	9	3	7	3
KS-15(2)	63	22	28	12	2073	2975	467	477	5	5	37	37
KS-15(3)	58	23	21	10	568	309	239	119	2	2	4	4
KS-15(4)	66	37	25	13	796	931	293	227	6	6	28	28
KS-15(5)	56	26	20	9	450	662	224	126	2	2	1	1
KS-15(6)	53	14	14	6	105	137	128	39	2	2	0	0
KS-15(8)	54	25	22	9	27	35	111	44	3	3	0	0
KS-15(9)	51	8	19	6	48	131	130	27	3	3	0	0
KS-15(11)	55	14	21	10	323	741	213	226	9	9	0	0
KS-17(1)	119	38	7	7	0	1	420	134	10	5	0	1
KS-17(2)	107	24	7	4	<LOD	-	304	93	14	5	0	1
KS-17(3)	117	43	5	5	336	387	347	134	9	5	3	16
KS-17(4)	108	17	6	5	17	19	269	53	9	4	0	1
KS-17(7)	101	26	4	4	<LOD	-	118	46	12	5	1	1
KS-17(8)	106	36	4	4	<LOD	-	212	85	9	4	0	1
KS-17(9)	110	37	6	6	<LOD	-	487	154	10	4	<LOD	-
KS-17(11)	124	26	4	4	<LOD	-	436	98	8	3	1	1
KS-17(12)	106	20	5	5	226	443	489	343	9	4	1	1
KS-17(13)	95	32	6	4	25	40	193	130	10	4	0	1
KS-18(1)	240	74	20	8	481	499	175	60	2	2	<LOD	-
KS-18(2)	239	107	22	11	311	239	69	35	2	2	<LOD	-
KS-18(5)	230	76	24	11	1139	1362	112	63	2	2	<LOD	-

Sample	²³ Na (ppm)	2SD	²⁴ Mg (ppm)	2SD	²⁵ Mg (ppm)	2SD	²⁷ Al (ppm)	2SD	²⁹ Si (ppm)	2SD	⁴³ Ca (ppm)	2SD	⁴⁴ Ca (ppm)	2SD
KS-18(6)	282	148	427	169	420	202	919	326	7964	4740	1160	1545	1336	610
KS-18(7)	439	606	323	219	323	264	1050	561	4469	3295	1311	1390	1195	696
KS-18(8)	178	62	239	134	234	168	802	339	5123	2313	654	1123	728	453
KS-18(9)	75	72	893	3525	900	3612	1061	2777	4783	6423	389	1107	354	371
KS-18(10)	176	74	241	166	235	172	623	248	4245	1787	955	1398	817	377
KS-18(11)	262	105	417	148	404	159	693	215	7221	3735	1796	1813	1726	468
KS-19(1)	131	28	138	41	144	67	2681	503	2189	819	485	381	475	194
KS-19(2)	98	32	202	36	203	52	2626	287	1760	542	314	423	349	155
KS-19(3)	120	226	947	323	967	476	2151	1564	2557	1978	575	1093	519	828
KS-19(5)	99	34	858	248	875	369	2655	455	2465	924	482	401	477	176
KS-19(6)	102	33	722	212	746	320	2908	559	1819	872	337	462	400	211
KS-19(8)	56	28	1212	324	1227	470	1991	396	2410	750	421	504	487	236
KS-19(9)	155	47	313	76	321	106	3133	498	2329	731	461	557	533	180
KS-19(10)	151	45	469	102	468	139	3357	382	2147	677	544	545	460	184
KS-25(1)	1378	382	3169	906	3182	1232	9004	1576	11630	3715	3851	2283	3705	1008
KS-25(3)	1384	307	2456	766	2468	980	9368	1874	11778	2746	3691	2278	3630	800
KS-25(4)	1568	428	2656	547	2644	679	10845	2240	15215	4014	5086	2881	5110	1082
KS-25(5)	1671	527	3111	645	3109	770	9678	2154	13064	3063	3808	2132	3756	936
KS-25(6)	1540	294	5887	1243	5884	1083	11035	1735	13264	2808	4175	2553	4208	921
KS-25(7)	812	168	3138	641	3119	657	8813	1639	8578	2532	2519	1631	2523	751
KS-25(8)	733	179	2528	498	2511	722	8151	1304	8037	1989	2475	1658	2434	494
KS-25(10)	1029	277	1488	340	1492	343	5984	1271	11967	2658	4167	2122	4012	1129
KS-25(11)	1280	361	3215	861	3215	840	8877	2080	11844	3182	4091	2310	4144	909
KS-25(14)	671	245	1632	355	1664	345	6783	1368	5499	1961	1593	2294	1655	681
KS-26(1)	150	76	329	114	328	151	2132	750	2493	1108	852	802	839	477
KS-26(2)	37	82	177	65	173	90	2310	900	1128	933	122	303	170	370
KS-26(4)	95	51	162	123	170	134	2275	585	1741	1007	361	546	276	241
KS-26(5)	44	26	177	53	182	65	2007	375	971	489	185	411	184	140
KS-26(6)	65	39	102	48	100	61	1856	452	1209	653	257	353	228	139

Sample	⁴⁷ Ti (ppm)	2SD	⁴⁹ Ti (ppm)	2SD	⁵¹ V (ppm)	2SD	⁵² Cr (ppm)	2SD	⁵³ Cr (ppm)	2SD	⁵⁵ Mn (ppm)	2SD
KS-18(6)	56	37	60	39	232	68	91	39	85	34	808	332
KS-18(7)	101	47	106	64	214	60	295	199	284	221	824	299
KS-18(8)	82	40	74	43	260	73	861	255	845	239	751	219
KS-18(9)	62	57	65	51	225	65	38	16	36	16	687	295
KS-18(10)	78	43	80	50	255	60	21	10	20	15	762	222
KS-18(11)	55	42	60	52	287	74	7	7	6	9	960	319
KS-19(1)	1309	475	1336	541	214	23	429	191	418	104	958	356
KS-19(2)	1392	287	1419	249	205	21	132	64	136	70	874	142
KS-19(3)	768	288	776	335	211	27	2	2	2	3	2060	696
KS-19(5)	1393	555	1422	600	216	23	297	129	288	92	1136	434
KS-19(6)	1651	489	1692	528	216	33	341	184	335	148	1148	358
KS-19(8)	929	286	952	335	189	20	1	3	1	3	1632	499
KS-19(9)	1444	420	1448	439	190	23	2	3	1	3	935	292
KS-19(10)	1720	379	1710	365	224	22	2158	556	2123	352	978	209
KS-25(1)	310	115	289	91	102	26	2	5	2	6	1560	415
KS-25(3)	532	156	558	189	131	36	37	11	35	19	1517	301
KS-25(4)	1755	481	1784	488	197	59	196	119	198	123	1780	343
KS-25(5)	626	169	670	200	144	34	3	6	4	7	1582	379
KS-25(6)	951	234	988	216	136	25	126	22	123	47	2634	414
KS-25(7)	986	283	996	274	113	21	1	4	<LOD	-	3696	671
KS-25(8)	977	244	993	283	110	23	<LOD	-	1	5	1874	385
KS-25(10)	33	25	34	29	134	29	<LOD	-	<LOD	-	1661	375
KS-25(11)	148	60	149	66	79	19	<LOD	-	<LOD	-	2337	408
KS-25(14)	999	304	1015	241	158	30	287	54	287	80	2052	336
KS-26(1)	528	158	532	193	79	15	2	3	2	3	943	268
KS-26(2)	1220	378	1212	444	196	24	41	93	40	91	852	327
KS-26(4)	969	444	979	495	168	33	14	37	14	38	1200	465
KS-26(5)	968	340	970	354	171	25	18	14	18	14	796	265
KS-26(6)	862	461	875	469	176	21	2	4	2	4	812	382

Sample	⁵⁹ Co (ppm)	2SD	⁶⁰ Ni (ppm)	2SD	⁶³ Cu (ppm)	2SD	⁶⁶ Zn (ppm)	2SD	⁷¹ Ga (ppm)	2SD	¹¹⁸ Sn (ppm)	2SD
KS-18(6)	251	90	25	16	2299	1218	121	51	3	3	<LOD	-
KS-18(7)	250	93	23	10	461	810	172	109	3	2	<LOD	-
KS-18(8)	254	80	24	10	1341	620	130	62	3	2	<LOD	-
KS-18(9)	252	85	21	10	676	665	101	109	3	3	<LOD	-
KS-18(10)	269	93	23	10	890	464	104	55	3	2	<LOD	-
KS-18(11)	270	81	28	11	2539	1844	119	63	3	2	1	5
KS-19(1)	66	26	12	5	<LOD	-	202	52	3	3	0	0
KS-19(2)	64	13	11	4	<LOD	-	161	43	2	2	0	0
KS-19(3)	91	34	16	6	<LOD	-	419	128	3	3	0	0
KS-19(5)	70	25	13	6	<LOD	-	255	69	3	3	1	1
KS-19(6)	69	20	12	5	<LOD	-	229	76	3	3	1	1
KS-19(8)	81	23	15	5	<LOD	-	279	58	2	2	0	0
KS-19(9)	65	20	12	5	<LOD	-	298	64	3	3	1	1
KS-19(10)	65	15	13	7	<LOD	-	257	63	3	3	0	0
KS-25(1)	83	19	8	7	<LOD	-	220	64	15	5	0	1
KS-25(3)	85	17	7	7	28	50	177	69	13	5	0	2
KS-25(4)	84	15	7	7	<LOD	-	190	80	18	7	<LOD	-
KS-25(5)	110	55	9	6	30	43	200	74	11	4	<LOD	-
KS-25(6)	100	17	7	7	0	2	458	120	10	5	0	2
KS-25(7)	126	23	10	7	<LOD	-	577	145	9	4	<LOD	-
KS-25(8)	88	22	9	5	<LOD	-	504	133	10	4	<LOD	-
KS-25(10)	87	17	6	5	3	3	133	48	15	4	<LOD	-
KS-25(11)	106	19	26	12	<LOD	-	225	76	15	6	<LOD	-
KS-25(14)	92	15	8	7	<LOD	-	454	163	12	5	<LOD	-
KS-26(1)	51	16	8	4	<LOD	-	107	39	3	3	0	0
KS-26(2)	54	18	10	4	58	119	111	41	3	3	0	0
KS-26(4)	53	18	10	5	324	188	206	79	3	3	0	0
KS-26(5)	51	16	10	5	5	8	146	44	2	2	0	0
KS-26(6)	51	27	10	6	5	11	128	58	3	3	0	0

Sample	²³ Na (ppm)	2SD	²⁴ Mg (ppm)	2SD	²⁵ Mg (ppm)	2SD	²⁷ Al (ppm)	2SD	²⁹ Si (ppm)	2SD	⁴³ Ca (ppm)	2SD	⁴⁴ Ca (ppm)	2SD
KS-26(7)	27	17	286	58	287	84	1866	282	1273	492	127	357	115	147
KS-26(8)	45	25	191	165	200	194	2022	497	1215	716	164	370	145	144
KS-26(9)	73	27	248	63	251	91	2270	425	1309	485	295	419	332	153
KS-26(10)	404	140	374	140	374	207	4789	1365	4176	1645	1460	1005	1530	494
KS-26(11)	212	98	432	150	436	213	2057	483	3686	1934	1127	988	1085	555
KS-38(2)	359	194	280	134	282	203	2803	1399	7222	9315	1192	1158	1186	710
KS-38(3)	412	179	287	128	296	173	2342	749	5373	2556	1475	1174	1570	693
KS-38(4)	427	175	1660	3482	1520	3107	4360	5174	11317	15957	1723	1196	1625	647
KS-38(6)	406	194	439	208	454	334	2686	1052	7754	5198	1831	1341	1734	522
KS-38(8)	493	184	317	152	328	239	2645	975	5971	3338	1807	1612	1796	499
KS-38(11)	273	293	153	142	152	149	1972	1572	3890	3229	903	1316	940	978
KS-38(13)	595	217	397	233	414	328	2503	919	7191	4368	1989	1747	1914	670

Sample	⁴⁷ Ti (ppm)	2SD	⁴⁹ Ti (ppm)	2SD	⁵¹ V (ppm)	2SD	⁵² Cr (ppm)	2SD	⁵³ Cr (ppm)	2SD	⁵⁵ Mn (ppm)	2SD	-	-
KS-26(7)	831	207	837	224	126	14	<LOD	-	<LOD	-	846	182	-	-
KS-26(8)	916	456	918	460	143	31	1	2	<LOD	-	872	427	-	-
KS-26(9)	1104	302	1107	370	203	27	17	6	18	8	930	260	-	-
KS-26(10)	1013	383	1025	458	124	18	6	3	6	4	996	380	-	-
KS-26(11)	327	143	333	169	53	20	<LOD	-	<LOD	-	1018	400	-	-
KS-38(2)	262	152	271	158	323	55	114	97	110	81	1037	521	-	-
KS-38(3)	296	169	295	182	265	45	18	9	18	8	776	425	-	-
KS-38(4)	195	88	199	87	284	40	21	11	20	10	799	376	-	-
KS-38(6)	184	120	186	124	278	44	13	11	13	10	944	504	-	-
KS-38(8)	390	266	400	296	251	40	10	8	10	6	763	502	-	-
KS-38(11)	399	284	408	322	270	55	30	20	29	21	828	251	-	-
KS-38(13)	307	224	304	238	260	45	5	7	5	7	829	521	-	-

Sample	⁵⁹ Co (ppm)	2SD	⁶⁰ Ni (ppm)	2SD	⁶³ Cu (ppm)	2SD	⁶⁶ Zn (ppm)	2SD	⁷¹ Ga (ppm)	2SD	¹¹⁸ Sn (ppm)	2SD
KS-26(7)	52	13	8	4	<LOD	-	128	38	2	2	0	0
KS-26(8)	53	26	10	5	<LOD	-	120	64	3	3	0	0
KS-26(9)	54	16	10	4	0	1	142	48	2	2	2	2
KS-26(10)	54	23	12	6	<LOD	-	129	53	4	4	0	0
KS-26(11)	56	23	11	6	279	323	159	75	4	4	7	7
KS-38(2)	72	40	44	17	53	41	111	67	2	2	31	31
KS-38(3)	70	35	45	20	34	38	97	40	1	1	1	1
KS-38(4)	77	26	43	14	65	73	149	150	2	2	3	3
KS-38(6)	70	38	42	16	90	53	118	58	2	2	25	25
KS-38(8)	69	46	39	14	34	30	127	59	2	2	2	2
KS-38(11)	69	22	35	11	33	35	86	39	1	1	2	2
KS-38(13)	74	48	45	22	155	95	153	68	2	2	1	1

Table C5. Trace element concentrations (ppm) in Keystone Fe ore collected in 2020 measured by LA-ICP-MS. The numbers in parentheses represent the spot analysis number. All data were processed using Fe as the internal standard based on average preliminary EMPA data of 67wt%, except for 20KS-08b, which used 70wt%.

Sample	²³ Na (ppm)	2SD	²⁴ Mg (ppm)	2SD	²⁵ Mg (ppm)	2SD	²⁷ Al (ppm)	2SD	²⁹ Si (ppm)	2SD	⁴³ Ca (ppm)	2SD	⁴⁴ Ca (ppm)	2SD
20KS-02(1)	978	7038	272	1815	278	1867	498	928	5473	25961	801	4644	703	4122
20KS-02(3)	31	39	23	10	25	24	2044	585	1301	965	55	631	103	272
20KS-02(4)	305	2768	115	807	123	870	467	479	3803	15044	389	2358	284	2546
20KS-02(6)	401	4071	101	1197	116	1406	643	2299	4112	19832	397	3554	327	2974
20KS-02(8)	815	7555	213	1893	224	1981	563	1603	5459	26858	517	4203	581	4755
20KS-03(1)	31	49	41	39	39	39	1147	762	3140	4382	118	765	84	203
20KS-03(2)	266	511	69	142	81	158	389	185	5716	8181	186	738	243	452
20KS-03(4)	166	377	31	76	34	95	232	259	2426	2735	49	801	151	384
20KS-05(2)	331	219	782	1729	785	1757	1350	1309	6377	6161	1073	1372	1012	544
20KS-05(4)	601	521	540	521	535	508	3140	1879	7512	5141	2173	2253	2070	1656
20KS-05(8)	767	3015	4371	6844	4401	7172	1826	1728	16439	22789	1728	6371	1041	2172
20KS-05(9)	433	146	644	664	623	705	1656	679	5363	2078	1397	1366	1708	785
20KS-05(11)	234	77	235	139	237	172	1111	467	3691	2014	806	1034	646	440
20KS-08a(2)	164	173	93	28	91	45	2245	571	1883	4029	258	941	280	306
20KS-08a(4)	690	365	492	210	499	241	5011	1820	6663	3845	2198	1615	2322	923
20KS-08a(5)	77	64	119	46	124	70	1908	413	1775	1573	238	853	250	280
20KS-08a(6)	71	48	76	16	77	36	1753	297	1231	950	199	701	223	196
20KS-08a(7)	39	44	90	41	96	65	1059	191	1328	1523	105	578	170	187
20KS-08a(8)	643	205	714	233	719	257	5152	1206	6321	2234	2307	1665	2368	686
20KS-08b(1)	-	-	214	105	218	105	1251	379	3573	2380	437	928	421	692
20KS-08b(2)	-	-	906	220	927	249	4930	749	7566	1802	2615	1331	2701	1080
20KS-08b(3)	-	-	448	151	450	135	2554	467	3510	1598	1256	1025	1141	582
20KS-08b(4)	-	-	371	184	382	194	3016	1507	4209	1689	1241	1239	1298	830
20KS-08b(5)	-	-	240	56	248	60	2178	447	3048	1238	803	870	811	575
20KS-08b(7)	-	-	359	316	357	309	4232	3202	4189	3213	1367	1722	1354	1416
20KS-08b(8)	-	-	427	455	427	450	3387	1260	4815	2470	1447	1566	1419	973

Sample	⁴⁷ Ti (ppm)	2SD	⁴⁹ Ti (ppm)	2SD	⁵¹ V (ppm)	2SD	⁵² Cr (ppm)	2SD	⁵³ Cr (ppm)	2SD	⁵⁵ Mn (ppm)	2SD
20KS-02(1)	6	14	6	9	32	11	1	6	0	4	545	84
20KS-02(3)	0	3	0	6	7	6	1	4	<LOD	-	639	119
20KS-02(4)	26	26	24	28	41	15	2	8	1	6	555	93
20KS-02(6)	2	8	3	10	11	5	2	8	1	6	506	125
20KS-02(8)	20	15	19	21	48	17	2	8	<LOD	-	443	88
20KS-03(1)	1	5	2	9	19	8	3	11	1	5	531	123
20KS-03(2)	0	3	0	5	11	6	1	3	0	3	487	223
20KS-03(4)	0	4	1	7	17	6	1	6	0	4	535	175
20KS-05(2)	299	128	272	117	248	35	28	13	28	18	731	131
20KS-05(4)	696	319	675	288	174	51	72	70	76	68	693	163
20KS-05(8)	284	170	277	227	250	36	73	85	75	94	619	153
20KS-05(9)	330	114	305	125	248	37	102	87	105	88	641	103
20KS-05(11)	255	101	242	93	210	18	9	5	10	8	528	89
20KS-08a(2)	868	236	872	234	138	22	6	12	5	8	801	110
20KS-08a(4)	1197	283	1189	316	98	11	80	22	78	27	1008	214
20KS-08a(5)	555	186	561	219	130	47	2	4	1	5	923	329
20KS-08a(6)	627	216	632	226	138	16	1	4	1	5	856	228
20KS-08a(7)	396	123	382	148	83	13	2	4	1	4	831	261
20KS-08a(8)	1861	552	1914	652	103	15	37	15	36	20	1135	255
20KS-08b(1)	470	170	468	175	83	14	16	7	17	10	1065	223
20KS-08b(2)	1250	270	1311	245	57	13	4	4	4	5	1085	140
20KS-08b(3)	1332	243	1310	246	76	11	10	4	10	6	1072	122
20KS-08b(4)	1652	587	1631	461	98	15	10	5	11	6	1158	255
20KS-08b(5)	1530	287	1572	310	95	12	19	6	19	7	1005	100
20KS-08b(7)	1158	549	1153	464	131	26	3	6	3	6	1028	310
20KS-08b(8)	906	254	945	292	82	27	21	17	21	18	938	157

Sample	⁵⁹ Co (ppm)	2SD	⁶⁰ Ni (ppm)	2SD	⁶³ Cu (ppm)	2SD	⁶⁶ Zn (ppm)	2SD	⁷¹ Ga (ppm)	2SD	¹¹⁸ Sn (ppm)	2SD
20KS-02(1)	233	351	413	67	1114	1901	1164	824	3	2	17	62
20KS-02(3)	217	35	111	87	76	83	1619	503	3	2	1	6
20KS-02(4)	189	39	453	120	592	267	1632	507	3	3	20	90
20KS-02(6)	170	38	452	108	298	318	826	1274	3	2	21	88
20KS-02(8)	257	109	380	126	1453	920	2303	1397	3	2	19	90
20KS-03(1)	288	84	271	201	442	491	803	374	3	2	33	131
20KS-03(2)	365	129	229	95	81	73	290	119	2	2	7	35
20KS-03(4)	373	122	349	93	40	15	102	48	2	2	27	111
20KS-05(2)	94	19	22	15	4190	2654	790	542	9	5	13	61
20KS-05(4)	104	17	13	6	2883	2165	634	361	13	8	<LOD	-
20KS-05(8)	100	27	20	15	3449	2109	758	485	9	5	25	102
20KS-05(9)	93	20	16	11	1824	884	524	196	10	4	3	17
20KS-05(11)	69	14	11	6	521	504	207	115	8	3	1	9
20KS-08a(2)	52	8	11	6	4	13	315	311	6	3	27	134
20KS-08a(4)	52	12	15	6	3	13	218	76	8	4	9	43
20KS-08a(5)	52	19	11	7	286	421	173	96	7	3	5	30
20KS-08a(6)	49	16	11	5	1	5	160	64	5	2	3	19
20KS-08a(7)	50	17	14	7	7	32	450	140	4	2	5	26
20KS-08a(8)	51	11	17	8	13	34	239	65	9	4	6	30
20KS-08b(1)	50	8	20	8	-	-	-	-	5	2	-	-
20KS-08b(2)	48	8	21	5	-	-	-	-	9	3	-	-
20KS-08b(3)	50	8	25	7	-	-	-	-	8	3	-	-
20KS-08b(4)	50	6	16	5	-	-	-	-	7	3	-	-
20KS-08b(5)	48	6	14	5	-	-	-	-	6	2	-	-
20KS-08b(7)	50	8	11	4	-	-	-	-	8	5	-	-
20KS-08b(8)	50	8	18	6	-	-	-	-	7	2	-	-